Physics-based Reduced-order Modeling of Flash-boiling Injection Processes in Internal Combustion Engines

Simulation von Einspritzvorgängen mit Flash-Sieden in Verbrennungsmotoren mittels physik-basierter Modelle niedriger Ordnung

Von der Fakultät für Maschinenwesen der Rheinisch-Westfälischen Technischen Hochschule Aachen zur Erlangung des akademischen Grades eines Doktors der Ingenieurwissenschaften genehmigte Dissertation

vorgelegt von

Avijit Saha

Berichter: Univ.-Prof. Dr.-Ing. Heinz Günter Pitsch
Univ.-Prof. Dr.-Ing. Andreas Kronenburg

Tag der mündlichen Prüfung: 29. September 2023

"*Dream is not that which you see while sleeping, it is something that does not let you sleep.*"

– Dr. A. P. J. Abdul Kalam

Preface

The research work reported in the present dissertation has been carried out within the framework of the Cluster of Excellence - "The Fuel Science Center" at Institute of Combustion Technology, RWTH Aachen University. I wish to express my sincere gratitude to the Deutsche Forschungsgemeinschaft (DFG, German Research Foundation) for providing the necessary funding during the course of this research under Germany's Excellence Strategy – Exzellenzcluster 2186 "The Fuel Science Center" ID: 390919832.

First and foremost, I am deeply grateful to my supervisor, Prof. Dr.-Ing. Heinz Pitsch, for granting me the chance to work on this interesting topic. I owe a great debt of gratitude to him for his unwavering support, guidance, and encouragement throughout my doctoral journey. Prof. Pitsch's immense patience, experience, insightful feedback, and valuable advice have been instrumental in shaping my research skills and the successful completion of this research work. I would like to express my profound gratitude to Prof. Dr.-Ing. Andreas Kronenburg for his essential role as the second referee on the committee and for his invaluable guidance and support throughout the progress of my thesis. Additionally, I extend my thanks to Prof. Dr.-Ing. Karl Alexander Heufer for serving as the committee chair.

Further, I would like to thank all my colleagues at ITV for their kind support and help. In particular, I am ever grateful to Dr.-Ing Abhishek Y. Deshmukh and Dr. Temistocle Grenga for their generosity in sharing knowledge and eagerness to engage in discussions on any specific topic. I am also very thankful to Dr.-Ing Jörn Hinrichs, Dr.-Ing Tobias Falkenstein, Dr.-Ing Rupali Tripathi, Dr.-Ing Florian vom Lehn, Mathis Bode, Fabian Fröde, Dominik Goeb, Marco Davidovic, Hongchao Chu, and Raghavan Lakshmanan for their generous help. I would like to appreciate the support of Leif Schumacher, Peter Augustin, and Dr.-Ing Manuel Reddemann from the Institute of Heat and Mass Transfer (WSA) for the useful discussion regarding the experimental work on flash-boiling. Additonally, I would like to thank Peter Krasnov for his kind support regarding IT issues. I am also grateful to Sonja Huppertz and Eva Schieren for their support in all administrative issues.

Last but not least, I would like to express my deepest gratitude to my mom Khana Saha and my uncle Shyamal Chatterjee for their love, motivation, and assistance in all my endeavors. I am also immensely grateful to my loving

wife Ritupriya for her unwavering support during the concluding phases of my PhD.

Aachen, September 29, 2023 Avijit Saha

Abstract

In order to accurately quantify flash-boiling injection processes in direct-injection spark-ignition (DISI) engines, it is imperative to develop a fundamental understanding of the underlying physics associated with this complex injection phenomenon at a microscopic level. In this dissertation, first, single-droplet flash-boiling is investigated by employing a Lagrangian particle tracking (LPT) approach considering both internal and external vaporization processes. Next, a novel reduced-order Lagrangian model is proposed for accurately capturing the vapor bubble growth in superheated microdroplets considering bubble-bubble interactions along with the finite droplet-size effects. It is observed that bubble-bubble interactions have a notable impact on the bubble growth dynamics and lead to a slower expansion of the vapor bubble in the later stage of growth. After that, a simplified nondimensional semi-analytical solution for bubble growth, which also includes the bubble interactions, is derived based on the dimensional analysis of the newly derived Rayleigh-Plesset equation (RPE) to estimate the bubble growth behavior with reasonable accuracy using larger time step sizes for a wide range of operating conditions, thus making it useful for simulations of superheated sprays with large numbers of droplets.

A large-eddy simulation (LES) of flash-boiling spray employing Lagrangian particle tracking is then performed with the newly derived subgrid-scale model for the bubble growth in a multibubble environment. The simulation results are compared against experimental measurements in terms of liquid penetration length and steady-state Sauter-mean diameter. A one-dimensional (1D) cross-sectionally averaged spray (CAS) model is also developed in this dissertation for use in faster simulations of flash-boiling sprays. It is found that the newly developed CAS model captures the trends in global flash-boiling spray characteristics reasonably well for different operating conditions and fuels.

Zusammenfassung

Zur genauen Quantifizierung von Flashboiling-Einspritzvorgängen in Motoren mit Direkteinspritzung und Fremdzündung (DISI) ist es unerlässlich, ein grundlegendes Verständnis der diesem komplexen Einspritzphänomen zugrunde liegenden physikalischen Zusammenhänge auf mikroskopischer Ebene zu entwickeln. In dieser Dissertation wird zunächst das Flashboiling von Einzeltropfen mithilfe eines Lagrangeschen Partikelverfolgungsansatzes (LPT) untersucht, der sowohl interne als auch externe Verdampfungsprozesse berücksichtigt. Anschließend wird ein neuartiges Lagrangesches Modell reduzierter Ordnung vorgestellt, um das Dampfblasenwachstum in überhitzten Mikrotropfen unter Berücksichtigung von Blasen-Blasen-Wechselwirkungen und der endlichen Tropfengröße genau zu erfassen. Es wird festgestellt, dass Blasen-Blasen-Wechselwirkungen einen erheblichen Einfluss auf die Dynamik des Blasenwachstums haben und zu einer langsameren Ausdehnung der Dampfblase im späteren Stadium des Wachstums führen. Anschließend wird eine vereinfachte nichtdimensionale halbanalytische Lösung für das Blasenwachstum abgeleitet, die auch die Blasenwechselwirkungen einbezieht und auf der Dimensionsanalyse der neu abgeleiteten Rayleigh-Plesset-Gleichung (RPE) basiert. Damit kann das Blasenwachstumsverhalten mit angemessener Genauigkeit unter Verwendung größerer Zeitschrittgrößen für einen breiten Bereich von Betriebsbedingungen berechnet werden, wodurch die Verwendung des Modells für Simulationen überhitzter Sprays mit einer großen Anzahl von Tropfen ermöglicht wird.

Anschließend wird eine Large-Eddy-Simulation (LES) eines flash-boiling Sprays mit Lagrangescher Partikelverfolgung mit dem neu abgeleiteten Modell für das Blasenwachstum in einer Multiblasenumgebung durchgeführt. Die Simulationsergebnisse werden mit experimentellen Messungen in Bezug auf die flüssige Eindringtiefe und den mittleren Sauter-Durchmesser im stationären Zustand verglichen. In dieser Dissertation wird auch ein eindimensionales (1D) querschnittsgemitteltes Spraymodell (CAS) entwickelt, das für schnellere Simulationen von flash-boiling Sprays verwendet werden kann. Es zeigt sich, dass das neu entwickelte CAS-Modell die Tendenzen in den globalen Flash-Boiling-Spray-Charakteristika für verschiedene Betriebsbedingungen und Kraftstoffe hinreichend gut erfasst.

Publications

This dissertation is mainly based on the following scientific publications:

Peer-reviewed Journals

- A. Saha, T. Grenga, A.Y. Deshmukh, J. Hinrichs, M. Bode, and H. Pitsch. Numerical modeling of single droplet flash boiling behavior of e-fuels considering internal and external vaporization. *Fuel*, Vol. 308, pp: 121934, 2022. doi: 10.1016/j.fuel.2021.121934
- A. Saha, A.Y. Deshmukh, T. Grenga, and H. Pitsch. Dimensional Analysis of Vapor Bubble Growth Considering Bubble-bubble Interactions in Flash Boiling Microdroplets of Highly Volatile Liquid Electrofuels. *Int. J. Multiph. Flow*, Vol. 165, pp: 104479, 2023. doi: https://doi.org/10.1016/j.ijmultiphaseflow.2023.104479
- A. Saha, A.Y. Deshmukh, T. Grenga, and H. Pitsch. Physics-based reduced-order modeling of flash-boiling sprays in the context of internal combustion engines. (in preparation)

Conference Papers

- A. Saha, A.Y. Deshmukh, T. Grenga, M. Bode, M. Grunewald, M., Y. Kaya, V. Kirsch, M. A. Reddemann, R. Kneer, and H. Pitsch. Numerical Modeling of the Flash Boiling Characteristics of E-Fuels at Low Ambient Pressure. *15th Triennial International Conference on Liquid Atomization and Spray Systems*, Aug 30 – Sep 2, 2021, Edinburgh, Scotland, UK
- A. Saha, A.Y. Deshmukh, T. Grenga, and H. Pitsch. Lagrangian Modeling of Vapor Bubble Growth in Flash Boiling Single Droplet Considering Bubble-bubble Interactions. *11th International Conference on Multiphase Flow*, April 2 - 7, 2023, Kobe International Conference Center, Kobe, Japan

For the listed publications, the author was responsible for developing the concepts, designing the methodology, and creating the software. The author also carried out thorough investigations and performed formal analyses to validate the findings. Throughout the process, the author was responsible for writing the original draft and creating visualizations to aid understanding the results.

Contents

List of Figures

List of Tables

Abbreviations

0D	Zero-dimensional
1D	One-dimensional
3D	Three-dimensional
CAS	Cross-sectionally Averaged Spray
CFD	Computational Fluid Dynamics
CFL	Courant-Friedrichs-Lewy
CO_2	Carbon dioxide
DISI	Direct Injection Spark Ignition
DME	Dimethyl Ether
DNS	Direct Numerical Simulation
ECN	Engine Combustion Network
GDI	Gasoline Direct Injection
GHG	Greenhouse Gas
HC	Hydrocarbon
HCCI	Homogeneous Charge Compression Ignition
HRe	High Reynolds Number
HRM	Homogeneous Relaxation Model
HS-LP	High Superheat-Low Pressure
IC	Inertia-controlled
IPCC	Intergovernmental Panel on Climate Change
LES	Large-Eddy Simulation
LOx	Liquid Oxygen
LPT	Lagrangian Particle Tracking
LRe	Low Reynolds Number
LS-LP	Low Superheat-Low Pressure
MRe	Medium Reynolds Number
MS-HP	Medium Superheat-High Pressure
MS-LP	Medium Superheat-Low Pressure
MS-MP	Medium Superheat-Medium Pressure
OMEx	Oxymethylene Ethers
PFI	Port Fuel Injection
RK	Runge-Kutta
ROM	Reduced-Order Model
RPE	Rayleigh-Plesset Equation
SMD	Sauter-Mean Diameter
ST	Surface Tension-controlled
T	Transition

TD	Thermal Diffusion

Nomenclature

α	Thermal diffusivity
b	Maximum radial distance for integration
$\mathrm{B_{M,d}}$	Spalding mass transfer number
C	Specific heat capacity
C_d	Discharge coefficient of nozzle
C_p	Specific heat capacity at constant pressure
ΔP	Pressure differential
δ	Thermal boundary layer thickness
$\Delta\theta$	Superheating degree
$\mathsf{D_o}$	Initial droplet diameter
e	Internal energy
E_drup	Disruption energy
ϵ	Void fraction
f_2	Analytical heat transfer correction factor
γ	Ratio of specific heats
$\Gamma_\mathrm{v,g}$	Diffusion coefficient
h_ex	External heat transfer coefficient
h_f	Flashing heat transfer coefficient
Ja	Jakob number
k_b	Boltzmann constant
λ	Thermal conductivity
Λ	Wavelength
L	Latent heat / Nozzle length
L_k	Knudsen length
μ	Molecular viscosity
n	Bubble number density
Nu	Nusselt number
Oh	Ohnesorge number
$\dot{\omega}/\dot{S}$	Source term
Ω	Frequency
P	Pressure
$\mathcal{P}(\hat{d}')$	Droplet size distribution
P_hd	Total hydrodynamic pressure
$P_\mathrm{hd,acc}$	Hydrodynamic pressure due to interface acceleration
$P_\mathrm{hd,vel,b}$	Hydrodynamic pressure due to interface velocity
ϕ	Quantity of interest
P_μ	Pressure due to viscous force

$\mathrm{Pr_g}$	Prandtl number
P_σ	Pressure due to surface tension force
R	Radius
r	Radial coordinate
$\mathcal{R}$	Universal gas constant
Re	Reynolds number
ρ	Density
R_p	Pressure ratio
$\mathrm{Sc_g}$	Schmidt number
$\mathrm{Sh_d}$	Sherwood number
σ	Surface tension
Ta	Taylor number
τ	Characteristic time / Particle time constant
Θ	Nondimensional surface tension
t	Time coordinate
T	Temperature
u	Velocity
$\mathsf{U_o}$	Nozzle exit velocity
v_l	Liquid molecular volume
V	Volume
We	Weber number
W	Molar mass
x	Number of oxymethylene groups / Spatial coordinate / Transient position
ξ_sub	Nondimensional subcooled evaporation parameter
ξ_sup	Nondimensional superheated evaporation parameter
$\chi_\mathrm{eq,v,s}$	Equilibrium mole fraction at droplet surface
$\chi_\mathrm{neq,v,s}$	Nonequilibrium mole fraction at droplet surface
Y	Mass fraction
z	Axial coordinate

Subscripts

0	Initial values
a	Air / Droplet acceleration / Molecular surface area
d	Droplet property
g	Gaseous phase

i	Cartesian directions / Internal / No. of bubbles / No. of phase
j	Cartesian directions
k	Droplet / bubble quantities
l	Liquid phase
v	Vapor

1 Introduction

In order to minimize the impact of global warming, the Intergovernmental Panel on Climate Change (IPCC) has reported an effort to limit the global temperature increase to 1.5 °C. It has also been emphasized that net-zero global carbon dioxide (CO_2) emissions need to be reached for achieving this goal by 2050 [1]. Thus, reducing greenhouse gas (GHG) emissions, from the transportation sector, especially CO_2 is one of the main global challenges to achieve a more sustainable future. Powertrain electrification is being considered as an alternative to reduce direct GHG emissions from internal combustion engines (ICEs). Still, developing ICEs with advanced injection and combustion concepts that improve efficiency and decrease pollutant emissions are essential steps towards reducing their environmental impact.

Direct-injection spark-ignition (DISI) engines have been demonstrated to have the potential for higher thermal efficiencies than port-fuel injection (PFI) engines leading to lower fuel consumption and lower CO_2 emissions [2]. DISI technology has several other advantages such as improved charge cooling potential, faster transient response, precise fuel metering, and lower cold start emissions [3–6]. DISI engines use high-pressure injection systems for atomizing the liquid fuel into small droplets. Although an accurate control of fuel delivery, atomization, and good efficiency with reasonable emissions can be achieved via high-pressure injection systems, there are certain drawbacks associated with this injection mechanism. For example, due to high-pressure injection, the liquid fuel jet exits the injector nozzle normally with higher momentum, and thus increases the chances of spray impingement onto the cylinder liner and/or piston head [7]. The formation of a liquid film on the wall surface due to spray impingement will in turn affect the near-wall fuel-air mixing process [8], as the fuel film is hard to evaporate and could lead to irregular combustion such as pool fire with subsequent production of soot and unburned hydrocarbons (HC) [7, 9]. Due to this ever-increasing stringent emission regulations, the atomization characteristics of DISI engines need to be improved further such that the resulting fine spray droplets from enhanced atomization lead to better fuel-air mixing with desired combustion characteristics [7]. Increasing injection pressure to extremely high values for achieving superior atomization characteristics has already been shown to be insufficient [10]. However, the drawbacks mentioned above with the

high-pressure injection strategy can be overcome by using the flash-boiling injection technique [5, 11].

Flash-boiling injection in DISI engines has become a promising alternative to generate a much finer spray compared to high-pressure injection [12–15]. Injecting liquid fuel into DISI engines operating at part-load, light-load, or idle conditions with early injection strategies for homogeneous-charge engine operation causes explosive vaporization of the fuel jet via bubble nucleation and growth [16, 17]. This rapid phase-change phenomenon occurs due to the superheating of the liquid fuel upon entering the combustion chamber under the above-mentioned operating conditions. The potentially explosive nature of flash-boiling results in tiny droplets due to the abrupt disintegration of the liquid jet, which in turn enhances the mixture homogeneity between air and fuel by increasing the vaporization rate [18], widening the spray plume due to the increased radial expansion via bubble growth, and reducing the droplet velocities, thus leading to shorter penetrations [16]. The underlying mechanisms of the flash-boiling process are fairly complex. They can be broadly categorized into three stages, namely, nucleation of vapor bubbles, bubble growth, and finally jet burst [19]. These stages occur on a very fast timescale initiated by sudden depressurization or heating, and therefore, a detailed understanding of the fundamental processes involved in flash-boiling at a microscopic droplet level is necessary to accurately quantify its effect on the macroscopic spray structure.

Many researchers have studied the flash-boiling phenomena at a microscopic single droplet level to have an in-depth understanding of the above-listed subprocesses (such as [20–22], among the most recent). Brown and York [23] were the first to investigate the influence of flash-boiling at a macroscopic scale on the breakup and atomization process of superheated water and freon-11 jets. Sher and Elata [24] quantified the flash-boiling spray formed by the binary mixture of toluene and freon-22 from pressure cans in terms of droplet size distributions for different pressures and temperatures. Adachi et al. [25] reported a significant increase in fuel vapor concentration and subsequently more homogeneous fuel-air mixture formation from their experimental and theoretical investigations on the atomization process of superheated n-pentane sprays. Vanderwege and Hochgreb [26] studied the effect of fuel volatility on sprays from high-pressure swirl injectors for fuel mixtures of doped and undoped isooctane and indolene, and reported a 40% reduction in droplet diameter under flash-boiling conditions. Kale and Banerjee [27] investigated the flash-boiling behavior of alcohol fuels using a direct-injection (DI) injector under engine-like hot injector body conditions. They also reported a significant

reduction in droplet diameter (58.45% and 54.5% for butanol and iso-butanol, respectively) at elevated fuel temperatures due to the occurrence of flash-boiling. Senda et al. [28] performed experiments with fuel mixtures of tri-decane and liquefied CO_2 to investigate the flash-boiling spray combustion characteristics. They found that the flash-boiling of the fuel mixture leads to a significant reduction in soot and NO_x emissions. The brake-specific fuel consumption was also observed to decrease due to the formation of an advanced flammable mixture resulting from flash-boiling. Aleiferis et al. [29] and Serras-Pereira et al. [30] studied the combined effect of cavitation and flash-boiling on spray characteristics of different fuels using an optical DI injector nozzle. They revealed that an increase in the cavitation phenomenon inside the nozzle hole at higher fuel temperatures results in a large number of vapor bubbles, which then act as a strong source of nucleation sites and lead to an increase in the rate of superheated fuel vaporization. Several other experimental studies on flash-boiling injection are available in the literature (such as [31–36], to name a few), which confirm the potential of flash-boiling sprays in producing superior spray atomization along with improved combustion characteristics in DISI engines.

Furthermore, flash-boiling inejction of the newly developed electrofuels (also known as 'e-fuels') in DISI engines could also be a promising alternative in improving the combustion behavior and reducing pollutant emissions. These e-fuels are are produced by the combined utilization of CO_2 as carbon sources and 'green hydrogen' from water electrolysis, thus enabling highly efficient and sustainable synthetic pathway to carbon-reduced fuels. Oxymethylene ethers (OMEx) are a class of such e-fuel candidates [37], which have shown a great potential to overcome the soot-NO_x trade-off associated with the conventional diesel fuel because of their almost soot-free combustion [38–40]. Recently, OMEx fuels have been blended with gasoline [41] and also investigated as a potential fuel in homogeneous charge compression ignition (HCCI) combustion [42, 43]. However, short-chain OMEx have lower viscosity and higher vapor pressure compared to conventional fuels. This latter property is particularly relevant, because it makes them prone to flash-boiling depending on the conditions.

1.1 Flash-boiling in Infinite Superheated Liquid Medium

Superheated liquids undergo spontaneous phase transition through the generation of vapor bubble nuclei [44]. Nuclei larger than the critical size continue to grow rapidly via the following phases: (1) surface tension-controlled phase,

(2) transitional phase, (3) inertia-controlled phase, and (4) thermal diffusion-controlled growth phase [45]. Several attempts with varying degrees of simplifying assumptions have been made to study the physics of vapor bubble growth in the infinitely large superheated liquid medium. Early theoretical work by Rayleigh [46] provided an approximate solution of spherical vapor bubble growth by considering only the inertial effect. Since the cooling effect of vaporization is not considered in the Rayleigh solution, a reliable prediction of bubble growth can be obtained only when the system pressure is sufficiently low or the initial superheating degree is sufficiently high [47]. Assuming a thin thermal boundary layer, [48] later formulated an asymptotic solution for thermal diffusion-controlled bubble growth based on their zero-order solution for the bubble wall temperature [49]. This solution is valid for the later stages of bubble growth when the bubble radius is large enough so that the heat flux becomes the important factor controlling the growth rate. Scriven [50] also investigated the thermal diffusion-controlled growth by relaxing the thin thermal boundary layer assumption and concluded that the asymptotic growth rate is identical to the Plesset and Zwick [48] solution for moderate to large Jakob numbers (Ja), which is a non-dimensional parameter defined as, $\mathrm{Ja} = \rho_\mathrm{l} c_\mathrm{l} \left(T_\infty - T_b(P_\infty)\right) / \left(\rho_\mathrm{v} L_\mathrm{v}\right)$, where T_∞ represents the liquid temperature, T_b the liquid boiling temperature, P_∞ the liquid pressure, c_l the specific heat capacity of liquid, L_v the latent heat of vaporization, ρ_l the liquid density, and ρ_v the vapor density. For low superheating degrees or small Jakob number, Scriven [50] found a different asymptotic dependency of bubble growth rate on the Jakob number. Riznic et al. [51] later confirmed the dependency on Jakob number and reported that for $\mathrm{Ja} > 2$, the thin thermal boundary layer assumption is valid, whereas for $\mathrm{Ja} < 2$, the assumption is no longer valid because of the effect of interface curvature on the temperature gradient at the interface. Mikic et al. [52] provided a first general expression for the bubble growth by combining the solution of inertia- and thermal diffusion-controlled stages. Good agreement was obtained in the comparison with the experimental data of Lien [53] for superheated water over a wide range of system pressures. However, the surface tension force, which dominates during the initial stages of the bubble growth, is not considered in the analytical works described above. Donne and Ferranti [54], Lee and Merte [47], and Robinson [45] addressed this issue by numerically solving the complete one-dimensional energy and momentum equations without making any assumption regarding the thermal boundary layer at the liquid-vapor interface, thus providing a more accurate description of bubble growth. Robinson [45] was the first to explore the detailed physics of spherical bubble growth with a primary focus

on the interaction between hydrodynamics and thermal diffusion near the liquid-vapor interface and its effect on the different stages of bubble growth.

1.2 Single Droplet Flash-boiling

The studies mentioned in Section 1.1 investigated only the growth of an isolated single bubble for a long period of time in an infinite liquid pool without considering finite drop-size effects and the droplet-disruption phenomenon. However, for flash-boiling spray in realistic engines, multiple bubbles can be present inside superheated liquid droplets. As the vapor bubbles grow, the droplets continue to expand and can eventually rupture into smaller child droplets once a critical void fraction is reached. To explore the effect of the presence of multiple bubbles and the droplet disruption phenomena, Xi et al. [21] simulated the flash-boiling in a superheated single droplet of dimethyl ether (DME) using the boiling explosion model derived by Zhang and Zhang [55]. They reported that the boiling explosion time becomes shorter for higher fuel temperatures and lower ambient pressures. Recently, Xi et al. [56] investigated the multi-mode breakup and boiling vaporization of binary fuel droplets of n-butanol and n-hexadecane in an elevated ambient temperature regime of 537 – 609 K via the pendant drop method. They also proposed an analytical model of heterogeneous nucleation for predicting the temperature at the onset of bubble nucleation. Fostiropoulos et al. [57] studied the breakup time initiation of water/heavy fuel oil emulsion droplets using a simple fitting model for the operating conditions related to marine diesel engines. Senda et al. [19] developed a model that calculates the critical void fraction to limit the growth process of vapor bubbles inside the superheated liquid. Once the critical value is reached, the droplet is assumed to break up into smaller child droplets with a number density equal to twice the bubble number density. Kawano et al. [58] utilized this approach to initiate the breakup process in their multicomponent flash-boiling spray simulation and observed a good qualitative agreement with the experimental measurements.

The superheated liquid may also undergo a phase transition from its external surface due to internal as well as external heat transfer. Vaporization from the superheated droplet external surface was highlighted by Adachi et al. [25], who presented simulation results in good agreement with their experimental measurements of fuel vapor concentration inside a flash-boiling spray. Recently, Yang [59] developed a flash-boiling model coupling the internal vaporization with the external one and studied the flash-boiling of iso-octane single droplet in real gasoline engine conditions. Although the important flash-boiling

phenomena were well-captured by their model, the detailed physics associated with the internal vaporization of a single droplet was not explored.

1.2.1 Influence of Bubble-bubble Interactions

The single droplet flash-boiling studies described above mainly focused on bubble growth without considering the bubble-bubble interactions. However, in reality, multi-bubble interactions in a superheated droplet play a crucial role in determining the volume expansion of the droplet. The vapor bubbles located closer to the droplet external surface grow faster compared to those near the center due to lower pressure faced by the droplet external surface [60]. This qualitatively affects the dynamics presented here in two ways. First, the faster-growing vapor bubbles may not undergo all growth stages as they may burst extremely fast and cause partial rupture of the parent droplet. The whole parent droplet may even burst due to the occurrence of successive partial ruptures. Second, the slower-growing vapor bubbles close to the droplet interior may not undergo all the growth stages as well depending on the dynamics of the bubbles near the surface. Dietzel et al. [60] performed a direct numerical simulation (DNS) of bubble clusters to quantify the effects of bubble-bubble interactions in comparison with the single bubble growth for liquid oxygen (LOx) in different simplified configurations. They reported a significant reduction (more than 70%) in the growth rate of the vapor bubbles located near the center of the LOx jet. These bubbles were found to have a negligible contribution to the volumetric expansion of the liquid jet. However, such fully-resolved simulations for accurate predictions of the bubble growth characteristics in multibubble environments are not feasible for large-scale spray simulations due to the high computational cost. A reduced-order model (ROM) considering the bubble-bubble interactions is thus necessary in this regard. The studies available in the literature mainly focus on the reduced-order modeling of the bubble-bubble interactions in the context of cavitation phenomena (such as [61–67], to name a few). Although there are plenty of studies on flash-boiling ROMs of single droplets and spray available in the literature (such as [18, 19, 25, 45, 59, 68–71], to name a few), none of them considered the effect of bubble-bubble interactions in their study.

1.3 Flash-boiling Spray

1.3.1 Three-dimensional (3D) Simulation

Significant efforts were made in developing numerical methods for modeling flash-boiling spray characteristics. Zuo et al. [68] presented a superheated spray and vaporization model for studying the evolution and vaporization behavior of flashing sprays in GDI engines. Zeng and Lee [72] developed an atomization model for flash-boiling sprays and concluded that the combined effect of aerodynamic forces and bubble expansion is responsible for breakup under flash-boiling conditions. Kawano et al. [58] integrated the bubble nucleation, growth and disruption sub-models into the KIVA3V code, and numerically investigated the flash-boiling characteristics of multicomponent fuels. Price et al. [73] proposed a numerical framework for modeling flash-boiling sprays using a Lagrangian Particle Tracking (LPT) technique. The spray collapse and recirculations of droplets were well predicted by their model in comparison with the experimental measurements. Price et al. [18] later applied this model to investigate the flash-boiling spray characteristics of high-volatility fuels (such as n-pentane, n-hexane, iso-hexane, and ethanol) as well as low-volatility fuels (such as iso-octane and n-butanol) over a wide range of injection systems. Guo et al. [74] numerically investigated the flashing n-hexane sprays using the homogeneous relaxation model (HRM) in a diffuse Eulerian framework. They observed an under-expanded flashing jet due to the explosive evaporation within the intact liquid core, which was found to exist in the near nozzle regime. With increasing superheating degrees, the shock-wave structure, known as 'Mach-disk', was also identified at some distance from the nozzle exit. Duronio et al. [75] developed a Lagrangian flash-boiling breakup model in OpenFOAM and studied the spray characteristics of the Engine Combustion Network (ECN) Spray G injector under flash boiling conditions for different injection pressures. Duronio et al. [76] later simulated the internal nozzle flow in an Eulerian framework using the HRM model and coupled it with their previously developed Lagrangian external spray simulations to investigate the effect of in-nozzle phase change on global spray characteristics. However, most of these numerical studies simulated the flash-boiling sprays considering the subgrid-scale model which does not incorporate the bubble-bubble interactions phenomenon.

1.3.2 One-dimensional (1D) Simulation

Although the 3D computational fluid dynamics (CFD) simulations are necessary to get a detailed fundamental understanding of the underlying physics of the flash-boiling phenomena, the high computational cost associated with these simulations makes their application in design of experiments, system simulations, creating digital twins, and screening of novel fuel candidates difficult. Model order reduction from 3D to 1D or 0D while preserving the essential multiphysics information is therefore useful as long as sufficient accuracy can be achieved. For example, in the fuel design process, each and every fuel candidate needs to undergo an extensive testing process before being used in real combustion systems. Assessing the spray characteristics and combustion performance is one of the crucial steps in this testing phase. However, conducting experiments on an engine test bench to investigate the spray and combustion characteristics for a large number of fuel candidates is extremely difficult [77]. The physics-based ROMs can also be used as a digital twin of the internal combustion engine for closed-loop feedback control of the combustion performance [77].

Sazhin et al. [78] proposed simplified analytical expressions for obtaining the spray tip penetrations during the initial stages and the later two-phase flow regimes. Desantes et al. [79] derived a theoretical model to investigate the influence of the injection parameters on the macroscopic spray characteristics based on the assumption of the conservation of the momentum flux along the spray axis. Pastor et al. [80] investigated the global spray characteristics of the transient inert diesel sprays using a 1D Eulerian spray model considering the mixing-controlled processes and locally-homogeneous flow field. Later, Desantes et al. [81] extended it to reactive diesel spray cases. Although considerable efforts have been made to the development of the ROMs for subcooled sprays, studies on the 1D physics-based ROM development for macroscopic characterization of the flash-boiling sprays are still scarce in the literature.

1.4 Objectives of the Dissertation

Flash-boiling injection can enhance fuel atomization via explosive vaporization and rapid disintegration of the liquid jet. This leads to better fuel-air mixing and ultimately improves combustion characteristics. Therefore, it is crucial to develop simplified yet physics-based models for accurately capturing the spray dynamics during flash-boiling injection. Along these lines, the objectives of this dissertation are:

1. Perform a detailed investigation of flash-boiling phenomena of highly volatile liquid fuel microdroplets under different operating conditions. A novel single-droplet flash-boiling model combining internal and external vaporization processes will be developed in a Lagrangian Particle Tracking (LPT) framework for assessing their relative importance in the overall droplet flash vaporization. The internal vaporization model will include several sub-models that compute bubble number density, bubble growth rate, and droplet bursting criteria. External vaporization will be modeled considering heat transfer from the droplet interior to the droplet surface and from the surrounding gas to the droplet surface. The model validation will be performed with experimental measurements of single isolated vapor bubble growth in an infinite superheated liquid water medium. The bubble growth characteristics will be analyzed in detail for highly volatile microdroplets under various superheating degrees. The influence of fuel molecular structure on the bubble dynamics will be highlighted. The role of bubble dynamics on the overall droplet vaporization process will also be quantified.

2. Develop a novel Lagrangian bubble growth model considering the effects of finite droplet-size and bubble-bubble interactions in flash-boiling microdroplets. A modified Rayleigh-Plesset equation (RPE) will be formulated for microdroplets of finite size, taking into account the influence of bubble interactions. The simulation results will be compared with the DNS data available in the literature for superheated LOx droplet in terms of its volumetric expansion over time. The constraints of the numerical solver in simulating the expansion of bubbles utilizing the recently derived RPE will be emphasized. A novel semi-analytical solution for the bubble growth rate will be derived based on the dimensional analysis of the modified RPE. A comparison of the bubble evolution obtained with the semi-analytical and numerical solutions will be discussed. A posteriori computational cost analysis will also be presented for the single droplet cases to demonstrate the benefits of using the semi-analytical solution compared to the numerical solution.

3. Perform a large-eddy simulation of a flash-boiling spray with the newly derived reduced-order bubble growth model using an Eulerian-Lagrangian approach. The in-house code CIAO will be used to perform the LES. The Eulerian approach will be employed to solve the gas phase, treating it as a continuous medium. On the other hand, the Lagrangian approach will be used to solve the liquid phase, which will be regarded as a dispersed

medium. The compressible Navier-Stokes equations will be numerically solved to obtain the gas phase solutions, whereas the dynamics of the spray droplets will be obtained by the solving the Lagrangian equations for droplet transient position, velocity, mass, and temperature. A hybrid breakup model, which incorporates both aerodynamic and flash-boiling induced breakup mechanisms, will be utilized to simulate the breakup. The simulation results will be compared with the experimental data of flash-boiling n-pentane spray in terms of liquid penetration length and steady-state SMD.

4. Develop a 1D cross-sectionally averaged spray (CAS) model for simulating flash-boiling sprays with significantly lower computational cost compared to the 3D simulations. Several physical submodels such as air entrainment, droplet drag, superheated droplet evaporation, flash-boiling induced breakup, and aerodynamic breakup models will be employed in the CAS model. The macroscopic spray characteristics obtained from the CAS model will be compared with the experimental measurements of different injector nozzles and fuels at various flash-boiling conditions. A posteriori computational cost analysis with the 3D and 1D spray simulations will also be highlighted.

1.5 Structure of the Dissertation

This dissertation is arranged as follows: In Chapter 2, the detailed single droplet flash-boiling phenomena considering internal and external vaporization processes will be addressed to achieve the first objective. Chapter 3 and Chapter 4 are dedicated to achieve the second objective. The investigation of the influence of bubble interactions on the dynamics of the vapor bubbles will be described in Chapter 3 and the formulation of the semi-analytical solution for bubble growth rate will be presented in Chapter 4. The 3D spray simulation details will be discussed in Chapter 5 to address the third objective. Finally, Chapter 6 is devoted to the 1D modeling of flash-boiling sprays. The concluding remarks in Chapter 7 marks the end of the dissertation.

2 Modeling of Single Droplet Flash-boiling

2.1 Introduction

Previous studies on single droplet flash-boiling have mainly focused on the dynamics of an isolated bubble growing in an infinite superheated liquid medium. Very few studies explored the fundamental physics associated with bubble growth dynamics while taking into account both internal and external flash vaporization processes. Also, the effect of molecular structure and subsequently the fuel properties on flash-boiling phenomena has not been studied in detail so far.

Resolving each and every detail of the flash-boiling process is highly difficult for large scale spray simulations due to the requirement of huge computational resources. But even if a single spherical liquid blob is fully resolved, the computational cost still remains one of the most important constraints, as also pointed out by Loureiro et al. [82]. Conversely, the LPT technique is one of the most widely adapted and computationally efficient method for single droplet and spray simulations [18, 21, 58, 83, 84]. Therefore, using OME_x as a generic example, the objectives of this chapter are threefold: (1) to study the physics underlying the dynamics of mono-disperse bubble growth in a single droplet configuration using an LPT technique, (2) to study the effect of molecular structure on bubble growth characteristics, and (3) to quantify the relative importance of internal and external flash vaporization in the overall droplet flash vaporization process.

A flash-boiling model is thus integrated in an LPT framework to investigate flash-boiling of OME_x single droplets at different superheating degrees with varying system pressures. The internal vaporization model is based on heterogeneous bubble nucleation due to air as a dissolved gas. To accurately predict the bubble growth rate, the diffusion of thermal energy is linked to the RPE through the prediction of temperature across the liquid-vapor interface. The onset of droplet bursting is modeled by evaluating the critical void fraction of the droplet-bubble system. The external vaporization model is based on the mass transfer due to heat flux from the inner-core of the droplet as well as from the surrounding gas. Simulation results are discussed in terms of the effects of superheating degree, system pressure, and the chain length on different regimes of bubble growth characteristics. Additionally, the influence

of bubble dynamics on overall droplet vaporization is also presented.

The chapter is structured as follows: first, the vaporization models of the superheated droplet are described in Section 2.2. Second, the validation of the simulation results with experiments are presented in Section 2.3. Next, results are discussed in detail in Section 2.4. Finally, the findings are summarized in Section 2.5.

2.2 Flash-boiling Models and Numerical Methods

A two-way coupled Eulerian-Lagrangian framework is used in this study. The compressible Navier-Stokes equations are solved using the in-house code CIAO. The reader is referred to Desjardins et al. [85] and Mittal et al. [86] for more details about the flow solver in CIAO. In this section, the equations describing the superheated dispersed phase will be introduced. First, the internal vaporization model will be discussed. Second, the external vaporization model and, subsequently, the solution procedure of both vaporization models will be presented.

2.2.1 Internal Vaporization

The internal vaporization process of a superheated single droplet can be classified into three stages: (1) bubble nucleation, (2) bubble growth, and (3) droplet burst. A schematic of these stages is shown in Fig. 2.1.

Bubble Nucleation

Nuclei may form either via homogeneous or heterogeneous nucleation depending on the superheating degree of the liquid droplet. Although the former one is difficult to obtain unless the superheating degree is very high, the latter occurs easily in the presence of any crevices on the solid surface, fine dust particles or mixed or dissolved gases in the liquid [19, 58]. In this study, we neglect the nucleation process owing to the dust particles. Only heterogeneous nucleation due to air as a dissolved gas is considered. In the view of such nucleation process, it has been experimentally shown that the number density of the bubble nuclei increases exponentially with the degree of superheating [87, 88]. The bubble number density is expressed based on the approximation suggested by Senda et al. [19] as

$$n = 5.757 \times 10^{12} \cdot \exp\left(\frac{-5.279\,\mathrm{K}}{\Delta\theta}\right), \tag{2.1}$$

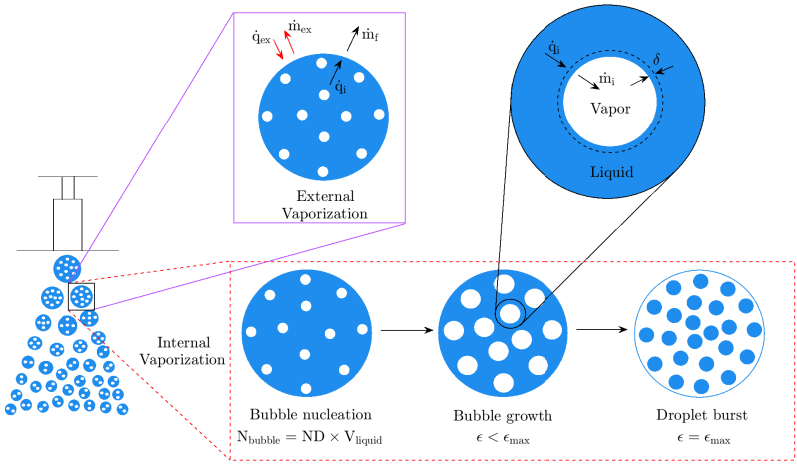

Figure 2.1: Schematic of the flash-boiling process.

where $\Delta\theta$ is the superheating degree of the liquid droplet, introduced by Senda et al. [19] as $\Delta\theta = T_{\mathrm{inj}} - T_{\mathrm{b}}\,(P_{\mathrm{l}})$. T_{inj} denotes the injection temperature of the droplet and T_{b} the droplet boiling temperature corresponds to the liquid pressure, P_{l}. The present study does not consider the polydispersity of the vapor bubbles but assumes mono-disperse bubbles, which are spaced sufficiently apart from each other such that the interaction between the adjacent bubbles' boundary layers can be neglected. These assumptions may get violated with increasing superheating degree due to the presence of large number of vapor bubbles. The validity of these assumptions will be highlighted in more detail in Section 2.4.

Bubble Growth

Neglecting the liquid viscosity, one-dimensional mass and momentum conservation equations leads to the RPE, which describes the growth process of a spherically symmetric vapor bubble and is used here to compute the growth rate of the bubble, $\mathrm{d}R_{\mathrm{b}}/\mathrm{d}t$. A quantitative justification of neglecting the

liquid viscosity is given in Appendix A. The resulting RPE is given as [89]

$$\underbrace{P_{\mathrm{v}}\left(T_{\mathrm{v}}\right)-P_{\mathrm{l}}}_{\Delta P}=\underbrace{\rho_{\mathrm{l}}R_{\mathrm{b}}\frac{\mathrm{d}^2R_{\mathrm{b}}}{\mathrm{d}t^2}+\frac{3}{2}\rho_{\mathrm{l}}\left(\frac{\mathrm{d}R_{\mathrm{b}}}{\mathrm{d}t}\right)^2}_{P_{\mathrm{hd}}}+\underbrace{\frac{2\sigma}{R_{\mathrm{b}}}}_{P_{\sigma}}, \tag{2.2}$$

where ρ_{l} denotes the liquid density, R_{b} the bubble radius, σ the surface tension of the liquid, P_{v} the saturated vapor pressure, and T_{v} the vapor temperature, which is assumed to be equal to the liquid temperature at the bubble surface. Since the droplet considered in this study is much larger than the bubble, it is assumed that P_{l} is the same as the surrounding gas pressure, P_{g}, neglecting the surface tension between droplet and gas. In Eq. (2.2), ΔP denotes the pressure differential at the liquid-vapor interface, P_{hd} represents the hydrodynamic pressure resulting from the bulk liquid motion at the bubble wall, and P_{σ} indicates the pressure due to the surface tension force at the interface. Assuming static equilibrium at $t = 0$, i.e., $\mathrm{d}R_{\mathrm{b}}/\mathrm{d}t = 0$, the critical radius at which the surface tension force is balanced by the pressure difference at the interface can be expressed as

$$r(t=0)=R_{\mathrm{c}}=\frac{2\sigma}{P_{\mathrm{v}}\left(T_{\mathrm{v}}\right)-P_{\mathrm{g}}}. \tag{2.3}$$

It has to be noted that the influence of bubble-bubble interactions and the finite droplet size effects on the bubble dynamics are not considered here and will be studided in the next chapter. The RPE describes the evolution of the bubble radius for a given P_{v}. In the absence of vaporization, the bubble radius given by Eq. (2.2) will not change anymore. For a superheated droplet, an energy flux from the liquid to the bubble surface causes vaporization, which increases the mass and the pressure inside the bubble. This leads to a driving pressure differential, ΔP, in Eq. (2.2). The saturated vapor pressure is determined from the solution of the energy equation inside the droplet, where the temperature inside the bubble is assumed to be homogeneous. Assuming that the bubble surface is at saturation temperature, integrating the energy equation across the interface gives

$$\rho_{\mathrm{v}}L_{\mathrm{v}}\frac{\mathrm{d}R_{\mathrm{b}}}{\mathrm{d}t}+L_{\mathrm{v}}\frac{R_{\mathrm{b}}}{3}\frac{\mathrm{d}\rho_{\mathrm{v}}}{\mathrm{d}t}=\lambda_{\mathrm{l}}\left(\frac{\partial T}{\partial r}\right)_{\mathrm{r=R_b}}, \tag{2.4}$$

where ρ_{v} is the saturated vapor density, L_{v} the latent heat of vaporization at T_{v}, and λ_{l} the liquid thermal conductivity.

Donne and Ferranti [54] and Lee and Merte [47] solved the complete energy equation to obtain $\left(\partial T/\partial r\right)_{\mathrm{r=R_b}}$ from the resolved temperature field. In

contrast, a thin boundary layer assumption around the bubble allows to model $(\partial T/\partial r)_{\mathrm{r=R_b}}$ without resolving the temperature field inside the droplet. This assumption is valid when Ja > 2 [51] and it confines the effect of diffusion of the thermal energy to a thin region of thickness δ adjacent to the bubble surface.

In the present work, to allow for efficient simulations, Board and Duffey [90] model is used to obtain $(\partial T/\partial r)_{\mathrm{r=R_b}}$, where a linear temperature drop is assumed to exist across a thin thermal boundary layer of thickness, $\delta = \left((\pi/3)\,\alpha_{\mathrm{l}} t\right)^{1/2}$ (schematic shown in Fig. 2.1), such that

$$\left(\frac{\partial T}{\partial r}\right)_{\mathrm{r=R_b}} = \frac{T_{\mathrm{d}} - T_{\mathrm{v}}}{\delta}, \tag{2.5}$$

where T_{d} is the droplet bulk temperature and α_{l} the thermal diffusivity of the liquid. t in the expression of δ denotes the time which is estimated from the inception of the bubble growth. Substituting Eq. (2.5) into Eq. (2.4), using the expression for δ and the ideal gas law yields a relation for the vapor temperature as

$$\frac{P_{\mathrm{v}} W_{\mathrm{l}}}{\mathcal{R} T_{\mathrm{v}}} L_{\mathrm{v}} \frac{\mathrm{d}R_{\mathrm{b}}}{\mathrm{d}t} + L_{\mathrm{v}} \frac{R_{\mathrm{b}}}{3} \frac{\mathrm{d}}{\mathrm{d}t}\left(\frac{P_{\mathrm{v}} W_{\mathrm{l}}}{\mathcal{R} T_{\mathrm{v}}}\right) = \lambda_{\mathrm{l}} \frac{T_{\mathrm{d}} - T_{\mathrm{v}}}{\delta}, \tag{2.6}$$

where $\mathcal{R}$ is the universal gas constant and W_{l} the molar mass of the liquid. Eq. (2.2) and Eq. (2.5) depend on each other and need to be solved together to obtain the interface dynamics. The driving pressure-differential imposed by the energy equation is then balanced in the RPE by either the hydrodynamic terms (inertia-controlled regime), the surface tension term (surface tension-controlled regime), or both (transition regime). The vaporization rate due to bubble growth is given by

$$\dot{m}_{\mathrm{i}} = \left\{ 4\pi R_{\mathrm{b}}^2 \frac{\mathrm{d}R_{\mathrm{b}}}{\mathrm{d}t} \rho_{\mathrm{v}} \right\} N_{\mathrm{bub}}, \tag{2.7}$$

N_{bub} denotes the number of bubbles calculated as $N_{\mathrm{bub}} = n \times V_{\mathrm{drop}}$, where V_{drop} is the initial droplet volume.

Droplet Burst

The droplet is considered to burst when the void fraction (ϵ) reaches its critical value. In this study, the void fraction is defined as [19]

$$\epsilon = \frac{V_{\mathrm{bub}}}{V_{\mathrm{bub}} + V_{\mathrm{liq}}}, \tag{2.8}$$

Literature	ϵ_{crit}
Suma and Koizumi [87]	0.51-0.53
Senda et al. [19]	0.45
Adachi et al. [25]	0.45
Sher et al. [44]	0.48
Kawano et al. [58]	0.55
Li et al. [22]	0.50

Table 2.1: Critical void fraction values.

where V_{bub} is the total volume of the vapor bubbles and V_{liq} the volume of the liquid in the droplet. The typical critical values of ϵ reported in previous studies are summarized in Table 2.1. The critical void fraction value of 0.55 is chosen in this dissertation, as suggested by Kawano et al. [58].

2.2.2 External vaporization

Vaporization from the droplet external surface consists of two parts, namely the vaporization due to the internal heat transfer, $\dot{q}_{\mathrm{i}}$, if the temperature of the droplet is at superheated conditions, and the external heat transfer, $\dot{q}_{\mathrm{ex}}$, if the temperature of the surrounding gas is higher than the droplet boiling temperature (schematic shown in Fig. 2.1). The rate of vaporization due to heat transfer from the droplet interior to the external droplet surface, $\dot{q}_{\mathrm{i}}$, is modeled as [25]

$$\dot{m}_{\mathrm{f}} = \frac{h_{\mathrm{f}} \left(T_{\mathrm{d}} - T_{\mathrm{b}}\right) A_{\mathrm{d}}}{L_{\mathrm{v}} \left(T_{\mathrm{b}}\right)}, \tag{2.9}$$

where $\dot{m}_{\mathrm{f}}$ denotes the flash boiled vapor mass flow rate, h_{f} the flashing heat transfer coefficient, A_{d} the droplet surface area, and $L_{\mathrm{v}}(T_{\mathrm{b}})$ the latent heat of the liquid at the boiling temperature, T_{b}, which depends on the surrounding gas pressure. To evaluate the heat transfer coefficient, Adachi et al. [25] proposed the following empirical functions from their experimental measurements of n-pentane spray:

$$h_{\mathrm{f}} = \begin{cases} 0.76 \left(T_{\mathrm{d}} - T_{\mathrm{b}}\right)^{0.26} & (0 < T_{\mathrm{d}} - T_{\mathrm{b}} < 5) \\ 0.027 \left(T_{\mathrm{d}} - T_{\mathrm{b}}\right)^{2.33} & (5 < T_{\mathrm{d}} - T_{\mathrm{b}} < 25) \\ 13.8 \left(T_{\mathrm{d}} - T_{\mathrm{b}}\right)^{0.39} & (T_{\mathrm{d}} - T_{\mathrm{b}} > 25), \end{cases} \tag{2.10}$$

where the temperature is expressed in K and the heat transfer coefficient in kW/(m^{2}K).

To consider vaporization due to the heat flux from the environment surrounding the droplet, $\dot{m}_{\mathrm{ex}}$, the standard droplet vaporization model [91] cannot be used here, because, for the flash-boiling droplets, $\dot{m}_{\mathrm{f}}$ induces an additional Stefan flow, which can significantly reduce the heat flux to the droplet surface from the surroundings and therefore needs to be considered in the film model. Assuming spherical symmetry for the droplet and a static heat transfer process, the energy equation can be integrated in the radial direction to obtain the mass flow rate due to $\dot{q}_{\mathrm{ex}}$ during superheated condition as [68]

$$\dot{m}_{\mathrm{ex}} = 2\pi \frac{\lambda_{\mathrm{g}}}{C_{\mathrm{p,g}}} R_{\mathrm{d}} \frac{\mathrm{Nu_d}}{\left(1+\frac{\dot{m}_{\mathrm{f}}}{\dot{m}_{\mathrm{ex}}}\right)} \ln\left[1+\left(1+\frac{\dot{m}_{\mathrm{f}}}{\dot{m}_{\mathrm{ex}}}\right)\frac{C_{\mathrm{p,g}}\left(T_{\mathrm{g}}-T_{\mathrm{s}}\right)}{L_{\mathrm{v}}\left(T_{\mathrm{s}}\right)}\right], \quad (2.11)$$

where T_{s} is the droplet surface temperature, which is assumed to be equal to the liquid boiling temperature during superheated conditions. λ_{g} and $C_{\mathrm{p,g}}$ are the gas-phase thermal conductivity and specific heat capacity, respectively, calculated using one-third rule [92]. R_{d} is the droplet radius, T_{g} the gas-phase temperature, and $\mathrm{Nu_d}$ the droplet Nusselt number. In this study, $\mathrm{Nu_d} = 2$, since the droplet and the surrounding gas are considered to be stationary. Combining Eq. (2.9) and Eq. (2.11) yields the total vapor mass flow rate from the droplet surface as

$$\dot{m}_{\mathrm{t}} = \dot{m}_{\mathrm{f}} + \dot{m}_{\mathrm{ex}}. \quad (2.12)$$

The droplet bulk temperature is calculated using the infinite conductivity model as

$$\frac{\mathrm{d}T_{\mathrm{d}}}{\mathrm{d}t} = \frac{\mathrm{Nu_d}}{3\mathrm{Pr_g}} \frac{C_{\mathrm{p,g}}}{C_{\mathrm{l}}} \frac{f_2}{\tau_{\mathrm{d}}} \left(T_{\mathrm{g}}-T_{\mathrm{s}}\right) - \frac{\dot{m}_{\mathrm{t}} L_{\mathrm{v}}\left(T_{\mathrm{s}}\right)}{m_{\mathrm{d}} C_{\mathrm{l}}}. \quad (2.13)$$

where $\mathrm{Pr_{gg}}$ denotes gas-phase Prandtl number, m_{d} the droplet mass and τ_{d} the particle time constant defined as $\tau_{\mathrm{d}} = 2\rho_{\mathrm{l}} R_{\mathrm{d}}^2 / \left(9\mu_{\mathrm{g}}\right)$, where μ_{g} is the dynamic viscosity of the surrounding gas. The factor f_2 is an analytical evaporative heat transfer correction to the solid sphere Nusselt number and is defined as [91]

$$f_2 = \beta/(\exp(\beta)-1), \qquad \beta = -\left(\frac{3\mathrm{Pr_g}\tau_{\mathrm{d}}}{2}\right)\frac{\dot{m}_{\mathrm{t}}}{m_{\mathrm{d}}}. \quad (2.14)$$

It is to be noted that the rate of change of liquid mass (Eq. (2.7)) due to bubble growth does not have any influence on T_{d} due to thin thermal boundary layer

assumption. Thus, the mass flow due to $\dot{q}_{\mathrm{i}}$ and $\dot{q}_{\mathrm{ex}}$ will only be responsible for changing T_{d}.

2.2.3 Solution Procedure

A flow chart illustrating the calculation procedure of a single droplet flash-boiling is shown in Fig. 2.2. After the flow field is initialized, a single droplet is positioned into the computational domain and the bubble number density is evaluated. Subsequent steps involve setting up the parameters at t_0 and perturbing the bubbles' critical radius by ΔR_{b} over Δt to initiate the growth process. These allow the evaluation of the bubble growth rate at the next time-step, $t_1 = t_0 + \Delta t$. After that, the bubbles' surface temperature is calculated using Eq. (2.6) and the vapor generation rate is obtained through Eq. (2.7). Thereafter, if the critical void fraction is not reached, the droplet mass and radius are updated due to internal bubble expansion. Then the vapor generation rate from the external surface of the droplet and rate of change of droplet bulk temperature are calculated using Eq. (2.12) and Eq. (5.27), respectively. The properties of the droplet-bubble system are then updated based on the external vaporization calculations. The flow field is kept frozen while updating the dispersed phase at the new time-step. It is advanced only after transferring the source term of the dispersed phase into the Eulerian phase. A new time step is then initiated with the evaluation of the bubble growth rate at $t_1 + \Delta t$ using Eq. (2.2). Note that Eq. (2.2), Eq. (2.7), Eq. (2.12), and Eq. (5.27) are advanced using a second-order Runge-Kutta scheme, whereas Eq. (2.6) is iteratively solved using the Newton-Raphson method. It is worth noting that Eq. (2.6) could also be solved using an explicit approach. However, the choice to iteratively determine the vapor temperature through an implicit method is made in pursuit of enhanced accuracy and consistency. It enables to accurately and consistently compute the vapor temperature, particularly in situations where explicit method requires overly restrictive step sizes.

2.3 Model Validation

To the best of the authors' knowledge, experimental data for flash-boiling of $\mathrm{OME_x}$ single droplet considering internal and external vaporization are not available in the literature. Therefore, a comprehensive validation of the models used in this study is beyond the scope of this article. However, there are numerous experimental data available for bubble growth in a uniformly

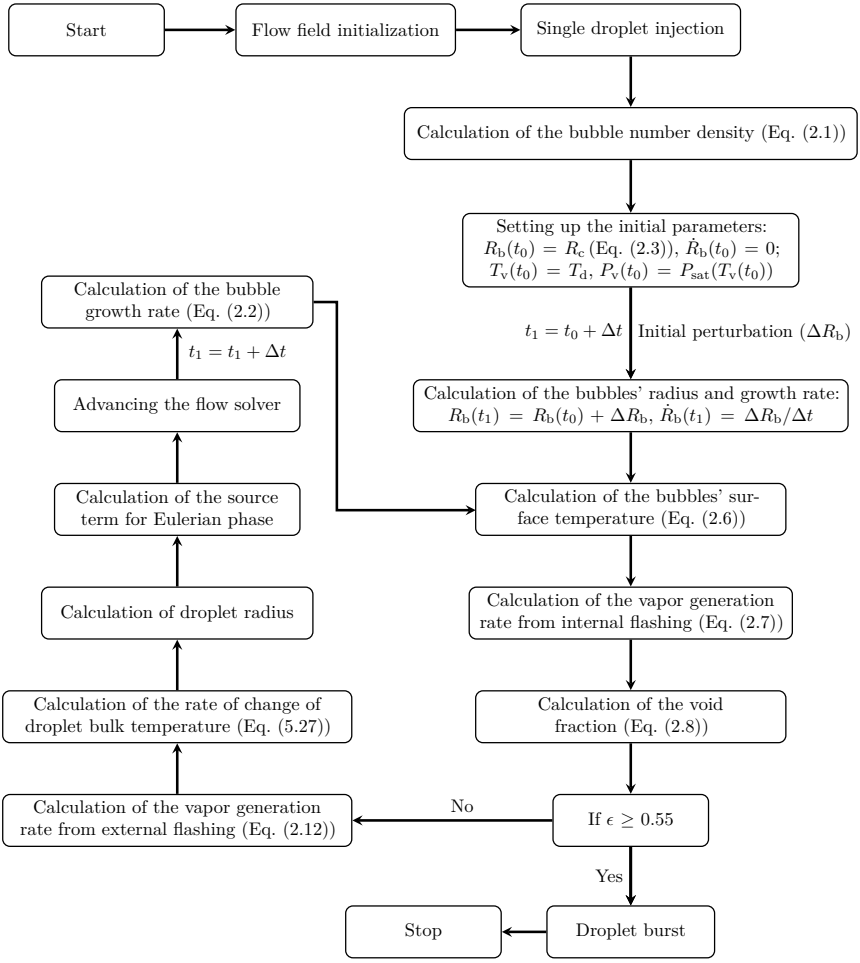

Figure 2.2: Flow chart for the calculation of the single droplet flash-boiling in CIAO.

superheated bulk water. The present flash-boiling models are thus tested in terms of internal vaporization against the measurements performed by Lien [53] for three different levels of superheating. The external vaporization models presented in this chapter have been extensively validated in the

previous literature for spray cases [25, 38, 68, 93, 94].

Lien [53] performed experiments for a single bubble growing in a uniformly superheated pool of water. A single vapor bubble in a relatively large droplet is considered in the present simulation to replicate the experimental conditions. Since the evaporation from the free surface was suppressed in the experiment, we neglect the external evaporation while simulating the superheated water cases. The ambient temperature is set to 273 K for all three simulated cases. The bubble critical radius is perturbed by $10^{-8}\%$ over a time interval of 100 ns. Fig. 2.3 shows that the bubble radii predicted by the present model are in reasonable agreement with Lien [53] experimental results.

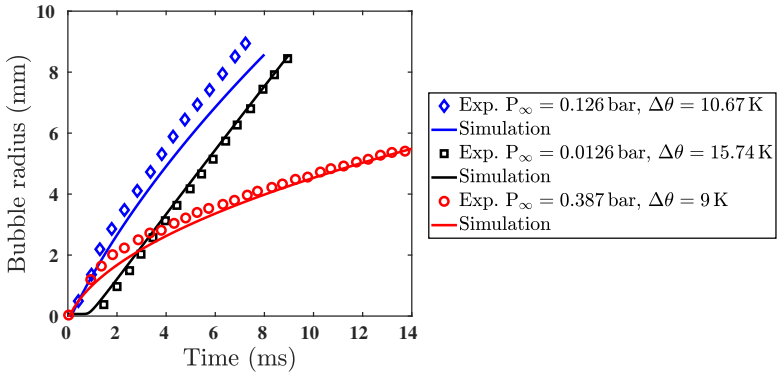

Figure 2.3: Comparison of the superheated water bubble radius evolution from the present numerical simulation with the experimental measurements of Lien [53].

2.4 Results and Discussion

The flash-boiling of OME_x single droplets with a diameter of 200 μm is investigated at low ambient pressures with varying superheating degrees. A square box of size 0.54 m × 0.54 m × 0.54 m with no-slip adiabatic walls with a temperature of 323 K is considered as the computational domain. The stationary single droplet is placed at the center of the box. Nitrogen is used as ambient gas, and the chemistry of the gas phase is neglected. To initiate the bubble growth process, the critical radius of the bubbles is perturbed by $10^{-4}\%$ over a time interval of 1 ns.

The thermophysical properties of OME_1 and OME_1 are obtained from Daubert and Danner [95] and Jacobs et al. [96], while for OME_4, experimental measurements of Safarov et al. [97] as well as group contribution methods (GCM) are used to obtain the thermophysical properties. Some of the properties, such as surface tension, heat capacity, thermal conductivity, and viscosity, have been extrapolated beyond the measured range. To ensure that this procedure would provide a sufficiently accurate approximation, the extrapolated properties are compared with those predicted using the theoretical methods. However, it is to be noted that this comparison is done only to verify if trends in the extrapolated range are captured and absolute comparison is not intended. The comparison of the theoretical prediction of the thermophysical properties with the experimental measurements is shown in Appendix B.

In this section, first, the bubble growth characteristics of the OME_1 droplet will be presented. Second, the effects of superheating degree and system pressure on the growth characteristics for OME_1 droplets will be discussed. Third, the influence of the chain length on the bubble dynamics will be investigated. Fourth, the importance of the bubble dynamics on the overall droplet vaporization will be examined.

2.4.1 Bubble Dynamics of Dimethoxymethane Single Droplet

Bubble dynamics of OME_1 single droplet will be discussed here for $\Delta\theta = 47$ K. Unlike in previous studies that characterized the dynamics of bubble growth into four phases for high enough superheating degrees [45], it is here observed that only three growth phases are present: (1) surface tension-controlled (ST) phase, (2) transition phase (T), and (3) inertia-controlled phase (IC). The thermal diffusion-controlled (TD) growth phase is not observed here, since the droplets explode near the end of the inertia-controlled phase.

Surface Tension-controlled (ST) Phase

Surface tension is the main controlling parameter that influences the growth dynamics of vapor bubble nuclei at the very beginning of the growth process. In this stage, the radius of the bubbles remains near to its critical value, 0.221 μm, over a significant period of time, as shown in Fig. 2.4. Although there is a continuous supply of energy from the surrounding superheated liquid into the bubbles, as observed from the positive interface temperature gradient in Fig. 2.5. This contribution is so small that $\mathrm{d}R_\mathrm{b}/\mathrm{d}t$ and also $\mathrm{d}^2R_\mathrm{b}/\mathrm{d}t^2$ are irrelevant with respect to the other terms in the equation of motion

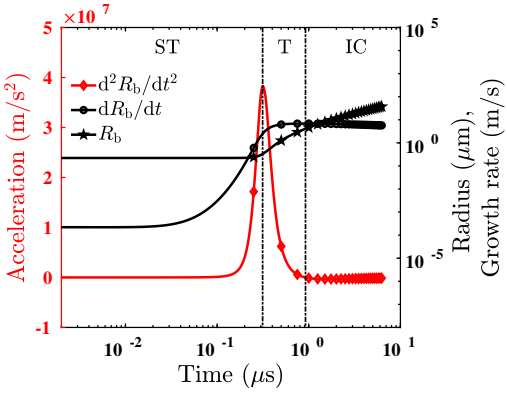

Figure 2.4: Growth curve and the interface acceleration over time for OME_1 vapor bubbles at $P_g = 0.3\,\text{bar}$, $T_g = 323\,\text{K}$, and $\Delta\theta = 47\,\text{K}$.

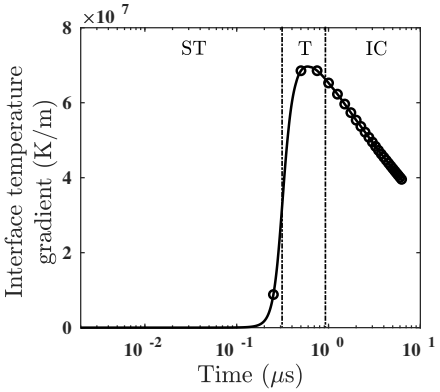

Figure 2.5: The temperature gradient histories at the bubbles' surface of vapor bubbles in OME_1 droplet for $P_g = 0.3\,\text{bar}$, $T_g = 323\,\text{K}$, and $\Delta\theta = 47\,\text{K}$.

(Eq. (2.2)), as depicted in Fig. 2.7a. This eventually reduces Eq. (2.2) to $\Delta P = P_v - P_g \approx 2\sigma/R_b$. The energy equation results in the driving pressure differential required for bubble growth. As the bubble grows in size, liquid temperature at the bubble surface (T_l) decreases. In this study, since it is assumed that $T_l = T_v$, a small increase in radius also decreases the vapor

temperature, T_v and because of the equilibrium assumption also to lower P_v. The lower T_v causes a higher temperature gradient at the interface, as depicted in Fig. 2.5. Due to the negligible effect of compressibility [45], Eq. (2.4) can also be expressed as follows

$$\rho_\mathrm{v} L_\mathrm{v} \frac{\mathrm{d}R_\mathrm{b}}{\mathrm{d}t} \approx \lambda_\mathrm{l} \left(\frac{\partial T}{\partial r} \right)_{\mathrm{r=R_b}}, \tag{2.15}$$

which dictates that the bubble growth rate is eventually proportional to the interface heat flux. Thus, the higher $(\partial T/\partial r)_{\mathrm{r=R_b}}$ will give rise to a higher bubble growth rate, engendering a further reduction in T_v, and escalating the temperature gradient at the interface. Thus, a positive thermal feedback is created, the effect of which is minimal in the initial period of the surface tension-controlled phase (ΔT in Fig. 2.6 rises only from zero to 0.041 K in the first 0.156 μs) but becomes relevant in the later period (ΔT in Fig. 2.6 increases to 5.241 K in the next 0.16 μs) such that growth rate, interface acceleration, and bubbles' radius appear to show a dramatic increase after 0.156 μs. The maximum rate of change of ΔT occurs at 0.316 μs, when also the interface acceleration reaches its peak value. This is the time that marks the onset of significant bubble growth and the end of the surface tension-controlled phase.

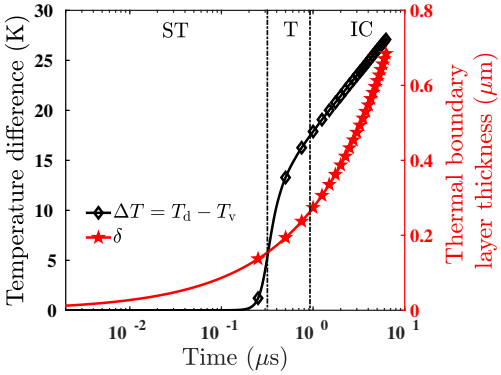

Figure 2.6: The variation of the thermal boundary layer thickness (δ) and the temperature difference (ΔT) of vapor bubbles in $\mathrm{OME_1}$ droplet for $P_\mathrm{g} = 0.3\,\mathrm{bar}$, $T_\mathrm{g} = 323\,\mathrm{K}$, and $\Delta\theta = 47\,\mathrm{K}$.

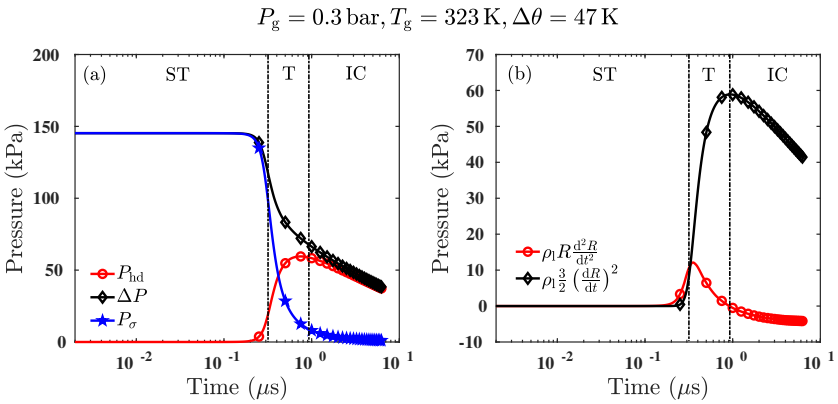

Figure 2.7: (a) Variation of the hydrodynamic pressure (P_{hd}), pressure due to the surface tension force (P_σ), and the pressure difference (ΔP) in the three distinct growth phases: surface tension-controlled (ST) phase, transition phase (T), and inertia-controlled phase (IC). (b) Relative contribution of velocity and acceleration in constituting the hydrodynamics pressure term in Eq. 2.2.

Transition Phase (T)

A rapid increase of the interface acceleration during the later period of the surface tension-controlled phase slowly generates the liquid motion that is responsible for increasing P_{hd} at the beginning of the transition phase, as shown in Fig. 2.7a. The hydrodynamic force, faced by the growing bubbles, has the potential to suppress the positive thermal feedback, as seen from the decrease in the slope of ΔT in Fig. 2.6. Consequently, both $\mathrm{d}R_b/\mathrm{d}t$ and $(\partial T/\partial r)_{R_b}$ increase in a less rapid manner, as illustrated in Fig. 2.4 and Fig. 2.5, respectively. Also, the decrease in the rate of change of $(\partial T/\partial r)_{R_b}$ causes the sharp decrease of the interface acceleration (Eq. (2.15)) from 3.826×10^7 m/s^2 to 1.158×10^3 m/s^2 within 0.601 μs, as shown in Fig. 2.4.

Fig. 2.7a shows the maximum value of P_{hd} at 0.75 μs, which indicates the significant liquid motion in the later period of the transition phase. Furthermore, it can be observed that the effect of the surface tension diminishes, as P_{hd} is balanced by the ΔP. The transition phase is considered to end at 0.917 μs, which corresponds to the maximum bubble growth rate.

Inertia-controlled Phase (IC)

In this region, only the liquid inertia plays an important role in balancing the equation of motion ($\Delta P = P_\mathrm{v} - P_\mathrm{g} \approx P_\mathrm{hd}$), as can be seen in Fig. 2.7a. The bubbles have grown so large, reaching a radius of about 4.054 μm at the beginning of this phase that the forces due to the surface tension become unimportant with respect to P_hd. Fig. 2.7b shows the contribution of the two inertial terms that constitute P_hd. The negative values of the acceleration term indicate that the liquid surrounding the bubbles has started decelerating irrespective of the continuous increase in ΔT. This phenomenon is a direct consequence of the rapid thickening of the thermal boundary layer, which outweighs the thermal feedback and causes $(\partial T/\partial r)_{R_\mathrm{b}}$ to decrease in this region, as depicted in Fig. 2.5. Since the temperature gradient decreases, the growth rate must decrease as predicted by Eq. (2.15) and visualized in Fig. 2.4.

Fig. 2.4 depicts that the size of the vapor bubbles is increased to 38.37 μm immediately prior to the droplet burst, which is almost 174.4 times that of the critical radius. Thus, it is very likely that the inter-bubble spacing becomes much smaller, which eventually increases the chances of bubble coalescence during the later stages of the bubble growth for high superheating degree [82]. Therefore, further investigations of the proposed model with the experimental measurements of superheated single droplet are warranted to explore the influence of the assumptions that the bubbles are mono-disperse and that they remain far away from each other on the bubble growth dynamics and the onset of droplet bursting.

2.4.2 Effect of Superheating Degree

Fig. 2.8 shows the variation in the bubble growth characteristics of $\mathrm{OME_1}$ single droplet for the superheating degree ranging from $\Delta\theta = 47\,\mathrm{K}$ to $\Delta\theta = 6\,\mathrm{K}$ (cases 'HS-LP', 'MS-LP', and 'LS-LP' in Table 2.2) at an ambient pressure of $P_\mathrm{g} = 0.3$ bar.

It can be observed from Fig. 2.8a that the critical radius of the vapor bubbles increases with decreasing superheating degree. To a lower superheating degree corresponds a lower droplet temperature, and consequently also a lower initial vapor pressure. This one, in turn, causes the critical radius to increase, as expressed in Eq. (2.3). The delay time, which is defined as the time interval between the initial disturbance and the onset of significant bubble growth, also increases substantially with decreasing superheating degree. Fig. 2.8a shows that it rises from 0.316 μs for the highest superheating degree value to

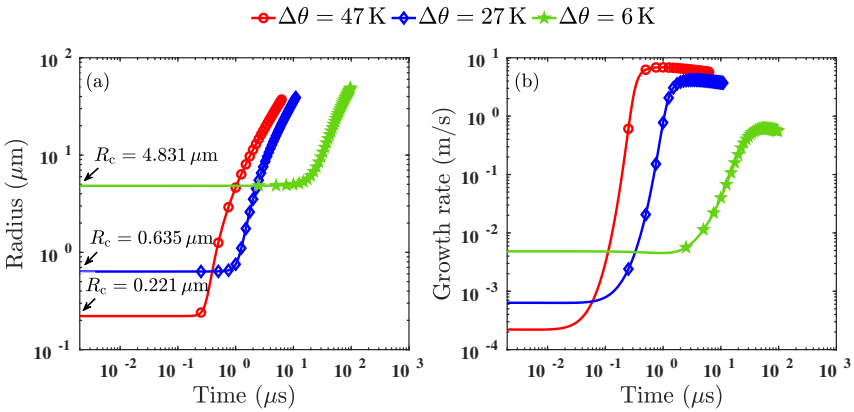

Figure 2.8: Growth characteristics of the vapor bubbles in OME_1 droplet at $P_g = 0.3\,\text{bar}$ and $T_g = 323\,\text{K}$ with varying superheating degrees of $\Delta\theta = 47\,\text{K}$, $\Delta\theta = 27\,\text{K}$, and $\Delta\theta = 6\,\text{K}$. Subfigures (a) and (b) represent the radius and the growth rate variation over time.

21.54 μs for the lowest one.

As the rate of change of vapor pressure is inversely related to the square of the bubbles' radius (Eq. (2.3)), a very small change in the radius would lead to a significant drop in the vapor pressure and the temperature for smaller critical nuclei. Thus, the thermal feedback, which is directly related to the temperature difference, ΔT, is markedly enhanced when the system superheating degree is maximum. A stronger thermal feedback results in a higher interface temperature gradient, and thus, a higher growth rate

Case ↓	T_g	P_g	T_d	$\Delta\theta$
Unit →	K	bar	K	K
High superheat-low pressure (HS-LP)	323	0.3	331.72	47
Medium superheat-low pressure (MS-LP)	323	0.3	311.72	27
Low superheat-low pressure (LS-LP)	323	0.3	290.72	6
Medium superheat-medium pressure (MS-MP)	323	0.5	323.63	27
Medium superheat-high pressure (MS-HP)	323	0.7	332.16	27

Table 2.2: Operating conditions of OME_1 for the numerical simulations.

(Eq. (2.15)), and shorter delay time, as shown in Fig. 2.8b and Fig. 2.8a, respectively. The peak interface acceleration is also increased from 2.601×10^4 m/s^2 to 3.826×10^7 m/s^2 due to a higher rate of change in the temperature gradient at the interface. These quantities are illustrated in the two panels of Fig. 2.9 respectively.

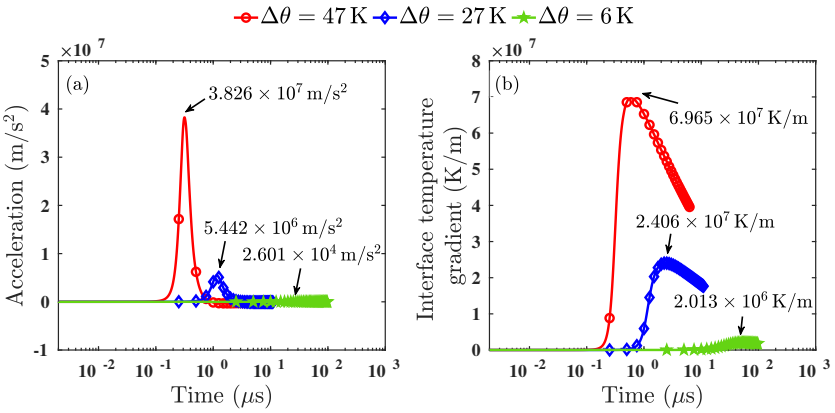

Figure 2.9: Variation of (a) the interface acceleration and (b) the temperature gradient for $P_g = 0.3$ bar, $T_g = 323$ K with varying degrees of system superheat, $\Delta\theta = 47$ K, $\Delta\theta = 27$ K, and $\Delta\theta = 6$ K.

Fig. 2.10 indicates that the higher superheating degree is responsible for a significant increase in liquid motion surrounding the bubbles. The increase in peak hydrodynamic pressure from 0.522 kPa to 59.528 kPa as the superheating degree rises from 6 K to 47 K is because of the stronger thermal feedback associated with it. Also the time at which the maximum value of P_{hd} is attained, changes drastically from 44.222 μs to 0.75 μs. This is because a more intense thermal feedback causes the bubbles to grow at a faster rate, creating a noticeable liquid motion within a very short period of time. However, the higher hydrodynamic pressure has also an adverse impact on the thermal feedback, due to which the vapor pressure drops at a much slower rate. This mechanism eventually helps in sustaining a considerable pressure difference over an extended period of time, and increasing the duration of the inertia-controlled phase at the highest superheating degree.

A particularly interesting aspect is found for case 'LS-LP': the absence of the inertia-controlled phase, as shown in Fig. 2.10c. In this case, the bubble growth dynamics in the transition phase are mainly controlled by the surface tension

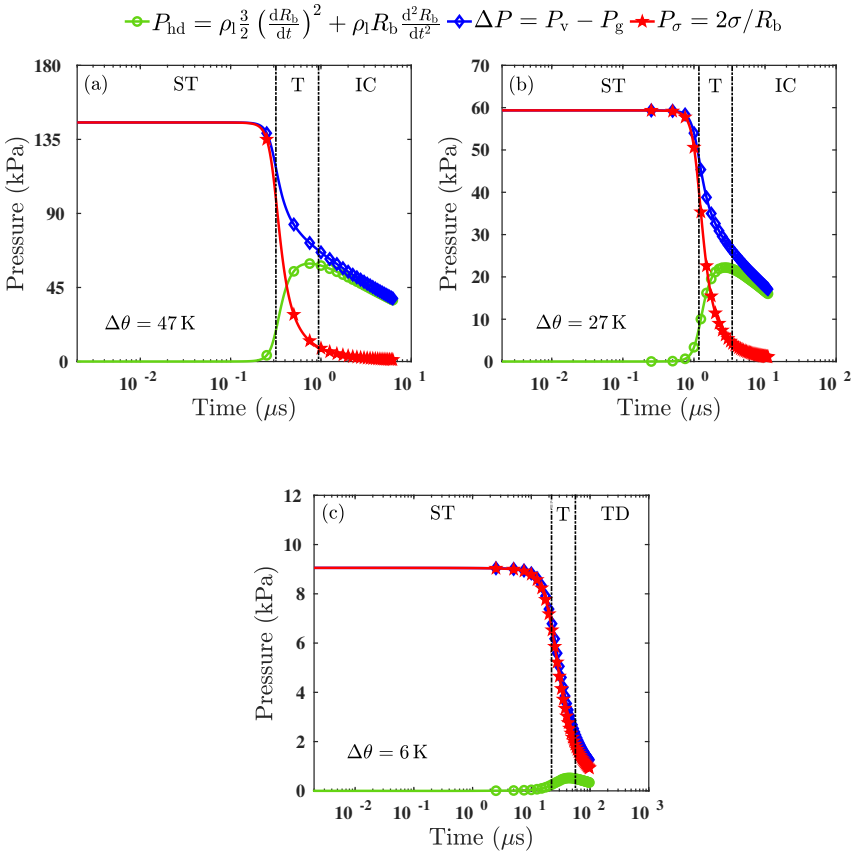

Figure 2.10: The dependency of the rate of change of ΔP on the hydrodynamic pressure at $P_{\mathrm{g}} = 0.3\,\mathrm{bar}$, $T_{\mathrm{g}} = 323\,\mathrm{K}$ for differing system superheat of (a) $\Delta\theta = 47\,\mathrm{K}$, (b) $\Delta\theta = 27\,\mathrm{K}$, and (c) $\Delta\theta = 6\,\mathrm{K}$.

and the heat transfer from the superheated liquid into the bubbles, as the effect of liquid inertia is negligibly small. Here, the equation of motion throughout the growth phase can be approximated by $\Delta P = P_{\mathrm{v}} - P_{\mathrm{g}} \approx 2\sigma/R_{\mathrm{b}}$. After the transition phase, the thermal difussion gradually becomes the rate-controlling factor of bubble growth as ΔP diminishes to zero.

2.4.3 Effect of Pressure

Bubble growth characteristics at superheating degree of $\Delta\theta = 27\,\mathrm{K}$ with varying system pressure values from $P_g = 0.3\,\mathrm{bar}$ to $P_g = 0.7\,\mathrm{bar}$, cases 'MS-LP', 'MS-MP', and 'MS-HP' in Table 2.2, are depicted in Fig. 2.11. Fig. 2.11a shows that the increasing system pressure at constant superheating degree produces critical nuclei of a smaller size (Eq. (2.3)). The delay time is also reduced by almost two times for the highest pressure case ($t_{\mathrm{delay}} = 0.547\,\mu\mathrm{s}$) in comparison to the lowest pressure case ($t_{\mathrm{delay}} = 1.158\,\mu\mathrm{s}$). The smaller critical nuclei also enhance the thermal feedback effect, as shown in Fig. 2.12b, following the same mechanism discussed in Section 2.4.2. This, in turn, leads to higher growth rate and higher interface acceleration for the high-pressure system, as depicted in Fig. 2.11b and Fig. 2.12a, respectively. However, the rate at which the interface temperature gradient decreases in the inertia-controlled phase increases substantially with increasing system pressure, as shown in Fig. 2.12b. Moreover, this phenomenon lowers the rate at which the bubbles expand for the high-pressure system in this growth phase, as illustrated in Fig. 2.11b.

The influence of hydrodynamic pressure on the rate of change of ΔP is shown in Fig. 2.13 for varying system pressure. It can be observed that the

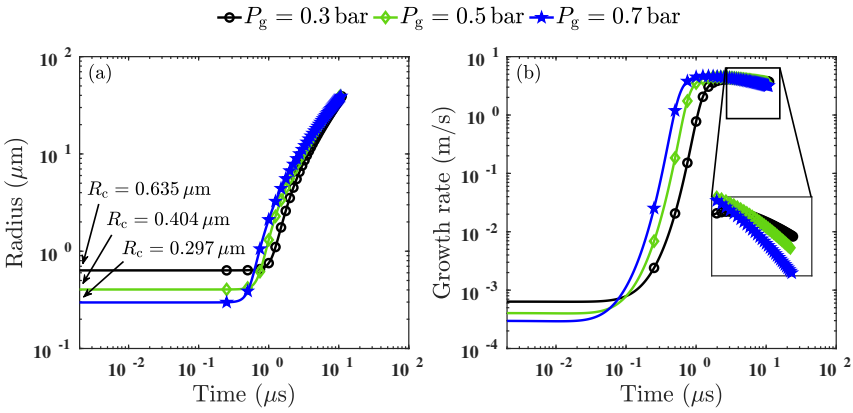

Figure 2.11: Growth characteristics of the vapor bubbles in OME_1 droplet at $T_g = 323\,\mathrm{K}$ and $\Delta\theta = 27\,\mathrm{K}$ with varying system pressures of $P_g = 0.3\,\mathrm{bar}$, $P_g = 0.5\,\mathrm{bar}$, and $P_g = 0.7\,\mathrm{bar}$. Subfigures (a) and (b) represent the variation of the bubbles' radius and growth rate.

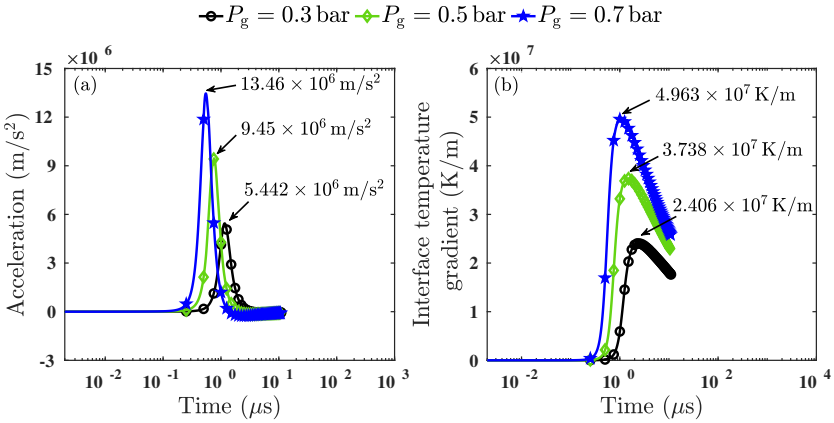

Figure 2.12: Variation of (a) the interface acceleration and (b) the temperature gradient for $T_g = 323$ K, $\Delta\theta = 27$ K with varying system pressures of $P_g = 0.3$ bar, $P_g = 0.5$ bar, and $P_g = 0.7$ bar.

increase in maximum hydrodynamic pressure is relatively small because of the moderate change in the thermal feedback. For the same reason, the time at which these maxima are reached does not change much. Indeed, the time at which the highest pressure values are reached varies from 1.139 μs to 2.754 μs. Increased thermal feedback with the increasing system pressure is responsible for this phenomenon in the same way as described in Section 2.4.2. Interestingly, the time interval over which the pressure difference is being balanced by the hydrodynamic pressure, $\Delta P = P_v - P_g \approx P_{hd}$, increases with the increasing system pressure. The lower growth rate in the inertia-controlled growth phase for case 'MS-HP', as depicted in Fig. 2.11b, can be attributed to this phenomenon. Thus, it can be concluded that increasing the system pressure pushes the dynamics towards inertia-controlled growth.

2.4.4 Influence of Chain Length

In this section, a comparison of bubble growth within single droplets at P_g= 0.3 bar and $\Delta\theta = 40$ K, is conducted for fuels with a different number of oxymethylene groups ($-CH_2O-$): OME_1, OME_4, having one and four groups respectively, and DME, which has none. The dynamics of the bubble growth change drastically, as the number of $-CH_2O-$ groups is increased.

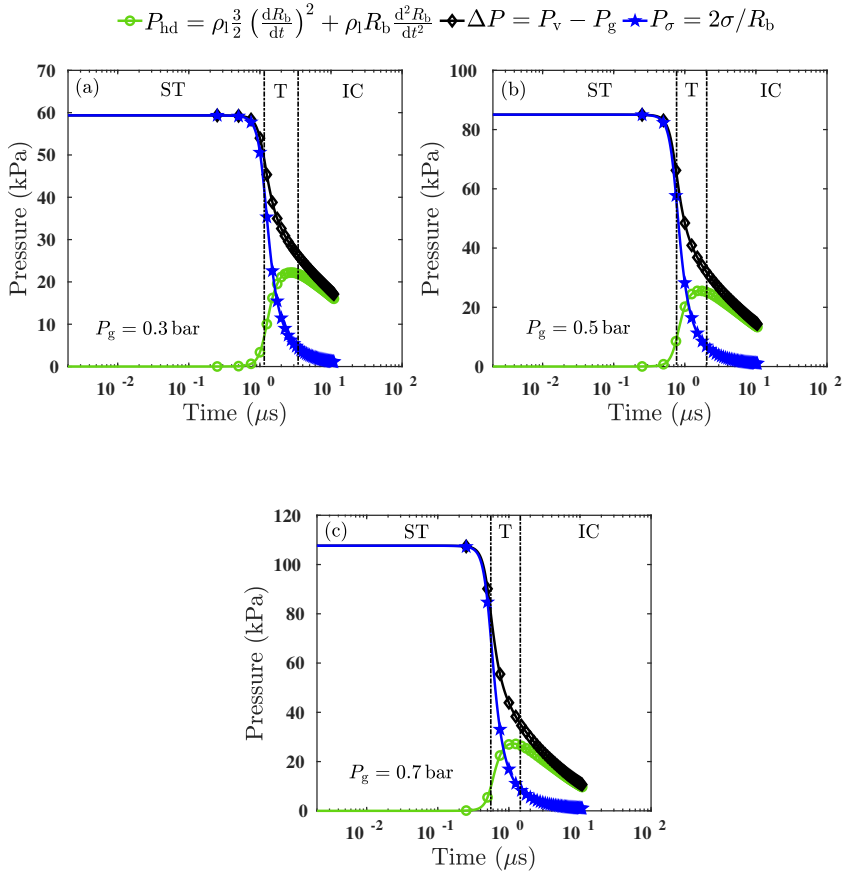

Figure 2.13: The dependency of the rate of change of ΔP on the hydrodynamic pressure at $T_g = 323\,\mathrm{K}$ and $\Delta\theta = 27\,\mathrm{K}$ with different system pressures (a) P_g= 0.3 bar, (b) P_g= 0.5 bar, and (c) P_g= 0.7 bar.

DME is found to have the smallest critical nuclei and the lowest delay time compared to OME_1 and OME_4, as shown in Fig. 2.14a. The higher vapor pressure of DME is responsible for the smallest critical radius (Eq. (2.3)). As described in Section 2.4.2, the smaller the critical radius is, the more intense is the thermal feedback effect (seen from the higher interface temperature gradient in Fig. 2.14d). Thus, the growth rate will increase, as illustrated in Fig. 2.14b. Fig. 2.14c depicts the interface acceleration, which also increases from $1.538 \times 10^7\,\mathrm{m/s^2}$ to $5.392 \times 10^7\,\mathrm{m/s^2}$ with the decreasing number of

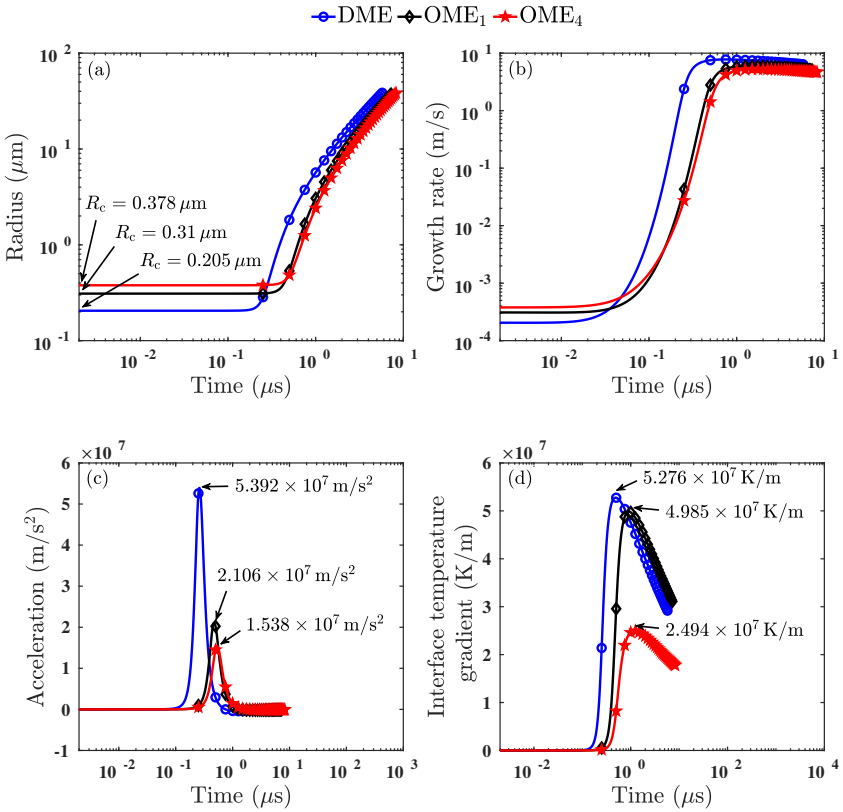

Figure 2.14: Influence of the number of $-CH_2O-$ groups on the bubble growth characteristics for $P_g = 0.3\,\text{bar}$, $T_g = 323\,\text{K}$ and $\Delta\theta = 40\,\text{K}$. Subfigures (a), (b), (c), and (d) represent the variation of the bubbles' radius, growth rate, interface acceleration, and temperature gradient, respectively over time.

$-CH_2O-$ groups, because this leads to an increase in the rate at which $(\partial T/\partial r)_{R_b}$ increases over time.

Fig. 2.15a illustrates that DME has the highest P_{hd} value, while in Fig. 2.15c, OME_4 shows a value which is in comparison less than about 43% that of DME. The higher bubble growth rate of DME has a positive influence on

creating a significant liquid motion in the surrounding within a relatively short period of time. The adverse impact of the higher hydrodynamic pressure on the thermal feedback phenomenon is thus higher in the case of DME, as can be seen from the highest change in slope of ΔP during the transition growth phase in Fig. 2.15a.

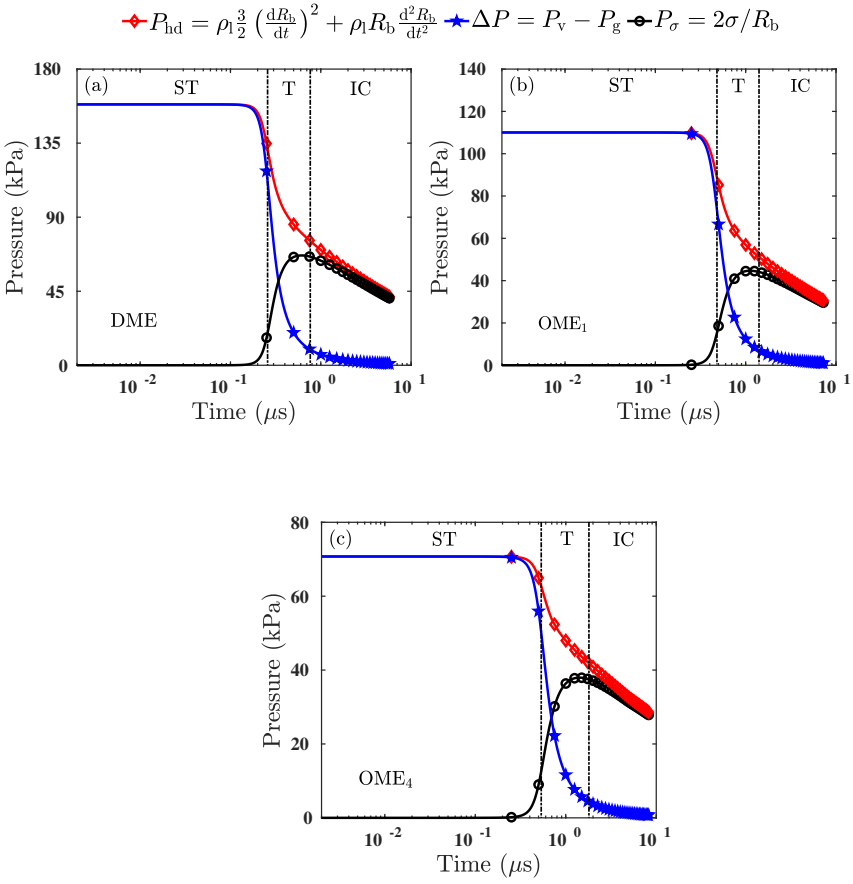

Figure 2.15: The dependency of the rate of change of ΔP on the hydrodynamic pressure for varying number of $-CH_2O-$ groups at $P_g = 0.3\,\text{bar}$, $T_g = 323\,K$, and $\Delta\theta = 40\,\text{K}$. Subfigures (a), (b) and (c) represent the pressure curves for DME, OME_1, and OME_4, respectively.

2.4.5 Effect of System Properties on the Onset of Droplet Bursting

The onset of droplet bursting, t_b, for OME_1 at different system superheating degrees is shown in Fig. 2.16. As the superheating degree is increased, t_b is markedly reduced. At $P_g = 0.3$ bar and $\Delta\theta = 6\,K$, the droplet bursting occurs at 98.55 μs, whereas for $\Delta\theta = 35\,K$, it takes only 8.519 μs. A faster growth rate and a higher bubble number density are likely responsible for decreasing the droplet bursting time. Fig. 2.16a depicts the variation of t_b with the increasing system pressures for moderate to high superheating degrees. It can be observed that the increase in system pressure initially reduces t_b, and then a further increase in the pressure increases t_b again. The gradual rise in the rate of decreasing interface temperature gradient with increasing system pressure in the inertia-controlled phase is responsible for this behavior. This is illustrated in Fig. 2.12b. Conversely, Fig. 2.16b shows a strong increase

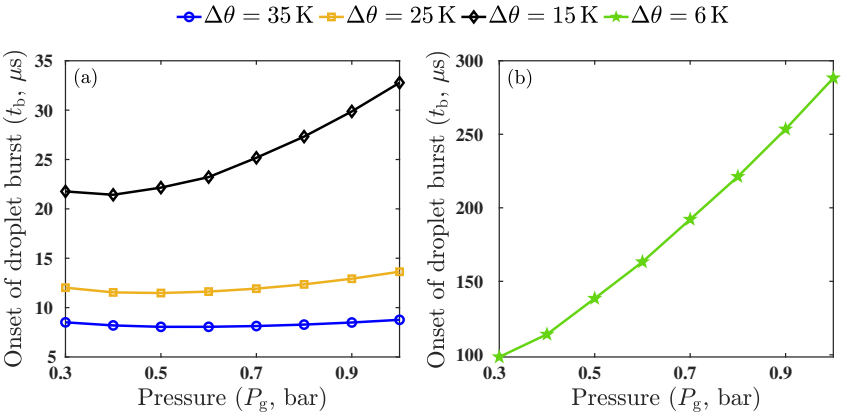

Figure 2.16: The influence of system pressure on the onset of OME_1 droplet bursting for varying superheating degrees of (a) $\Delta\theta = 35\,K$, $\Delta\theta = 25\,K$, $\Delta\theta = 15\,K$, and (b) $\Delta\theta = 6\,K$.

in t_b with the increasing system pressure at a very low superheating degree. This behavior is somehow unexpected but explainable considering Eq. (2.15). For the low superheat case, the difference in the heat flux at the interface, $\lambda_l \left(\partial T/\partial r\right)_{R_b}$, is small, as shown in Fig. 2.17a. Thus, the change of the inverse of the sensible heat term, $1/\left(\rho_v L_v\right)$, which decreases significantly with increasing system pressure, becomes the dominating factor determining the bubble growth in the later period of the bubbles' lifetime. This phenomenon

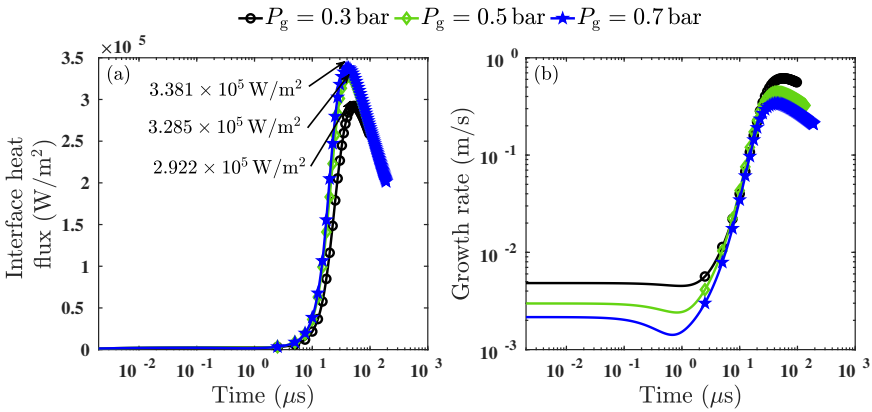

Figure 2.17: Variation of (a) the interface heat flux and (b) the bubble growth rate for $T_g = 323$ K, $\Delta\theta = 6$ K with varying system pressure of $P_g = 0.3$ bar, $P_g = 0.5$ bar, and $P_g = 0.7$ bar for the OME_1 droplet.

eventually causes the bubbles to expand at a much lower rate compared to the low pressure cases, as shown in Fig. 2.17b, and consequently delays the droplet burst.

Fig. 2.18 illustrates the effect of chain length on the onset of droplet bursting for a superheating degree of $\Delta\theta = 25$ K with the system pressures ranging from P_g= 0.3 bar to P_g= 1 bar. It is observed that the droplet bursting occurs relatively quickly in the case of DME, while for OME_1 and OME_4, it takes longer time to initiate the process. The faster occurrence of droplet burst is due to the higher bubble growth rate of DME. It is interesting to note that the OME_1 droplet bursts earlier compared with the OME_4 droplet in the case of low pressure. This gradually changes with the increasing system pressure; at P_g= 1 bar, the initiation of the droplet bursting process takes a longer time for OME_1 compared with OME_4. The lower bubble growth rate in the inertial-controlled phase, due to the relatively higher rate of decrease in the interface temperature gradient, is responsible for delaying the droplet bursting process of OME_1.

Fig. 2.19 illustrates the influence of initial perturbation on bubble growth rate for an OME_1 droplet with varying superheating degrees. In general, the vapor bubbles with larger initial radius due to large perturbation grow faster than the smaller ones in the very beginning of their evolution. Because of this, t_b decreases with increasing perturbation, as can be seen from Fig. 2.19.

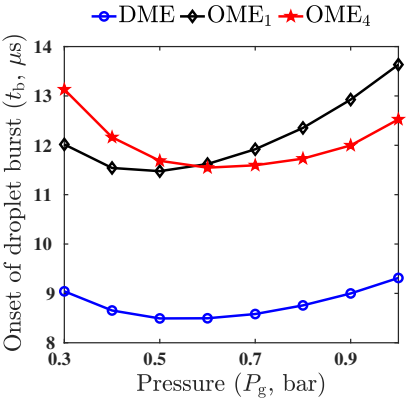

Figure 2.18: Influence of the number of $-CH_2O-$ groups on the onset of droplet bursting for $\Delta\theta = 25\,\mathrm{K}$ at system pressures ranging from $P_\mathrm{g} = 0.3\,\mathrm{bar}$ to $P_\mathrm{g} = 1\,\mathrm{bar}$.

Still the effect of initial perturbation on the initiation of droplet bursting becomes smaller with increasing superheating degree. Fig. 2.19a shows that for $\Delta\theta = 47$ K, t_b is decreased by 4.4 % with increasing ΔR_b, while for $\Delta\theta = 10$ K, t_b is reduced by 25.8 %, as can be seen from Fig. 2.19c. The higher value of t_d and slower growth rate associated with decreasing ΔR for lower superheating degree is eventually the reason behind this phenomenon. It is also important to note that the bubble growth rate converges quickly towards an asymptotic value for higher superheating degree, whereas for lower superheating degree, the droplet bursts before it reaches the asymptotic limit. Nevertheless, qualitatively the arbitrarily applied initial perturbation may not have major impact on the bubble dynamics.

2.4.6 Role of Bubble Dynamics on the Overall Droplet Vaporization

The bubble and droplet dynamics are linked together primarily via the expansion of the liquid due to the presence of multiple bubbles. The droplet bulk temperature is a secondary factor in combining these two dynamics, although it has an influence in the prediction of the bubbles' surface temperature, as shown in Eq. (2.6). We consider the droplet bulk temperature as a secondary factor because the change in T_d is found to be negligibly small during the droplet lifetime due to much shorter timescales associated with flash-boiling.

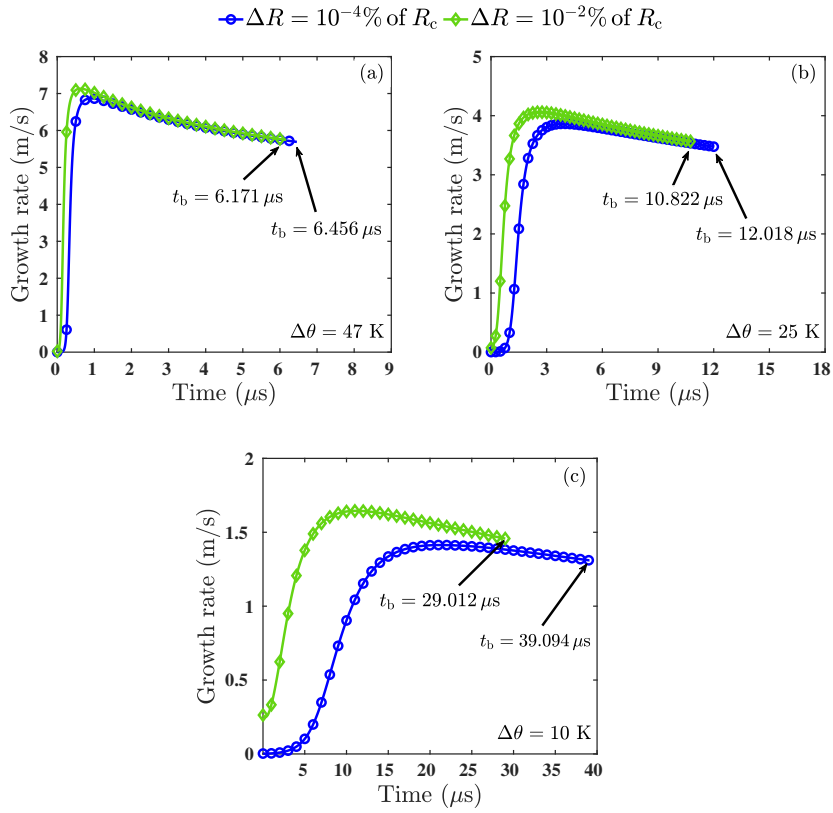

Figure 2.19: The influence of initial perturbation on bubble growth rate for OME_1 droplet at $T_g = 323\,K$, $P_g = 0.3\,bar$ with varying superheating degrees of (a) $\Delta\theta = 47\,K$, (b) $\Delta\theta = 25\,K$, and (c) $\Delta\theta = 10\,K$.

A quantitative comparison between the internal and the external vaporization is discussed in this section. It can be seen from Fig. 2.20a and Fig. 2.20c that the amount of liquid undergoing phase transition from the external surface of the droplet is higher only at the very beginning of the droplet lifetime. Since the vapor bubbles are just nucleated and are still small in size, the internally vaporized mass is small compared to that vaporized externally. As the vapor bubbles continuously grow in size, the internal vaporization increases, and then starts dominating over the external vaporization. The

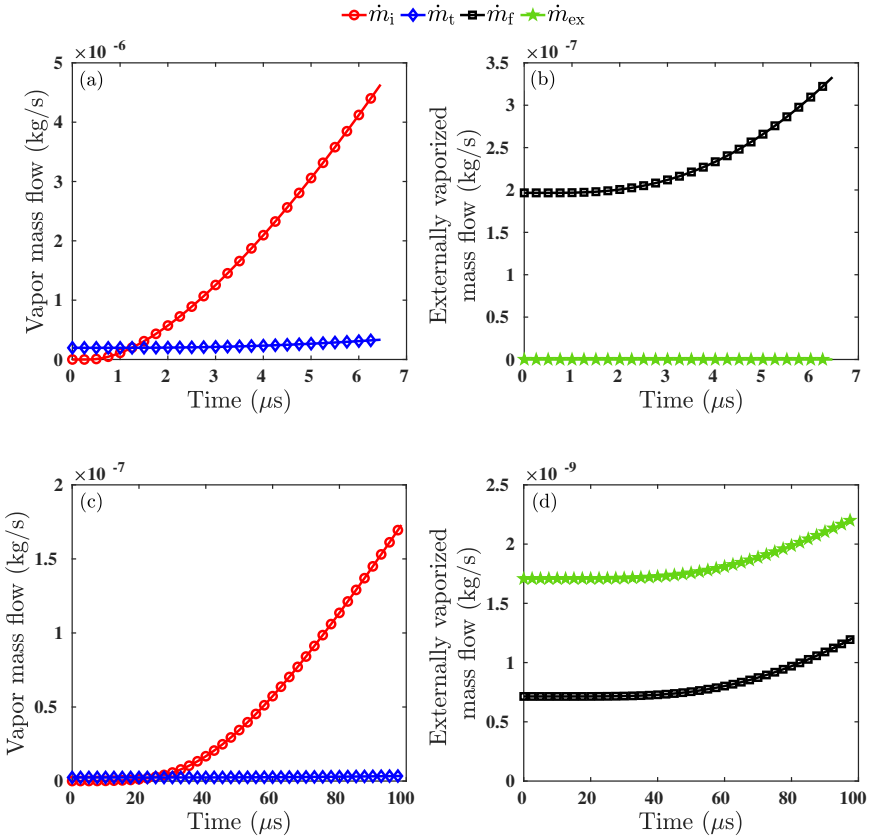

Figure 2.20: OME_1 fuel vapor mass flow rate over time at $P_g = 0.3$ bar and $T_g = 323$ K with varying superheating degrees of $\Delta\theta = 47$ K ((a) and (b)) and $\Delta\theta = 6$ K ((c) and (d)). Subfigures (a) and (c) represent the internally ($\dot{m}_i$) as well as the externally vaporized fuel mass flow ($\dot{m}_t$). Subfigures (b) and (d) illustrate the relative contribution of the flash boiled fuel vapor mass at the outer interface of the droplet ($\dot{m}_f$) and the external heat transfer driven fuel vapor mass ($\dot{m}_{ex}$) in overall droplet vaporization.

growing bubbles gradually push the surrounding liquid in outward direction, causing the droplet expansion over time, as shown in Fig. 2.21. This trend is opposite relative to the subcooled vaporization, where the liquid droplet surface regresses over time, as the external vaporization is the only source of phase change.

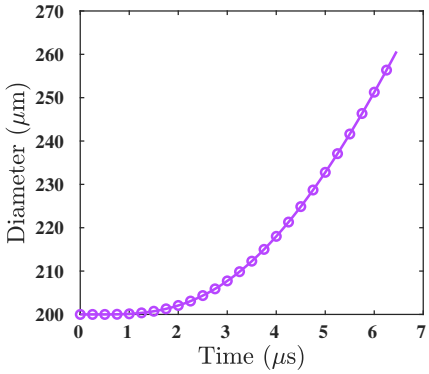

Figure 2.21: Superheated OME_1 droplet diameter evolution over time for $P_g = 0.3\,\text{bar}$, $T_g = 323\,\text{K}$, $\Delta\theta = 47\,\text{K}$.

Fig. 2.20b and Fig. 2.20d illustrate the relative contribution of the flash boiled vapor mass and the external heat transfer driven vapor mass in the total mass leaving from the droplet. It is worth noting that the contribution of the mass flow from the droplet surface due to the external heat transfer is very small for $\Delta\theta = 47\,\text{K}$. It remains nearly of the order of $O(\dot{m}_{ex}) \approx 10^{-13}$ kg/s for the majority of the droplet lifetime, as displayed in Fig. 2.20b. Thus, in the case of the high superheating degree, it can be concluded that $\dot{m}_i$ and $\dot{m}_f$ are the two main ways in which the transition of the metastable liquid phase into the stable one occurs. However, this is not the case for $\Delta\theta = 6\,\text{K}$. Here, the external heat transfer driven vapor mass flow ($O(\dot{m}_{ex}) \approx 10^{-9}$ kg/s) is one order of magnitude larger than the flash boiled vapor mass flow ($O(\dot{m}_f) \approx 10^{-10}$ kg/s), as depicted in Fig. 2.20d. Hence, for the low superheating degree, $\dot{m}_{ex}$ also plays an important role along with $\dot{m}_i$ and $\dot{m}_f$ during the transition towards a stable system.

2.5 Conclusions

In this study, the flash-boiling of the OME_x single droplets was investigated at low ambient pressures for different superheating degrees. The OME_1 bubble growth characteristics were described in a detailed manner. The effects of superheating degree and system pressure on the bubble growth dynamics of OME_1 was shown. The study revealed three distinct growth phases of the vapor bubbles in the OME_1 single droplet for moderate and high superheat cases under the assumption that the mono-disperse bubbles remain separate and distant from each other throughout their lifetime: (1) surface tension-controlled phase, (2) transition phase, and (3) inertia-controlled phase. Thermal diffusion does not appear to play a role in controlling the bubble growth under these operating conditions, which has not been reported earlier but shall be subject to further investigations using resolved simulations of bubbles in a single droplet configuration. Differently, in the case of a low superheat level, mainly two growth phases are observed: (1) surface tension-controlled phase and (2) transition phase. Due to the negligibly small liquid inertial forces, the transition phase for the low superheat system is primarily controlled by surface tension and thermal diffusion. For high and moderate superheat level, the increasing system pressure is found to decrease the onset of droplet bursting initially, and then increases again with further increase in pressure; whereas for a low superheating degree, increasing system pressure markedly postpones the time when the droplet bursts. Similarly, increasing superheating degree at a constant pressure leads to a drastic reduction in the bursting time. Moreover, the increasing system pressure is found to push the bubble dynamics more towards inertia-controlled growth.

The dependency of the growth characteristics on the chain length was also studied. It is found that decreasing the number of $-CH_2O-$ groups in the OME-fuel significantly increases the bubble growth rate because of the stronger thermal feedback from the surrounding superheated liquid. OME_x with increasing chain length is found to have a higher hydrodynamic pressure. Additionally, the DME droplet is found to burst faster compared with the other molecules. Bubble radius evolutions of OME_x fuels are also shown in non-dimensional form, which demonstrates that a generalized curve can be used to predict the characteristics of bubble growth for OME_x with lower number of $-CH_2O-$ groups such as $x = 0$ and 1. As the number of $-CH_2O-$ groups is increased to four, the non-dimensional growth characteristics of the vapor bubbles show a strong deviation, thus illustrating the requirement of further investigation of the non-dimensional parameters.

The effect of system properties on the onset of droplet bursting was explored. It is found that increasing superheating degree noticeably reduces the onset of droplet bursting. For high superheating degree, the system pressure is found to have a negligible impact on the initiation of droplet bursting, whereas for low superheat level, the increasing system pressure leads to a significant delay in initiating the droplet bursting. The effect of the varying initial perturbation on bubble growth rate was studied for different superheating degrees. A small initial perturbation leads to a longer time delay and slower growth rate compared with a high perturbation. This, in turn, delays the onset of droplet bursting. However, with increasing superheat level, the influence of initial perturbation on the onset of droplet bursting becomes smaller.

Furthermore, the influence of bubble growth dynamics on the overall droplet vaporization was discussed. It is concluded that the amount of liquid vaporized due to the bubbles formation inside the droplet is noticeably larger than the one from the external surface. The droplet diameter increases over time as the internal vaporization causes the droplet to expand. An outward force resulting from the continuous expansion of the vapor bubbles is found to be responsible for this phenomenon.

It is to be noted that the aim of this chapter is to provide a qualitative guidance on the physics associated with the single droplet flash-boiling phenomena of OME_x fuels for varying operating conditions. Since the actual perturbation required for initiating the bubble growth is not known a priori, the quantitative values related to the dynamics of the bubbles reported in this chapter will differ according to the arbitrarily applied initial perturbation.

3 Bubble Growth Modeling with Bubble Interactions

Reduced-order modeling on flash-boiling of single droplets considering the effects of the finite droplet-size and bubble-bubble interactions are still scarce in the literature. Although recent study by Dietzel et al. [60] investigated the bubble evolution using DNS, it is not feasible for large-scale spray simulations. Along these lines, the objectives of this chapter can be summarized as follows: (1) to propose a modified RPE for characterizing the growth of vapor bubbles in superheated microdroplets considering bubble-bubble interactions; (2) to validate the derived ROM for bubble growth using DNS results by Dietzel et al. [60]; and (3) to analyze the effect of bubble-bubble interactions on the growth characteristics of the vapor bubbles in superheated microdroplets. It has to be noted that the present chapter does not include the vaporization from the droplet's external surface, as it has been shown in the previous chapter to have a negligible contribution compared to internal vaporization.

The manuscript is organized as follows: in Section 3.1, we present the bubble growth models for superheated microdroplets with and without considering bubble-bubble interactions. The details of the computational setup and the solution procedure are shown in Section 3.2. The performance of the proposed bubble growth model is compared with that of the DNS results [60] in Section 3.3. Section 3.4 outlines the results from the numerical simulations. Finally, the findings are summarized in Section 5.7.

3.1 Theoretical Formulations

The conventional RPE [89] is often used to describe the temporal dynamics of a single vapor bubble in a superheated liquid medium. However, the conventional RPE needs to be modified for the flash-boiling microdroplets containing multiple bubbles, where the interaction among bubbles significantly alters the bubble dynamics [60]. In this study, we first derive the modified RPE considering the bubble-bubble interactions along with the finite-size effects of the flash-boiling microdroplets.

In this section, first, we discuss the governing equations of the single isolated vapor bubble growth in an infinite liquid medium and in a finite-size

superheated microdroplet. Then, we describe the equations governing the vapor bubble growth in superheated microdroplets considering the bubble-bubble interactions.

3.1.1 Single Isolated Vapor Bubble Growth

The growth rate of an isolated spherically symmetric vapor bubble in a homogeneous infinite liquid medium can be estimated using the conventional RPE as [89]

$$\underbrace{P_{\mathrm{v}}\left(T_{\mathrm{v}}\right)-P_{\mathrm{l}}}_{\Delta P}=\underbrace{\rho_{\mathrm{l}} R_{\mathrm{b}} \frac{\mathrm{d}^2 R_{\mathrm{b}}}{\mathrm{d}t^2}}_{P_{\mathrm{hd,acc}}}+\underbrace{\frac{3}{2}\rho_{\mathrm{l}}\left(\frac{\mathrm{d}R_{\mathrm{b}}}{\mathrm{d}t}\right)^2}_{P_{\mathrm{hd,vel,b}}}+\underbrace{\frac{4\mu_{\mathrm{l}}}{R_{\mathrm{b}}}\frac{\mathrm{d}R_{\mathrm{b}}}{\mathrm{d}t}}_{P_{\mu}}+\underbrace{\frac{2\sigma}{R_{\mathrm{b}}}}_{P_{\sigma}}, \tag{3.1}$$

where P_{μ} is the pressure due to liquid viscosity at the liquid-vapor interface. $P_{\mathrm{hd,acc}}$ and $P_{\mathrm{hd,vel,b}}$ are the hydrodynamic pressures induced by the surrounding liquid due to the bubble surface acceleration and velocity, respectively. In this study, we denote the total hydrodynamic pressure for the bubble growth without bubble-bubble interactions as $P_{\mathrm{hd}}=P_{\mathrm{hd,acc}}+P_{\mathrm{hd,vel,b}}$.

For a finite-size single droplet in a quiescent gaseous medium, the conventional RPE can be modified as

$$P_{\mathrm{v}}\left(T_{\mathrm{v}}\right)-P_{\mathrm{l}}=\rho_{\mathrm{l}}\left[R_{\mathrm{b}}\left(1-\frac{R_{\mathrm{b}}}{R_{\mathrm{d}}}\right)\frac{\mathrm{d}^2 R_{\mathrm{b}}}{\mathrm{d}t^2}+\left(\frac{3}{2}-\frac{2R_{\mathrm{b}}}{R_{\mathrm{d}}}+\frac{R_{\mathrm{b}}^4}{2R_{\mathrm{d}}^4}\right)\left(\frac{\mathrm{d}R_{\mathrm{b}}}{\mathrm{d}t}\right)^2\right]+\frac{4\mu_l}{R_{\mathrm{b}}}\frac{\mathrm{d}R_{\mathrm{b}}}{\mathrm{d}t}+\frac{2\sigma}{R_{\mathrm{b}}}, \tag{3.2}$$

where $R_{\mathrm{d}}(t)$ denotes the instantaneous droplet radius. In comparison with the conventional RPE shown in Eq. (3.1), Eq. (3.2) includes additional inertia terms on the right-hand side given by $-\rho_{\mathrm{l}}\left(R_{\mathrm{b}}^2/R_{\mathrm{d}}\right)\left(\mathrm{d}^2R_{\mathrm{b}}/\mathrm{d}t^2\right)$ and $\rho_{\mathrm{l}}\left\{-2R_{\mathrm{b}}/R_{\mathrm{d}}+R_{\mathrm{b}}^4/\left(2R_{\mathrm{d}}^4\right)\right\}\left(\mathrm{d}R_{\mathrm{b}}/\mathrm{d}t\right)^2$. P_{l} in Eq. (3.2) is given by the mechanical balance between the liquid and the surrounding gas phase as

$$P_{\mathrm{l}}=P_{\mathrm{g}}+\frac{2\sigma}{R_{\mathrm{d}}}, \tag{3.3}$$

where P_g is the surrounding gas pressure. Substituting P_l into Eq. (3.2) yields

$$\underbrace{P_\mathrm{v}\left(T_\mathrm{v}\right) - P_\mathrm{g}}_{\Delta P} = \underbrace{\rho_\mathrm{l} R_\mathrm{b}\left(1 - \frac{R_\mathrm{b}}{R_\mathrm{d}}\right)\frac{\mathrm{d}^2 R_\mathrm{b}}{\mathrm{d}t^2}}_{P_\mathrm{hd,acc}} + \underbrace{\rho_\mathrm{l}\left(\frac{3}{2} - \frac{2R_\mathrm{b}}{R_\mathrm{d}} + \frac{R_\mathrm{b}^4}{2R_\mathrm{d}^4}\right)\left(\frac{\mathrm{d}R_\mathrm{b}}{\mathrm{d}t}\right)^2}_{P_\mathrm{hd,vel,b}} + \underbrace{\frac{4\mu_l}{R_\mathrm{b}}\frac{\mathrm{d}R_\mathrm{b}}{\mathrm{d}t}}_{P_\mu} + \underbrace{2\sigma\left(\frac{1}{R_\mathrm{b}} + \frac{1}{R_\mathrm{d}}\right)}_{P_\sigma}. \tag{3.4}$$

It is to be noted that the Eq. (3.4) is valid only for a single isolated vapor bubble inside a superheated single droplet.

3.1.2 Vapor Bubble Growth in Multibubble Environment

In reality, there are multiple bubbles inside the droplet. Thus, the bubble growth rate is also influenced by the interaction between the individual bubbles. Considering the bubble-bubble interactions, the RPE in Eq. (3.4) is modified as

$$\begin{aligned} P_\mathrm{v}\left(T_\mathrm{v}\right) - P_\mathrm{g} = \rho_\mathrm{l}\Bigg[\frac{\mathrm{d}}{\mathrm{d}t}\left(\sum \frac{R_\mathrm{b}^2}{r_i}\frac{\mathrm{d}R_\mathrm{b}}{\mathrm{d}t}\right) + R_\mathrm{b}\left(1 - \frac{R_\mathrm{b}}{R_\mathrm{d}}\right)\frac{\mathrm{d}^2 R_\mathrm{b}}{\mathrm{d}t^2} \\ + \left(\frac{3}{2} - \frac{2R_\mathrm{b}}{R_\mathrm{d}} + \frac{R_\mathrm{b}^4}{2R_\mathrm{d}^4}\right)\left(\frac{\mathrm{d}R_\mathrm{b}}{\mathrm{d}t}\right)^2\Bigg] + \frac{4\mu_\mathrm{l}}{R_\mathrm{b}}\frac{\mathrm{d}R_\mathrm{b}}{\mathrm{d}t} + 2\sigma\left(\frac{1}{R_\mathrm{b}} + \frac{1}{R_\mathrm{d}}\right), \end{aligned} \tag{3.5}$$

where the first term on the right-hand side of Eq. (3.5) represents the pressure, P_inter, acting on the target bubble surface induced by all the other bubbles [67]. The distance r_i is measured from the center of the i-th bubble to the center of the target bubble. The bubbles are assumed to be mono-disperse in this study. For simplicity, it is also assumed that the bubbles remain sufficiently far away from each other such that the interactions among the boundary layers across the bubble surface can be neglected and the relative position of the bubbles remain unchanged during the vaporization process. A schematic model of the bubble-bubble interactions is shown in Fig. 3.1. The detailed derivation of

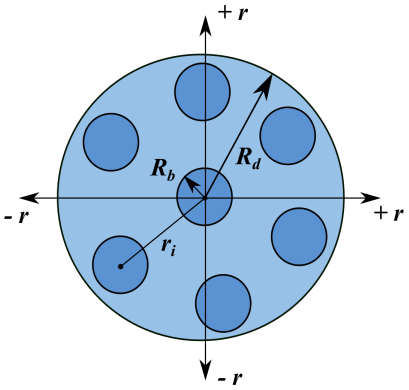

Figure 3.1: Schematic of the reduced-order modeling of bubble-bubble interactions in superheated microdroplets.

P_{inter} is given in Appendix C. P_{inter} can be rearranged as follows [98]

$$\frac{\mathrm{d}}{\mathrm{d}t}\left[\sum \frac{R_{\mathrm{b}}^2}{r_i}\frac{\mathrm{d}R_{\mathrm{b}}}{\mathrm{d}t}\right] = \frac{\mathrm{d}}{\mathrm{d}t}\left[R_{\mathrm{b}}^2\frac{\mathrm{d}R_{\mathrm{b}}}{\mathrm{d}t}\sum \frac{1}{r_i}\right] = \frac{\mathrm{d}}{\mathrm{d}t}\left[R_{\mathrm{b}}^2\frac{\mathrm{d}R_{\mathrm{b}}}{\mathrm{d}t}\int_0^{R_{\mathrm{d}}}\frac{1}{r}(n\ \mathrm{d}v)\right], \tag{3.6}$$

where n denotes the number density of the vapor bubbles and $n\ \mathrm{d}v$ the total number of bubbles in an infinitesimal volume of the droplet, $\mathrm{d}v$. Assuming heterogeneous nucleation due to air as dissolved gas, the number density of the vapor bubble nuclei can be estimated using the approximation suggested by Senda et al. [19] as described in Chapter 2.

The integration over the sphere of influence (R_{d}) in Eq. (3.6) yields

$$\begin{aligned}\frac{\mathrm{d}}{\mathrm{d}t}\left[R_{\mathrm{b}}^2\frac{\mathrm{d}R_{\mathrm{b}}}{\mathrm{d}t}\int_0^{R_{\mathrm{d}}}\frac{1}{r}(n\ \mathrm{d}v)\right] &= \frac{\mathrm{d}}{\mathrm{d}t}\left[R_{\mathrm{b}}^2 n\frac{\mathrm{d}R_{\mathrm{b}}}{\mathrm{d}t}\int_0^{R_{\mathrm{d}}}\frac{1}{r}4\pi r^2\ \mathrm{d}r\right] \\ &= \frac{\mathrm{d}}{\mathrm{d}t}\left[2\pi R_{\mathrm{b}}^2 n\frac{\mathrm{d}R_{\mathrm{b}}}{\mathrm{d}t}R_{\mathrm{d}}^2\right] \\ &= 2\pi n R_{\mathrm{d}}^2 R_{\mathrm{b}}\left\{R_{\mathrm{b}}\frac{\mathrm{d}^2R_{\mathrm{b}}}{\mathrm{d}t^2} + 2\left(\frac{\mathrm{d}R_{\mathrm{b}}}{\mathrm{d}t}\right)^2\right\} \\ &\quad + 4\pi n R_{\mathrm{b}}^2 R_{\mathrm{d}}\left(\frac{\mathrm{d}R_{\mathrm{b}}}{\mathrm{d}t}\right)\left(\frac{\mathrm{d}R_{\mathrm{d}}}{\mathrm{d}t}\right)\end{aligned} \tag{3.7}$$

where n is assumed to be constant during the flash vaporization process. It is essential to acknowledge that in practical scenarios, the number density will vary as the droplet expands. Hence, it is imperative to conduct further research on the proposed model, incorporating experimental measurements of superheated single droplets. This will enable a comprehensive exploration of the implications of our assumption regarding constant number density. Substituting Eq. (3.7) into Eq. (3.5) and rearranging the terms, the modified RPE for spherically symmetric vapor bubbles in a single droplet of radius R_d considering the bubble-bubble interactions is written as

$$\begin{aligned}\underbrace{P_\mathrm{v}\left(T_\mathrm{v}\right)-P_\mathrm{g}}_{\Delta P'} = \underbrace{\rho_\mathrm{l}R_\mathrm{b}\left(1-\frac{R_\mathrm{b}}{R_\mathrm{d}}+2\pi R_\mathrm{d}^2 n R_\mathrm{b}\right)\frac{\mathrm{d}^2R_\mathrm{b}}{\mathrm{d}t^2}}_{P'_\mathrm{hd,acc}} \\ +\underbrace{\rho_\mathrm{l}\left(\frac{3}{2}-\frac{2R_\mathrm{b}}{R_\mathrm{d}}+\frac{R_\mathrm{b}^4}{2R_\mathrm{d}^4}+4\pi R_\mathrm{d}^2 n R_\mathrm{b}\right)\left(\frac{\mathrm{d}R_\mathrm{b}}{\mathrm{d}t}\right)^2}_{P'_\mathrm{hd,vel,b}}+\underbrace{\frac{4\mu_\mathrm{l}}{R_\mathrm{b}}\frac{\mathrm{d}R_\mathrm{b}}{\mathrm{d}t}}_{P'_\mu} \\ +\underbrace{4\pi n\rho_\mathrm{l}R_\mathrm{d}R_\mathrm{b}^2\left(\frac{\mathrm{d}R_\mathrm{d}}{\mathrm{d}t}\right)\left(\frac{\mathrm{d}R_\mathrm{b}}{\mathrm{d}t}\right)}_{P'_\mathrm{hd,vel,db}}+\underbrace{2\sigma\left(\frac{1}{R_\mathrm{b}}+\frac{1}{R_\mathrm{d}}\right)}_{P'_\sigma},\end{aligned} \tag{3.8}$$

where the superscript ' $\prime$ ' denotes the modified pressures acting on the bubble surface for the bubble growth considering the bubble-bubble interactions. The new pressure term, $P'_\mathrm{hd,vel,db}$, is the contribution to the total hydrodynamic pressure (P'_hd) due to the expansion velocities of both the bubble and the droplet. P'_hd is thus expressed as $P'_\mathrm{hd} = P'_\mathrm{hd,acc} + P'_\mathrm{hd,vel,b} + P'_\mathrm{hd,vel,db}$.

In this study, the droplet is considered much larger than the vapor bubbles ($R_\mathrm{d} \gg R_\mathrm{b}$). Thus, the second term of $P'_\mathrm{hd,acc}$ can be neglected, since the order of magnitude of the bubble to droplet radius ratio, $R_\mathrm{b}/R_\mathrm{d}$, remains very small compared to the first and third terms. Similarly, the contribution from the second and third terms of $P'_\mathrm{hd,vel,b}$ also becomes negligible with respect to the first and fourth terms and hence can be neglected. The second term of P'_σ can also be neglected, since $1/R_\mathrm{b} \gg 1/R_\mathrm{d}$. The resulting simplified RPE

after neglecting the above-mentioned terms is given as

$$\underbrace{P_{\mathrm{v}}\left(T_{\mathrm{v}}\right)-P_{\mathrm{g}}}_{\Delta P'}=\underbrace{\rho_{l}R_{\mathrm{b}}\left(1+2\pi R_{\mathrm{d}}^{2}nR_{\mathrm{b}}\right)\frac{\mathrm{d}^{2}R_{\mathrm{b}}}{\mathrm{d}t^{2}}}_{P'_{\mathrm{hd,acc}}}+\underbrace{\rho_{\mathrm{l}}\left(\frac{3}{2}+4\pi R_{\mathrm{d}}^{2}nR_{\mathrm{b}}\right)\left(\frac{\mathrm{d}R_{\mathrm{b}}}{\mathrm{d}t}\right)^{2}}_{P'_{\mathrm{hd,vel,b}}}+\underbrace{\frac{4\mu_{\mathrm{l}}}{R_{\mathrm{b}}}\frac{\mathrm{d}R_{\mathrm{b}}}{\mathrm{d}t}}_{P'_{\mu}}+\underbrace{4\pi n\rho_{\mathrm{l}}R_{\mathrm{d}}R_{\mathrm{b}}^{2}\left(\frac{\mathrm{d}R_{\mathrm{d}}}{\mathrm{d}t}\right)\left(\frac{\mathrm{d}R_{\mathrm{b}}}{\mathrm{d}t}\right)}_{P'_{\mathrm{hd,vel,db}}}+\underbrace{\frac{2\sigma}{R_{\mathrm{b}}}}_{P'_{\sigma}}. \tag{3.9}$$

The saturated vapor temperature, T_{v}, is obtained by solving the implicit relation given by Eq. (2.6). The energy flux at the liquid-vapor interface causes the liquid to vaporize and creates a pressure difference, which is then balanced in the RPE by the hydrodynamic terms (IC growth stage), the surface tension term (ST growth stage), or both (T stage).

The droplet is considered to burst once the void fraction exceeds its critical limit ($\varepsilon \geq \varepsilon_{\mathrm{crit}}$). The critical void fraction value of 0.55 is chosen here for all simulated test cases [58].

3.2 Numerical Methodology

A square box of size 0.54 m × 0.54 m × 0.54 m with no-slip walls is chosen as the simulation domain. A superheated single droplet with a diameter of 200 µm is placed at the center of the domain. Although a spherical droplet is introduced into a three-dimensional computational domain, the complete problem is reduced to the solution of an ordinary differential equation in zero dimension by assuming the spherical symmetry of the droplet and considering the surrounding flow field as frozen. The droplet is considered to be stationary. Inert gas nitrogen is used as an ambient medium and the chemistry in the gas phase is neglected. The temperature and pressure inside the liquid droplet are assumed to be homogeneous. It is to be noted that the size of the square box and the subsequent spatial discretization were chosen such that they have no influence on the bubble dynamics presented in this study due to the assumptions of the frozen surrounding flow field.
The RPEs are advanced using a fixed time-step second-order Runge-Kutta (RK) scheme. Eq. (3.9) is solved for the case with bubble-bubble interactions. Whereas for the case without bubble-bubble interactions, Eq. (3.1) is solved assuming mono-disperse vapor bubbles of the number density of n in an

infinitely large single droplet ($R_d \gg R_b$). The bubble growth is initiated by perturbing the bubble critical radius, R_c, by 10^{-4}%. The temperature inside the vapor bubble, T_v, is obtained by iteratively solving Eq. (2.6) using the Newton-Raphson method.

3.3 Model Validation

Ideally, the proposed ROM needs to be validated at a microscopic level in two steps. First, the validation with experimental measurements of single isolated vapor bubbles is required to ensure that the model is able to accurately capture the single bubble growth in a superheated liquid medium. In the second step, the validation must be performed using flash-boiling single droplet experimental measurements in the presence of multiple bubbles. The present model has already been validated in Chapter 2 at the single isolated bubble level, and a further comparison with the single isolated bubble simulation by Dietzel et al. [60] will be shown in the following. Additionally, the performance of the proposed reduced-order bubble growth model with bubble-bubble interactions is compared against the DNS of multiple bubbles with variable expansion rate performed by Dietzel et al. [60] in terms of the volumetric expansion of a superheated LOx fuel droplet. A single droplet including 221 vapor bubbles was simulated for this purpose. The initial perturbation in R_c was chosen based on their single isolated bubble reference solution. The volume of the droplet was considered to be equivalent to that of the cylindrical liquid jet of Dietzel et al. [60]. Fig. 3.2 depicts the comparison of the nondimensional volumetric expansion of the LOx droplet for the isolated bubble and the bubble-bubble interaction case with the DNS results. For the single isolated bubble simulations, both the DNS and the ROM predict a similar volumetric expansion of around 75 %, as can be seen from Fig. 3.2. It is observed that the present ROM predicts a volumetric droplet expansion of around 7.5 % for the case with bubble-bubble interactions, whereas the multibubble DNS with variable expansion rate results in approximately a 5 % increase in the volume of the liquid jet. This demonstrates the strong impact of bubble interactions in the present case. The simulation is continued only up to $t = 0.45\,\mu s$, as this marks the minimum time required to the onset of bubble merging for the Dietzel et al. [60] case. The resulting overprediction from the ROM in the volumetric expansion for the bubble-bubble interactions case is reasonably small compared with the total effect of bubble interactions and can be attributed to the assumptions considered in its derivation such as spherically symmetric mono-disperse vapor bubbles and homogeneous

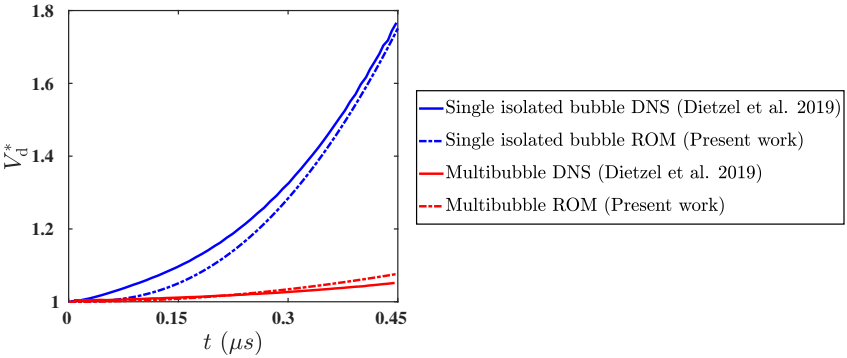

Figure 3.2: Comparison of the dimensionless volume of a LOx fuel droplet predicted by the proposed ROM with the DNS results reported by Dietzel et al. [60] for the bubble growth with (referred to as 'multibubble') and without (referred to as 'single isolated bubble') the bubble-bubble interactions at $P_g = 2.045$ bar and $T_d = 120$ K. The initial volume of the liquid droplet is used as a reference scale to nondimensionalize the instantaneous droplet volume, $V_{droplet}$.

pressure and temperature distribution in the liquid droplet. Overall, it can be concluded that the proposed ROM is capable of predicting the considerably smaller volume expansion in presence of the bubble-bubble interactions with reasonable accuracy.

At a macroscopic scale, the present bubble growth model could be validated by applying it to the primary breakup simulation of the flash-boiling spray case and comparing the droplet size distributions in the near-nozzle regime obtained from the simulations with the experiments. This validation at a macroscopic level is beyond the scope of the present dissertation and will be left for future work.

3.4 Results and Discussion

In this section, considering high volatility e-fuels, such as short-chain oxymethylene ethers (OME_x) as a generic example the influence of the bubble-bubble interactions on the dynamics of the vapor bubble growth in superheated microdroplets is described.

3.4.1 Influence of Bubble-bubble Interactions on the Bubble Dynamics

The comparison between the bubble growth characteristics of OME_1 microdroplets with and without bubble-bubble interactions is shown in Fig. 3.3 in terms of nondimensional variables for $P_g = 0.3$ bar, $T_d = 434.72$ K, and $\Delta\theta = 150$ K. The reference length (R_{ref}) and time (t_{ref}) scales used to nondimensionalize R_b and t are defined as $R_{ref} = R_c$ and $t_{ref} = R_c/A$, respectively, where $A = \sqrt{(2/3)(P_v - P_l)/\rho_l}$. The initial vapor temperature is used as a reference temperature scale to nondimensionalize the vapor temperature T_v. It can be seen that the bubble growth characteristics are significantly influenced by the bubble-bubble interactions once the bubbles surpass the T stage and enter into the IC growth stage. Fig. 3.3 depicts that the bubble-bubble interactions cause much slower expansion of the bubbles. This is because the additional pressure force induced by the surrounding growing bubbles on the target bubble surface markedly reduces its growth rate in the IC growth stage, as illustrated in Fig. 3.4. It is also observed from Fig. 3.4 that the rate at which the vapor temperature decreases considering the bubble-bubble interactions decreases substantially in this growth stage and subsequently reduces the positive thermal feedback at the bubble surface, which is proportional to $\Delta T^+ = T_d^+ - T_v^+$. The higher hydrodynamic pressure emerging from the bubble-bubble interactions in the IC growth stage is eventually the reason behind this phenomenon, which is depicted in Fig. 3.5.

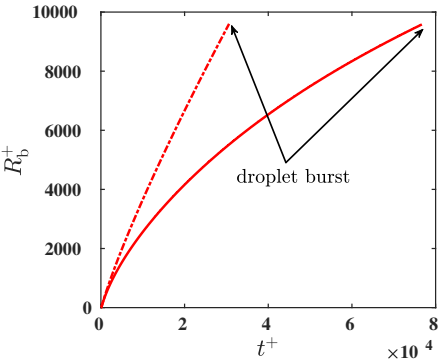

Figure 3.3: Comparison of the nondimensional bubble radius evolution over time with (solid line) and without (dash-dotted line) bubble-bubble interactions for OME_1 microdroplet at $\Delta\theta = 150$ K.

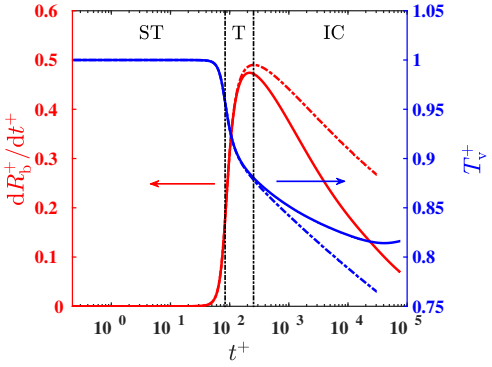

Figure 3.4: Comparison of the variation of the nondimensional bubble growth rate and vapor temperature with (solid line) and without (dash-dotted line) bubble-bubble interactions for OME_1 microdroplet at $\Delta\theta = 150$ K.

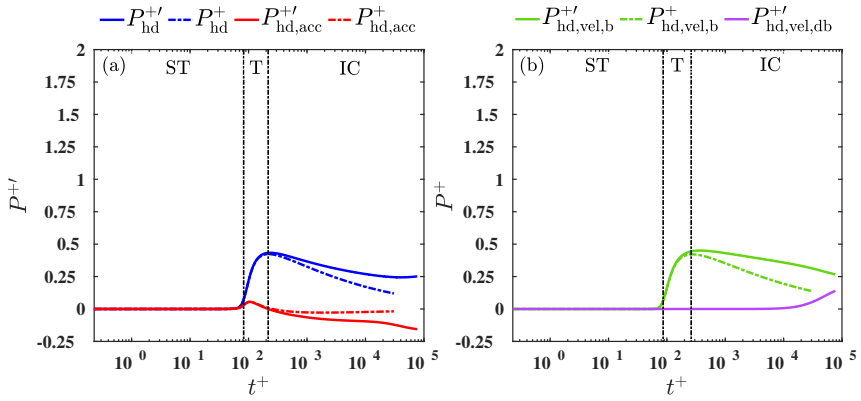

Figure 3.5: Comparison of the nondimensional pressure terms for the bubble growth with (solid line) and without (dash-dotted line) the bubble-bubble interactions for OME_1 microdroplet at $P_g = 0.3$ bar, $T_d = 434.72$ K, and $\Delta\theta = 150$ K. The presseure terms are nondimensionalized using the reference scale of $\rho_l A^2$.

From Fig. 3.4, it is interesting to note that the vapor temperature curve for the bubble growth with bubble-bubble interactions shows a gradual rise near the onset of droplet bursting. This phenomenon can be explained as follows: the mass within the bubbles increases in time as the surrounding superheated liquid becomes vapor due to the continuous energy flux at the bubble surface. The increasing mass causes a build-up of vapor pressure inside the bubbles. The bubbles then grow in size such that this excess of pressure can be relaxed. Since the vapor inside the bubbles is assumed to be saturated, a reduction in P_{v} also lowers the vapor temperature T_{v}. However, for the bubble growth considering the bubble-bubble interactions, a gradual rise in $P_{\mathrm{hd}}^{+\prime}$ near the onset of the droplet bursting suppresses the bubble growth, and subsequently the bubble surface acceleration (as shown in Fig. 3.5a) to such an extent that the vapor pressure continues to build up due to the slower growth of the vapor bubbles, and thus leading to an increase in vapor temperature near the onset of droplet bursting, as shown in Fig. 3.4. The faster droplet expansion in this regime eventually increases $P_{\mathrm{hd,vel,db}}^{+\prime}$ (as can be seen from Fig. 3.5b) in the later period of IC growth, which in turn, causes the total hydrodynamic pressure, $P_{\mathrm{hd}}^{+\prime}$ to increase (note that the slope of $P_{\mathrm{hd}}^{\prime}$ curve changes from negative to positive in the IC growth stage). Whereas for the bubble growth without the bubble-bubble interactions, P_{hd}^{+} continues to decrease in the IC growth stage due to the absence of the additional pressure force term, $P_{\mathrm{hd,vel,db}}^{+\prime}$. Thus, the vapor temperature also shows a continuous decline in time, as shown by the blue dash-dotted line in Fig. 3.3b. Due to the slower growth of the vapor bubbles, the onset of droplet bursting is also considerably delayed for the bubble growth with bubble-bubble interactions. The variation of the nondimensional pressure terms due to the viscous and surface tension forces is not shown as the bubble-bubble interactions are found to have negligible influence on these forces.

The dimensionless volume of the OME_1 fuel droplet is shown in Fig. 3.6 for the bubble growth with and without bubble-bubble interactions up to 2.67 µs, which marks the onset of droplet bursting for the later case. It is observed that the volumetric expansion of the liquid droplet is significantly smaller in presence of bubble-bubble interactions. It can be seen that the droplet volume has increased by only 23% after 2.67 µs when considering bubble-bubble interactions. Conversely, the case without bubble-bubble interactions leads to an increase in droplet volume by approximately 120% within the same time interval.

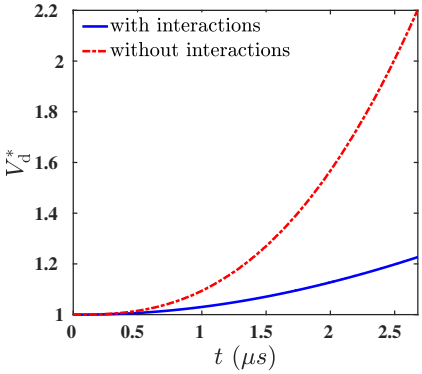

Figure 3.6: Variation of the dimensionless volume of the OME_1 fuel droplet for the bubble growth with (solid line) and without (dash-dotted line) the bubble-bubble interactions at $P_g = 0.3$ bar, $T_d = 434.72$ K, and $\Delta\theta = 150$ K. The initial volume of the liquid droplet is used as a reference scale to nondimensionalize the instantaneous droplet volume, V_{drop}.

3.4.2 Limitations of the Proposed ROM

Several assumptions were made in the derivation of the modified RPE (Eq. (3.9)), such as constant bubble number density, mono-disperse and spherically symmetric vapor bubbles, and sufficiently large inter-bubble spacing, which may not always hold true in comparison to the practical scenario. It has to be noted that while the assumptions are being made, the proposed model is closer to reality than completely neglecting the interactions. A more advanced subgrid-scale model for bubble growth may be derived by relaxing these assumptions. For example, polydisperse vapor bubbles arranged randomly in a superheated microdroplet could be considered. However, such an advanced modeling approach requires solving the RPE for each of the vapor bubbles present in the superheated droplet. This is also likely to increase the computational cost for large-scale sprays due to the presence of millions of microdroplets with multiple polydisperse vapor bubbles. Although it is necessary to study the dynamics of the droplet-bubble system with the above-mentioned advanced modeling strategy, the actual need for such models in predicting global spray characteristics should be determined based on the comparative analysis of cost-accuracy trade-off for different subgrid-scale bubble growth

models with varying degrees of simplification.

3.5 Conclusions

A new ROM for vapor bubble growth considering the bubble-bubble interactions in superheated microdroplets was proposed in this chapter. The model performance was compared with the DNS performed by Dietzel et al. [60]. It was observed that the proposed bubble growth model reasonably capture the impact of bubble interactions leading to smaller volumetric droplet expansion in comparison with the DNS results [60]. The bubble dynamics of OME_1 in the presence of bubble-bubble interactions was investigated. It was found that the bubble-bubble interactions significantly influence the bubble growth characteristics once the bubble surpasses the transition growth stage. The additional inertial force, P_{inter}, emerging from the bubble-bubble interactions was found to markedly reduce the bubble growth rate, and thus, significantly delay the onset of droplet bursting.

4 Semi-analytical Solution of RPE

4.1 Introduction

The time-step size is an important factor in the simulation of the flash-boiling phenomena of high-volatility liquid fuels. In Chapter 2, a fixed time-step size of one nanosecond $\left(\mathcal{O}\left(10^{-9}\,\mathrm{s}\right)\right)$ was used to simulate the flash vaporization phenomena of highly volatile e-fuel microdroplets. Yet, it was found in Chapter 3 that this time-step size is still insufficiently small when considering bubble-bubble interactions for high-volatility fuels. Thus, the computational cost will also increase for the simulation of the large-scale spray case consisting of millions of single droplets.

A universal correlation or a simplified analytical solution for the bubble growth rate throughout the whole bubble lifetime, which also considers all the complex physical processes including bubble-bubble interactions occurring during the flash vaporization of a superheated single droplet, would be useful for the accurate and computationally efficient simulation of the large-scale spray case.

Previous studies were mainly focused on the derivation of the analytical formulation and correlation for the single vapor-bubble growth in an infinite superheated liquid medium only at later growth stages, such as IC and TD growth [46, 48, 50–53, 99]. Rayleigh [46] proposed an analytical solution for bubble growth by neglecting the viscous effect and the cooling effect of vaporization as

$$\frac{\mathrm{d}R_\mathrm{b}}{\mathrm{d}t} = \left(\frac{2}{3}\frac{P_\mathrm{v} - P_\mathrm{l}}{\rho_\mathrm{l}}\right)^{\frac{1}{2}}, \tag{4.1}$$

where ρ_l and P_v are the saturated liquid density and vapor pressure, respectively, at bulk liquid temperature T_l. Eq. (4.1) is referred to as inertia-controlled growth and provides a good description of bubble dynamics for sufficiently large initial superheating degrees or sufficiently low system pressures. Plesset and Zwick [48] later obtained an asymptotic solution of bubble growth controlled by the thermal diffusion effect as

$$\frac{\mathrm{d}R_\mathrm{b}}{\mathrm{d}t} = \frac{1}{2}\left(\frac{12\alpha_\mathrm{l}}{\pi t}\right)^{\frac{1}{2}} \frac{\rho_\mathrm{l} C_\mathrm{l}\left(T_\mathrm{l} - T_\mathrm{sat}\left(P_\mathrm{l}\right)\right)}{L_\mathrm{v}\rho_\mathrm{v}}, \tag{4.2}$$

L_v and ρ_v denote the latent heat and saturated vapor density at saturation temperature, T_sat, respectively. The time t in Eq. (4.2) is measured from the onset of nucleation of the bubble. The range of applicability of the analytical works described above is limited to the later stages of bubble growth when the radius is much larger than the critical radius.

In order to correlate the bubble radius as a function of time in terms of nondimensional parameters, Lien [53] derived the reference length and time scales by requiring the nondimensionalization to be reasonable for both Eq. (4.1) and Eq. (4.2), which leads to

$$R_\mathrm{ref} = \frac{B^2}{A}, \quad t_\mathrm{ref} = \frac{B^2}{A^2}, \tag{4.3}$$

with

$$A = \left(\frac{2}{3}\frac{P_\mathrm{v} - P_\mathrm{l}}{\rho_\mathrm{l}}\right)^{\frac{1}{2}}, \quad B = Ja\left(\frac{12}{\pi}\alpha_\mathrm{l}\right)^{\frac{1}{2}}, \tag{4.4}$$

where Ja is the Jakob number defined as

$$Ja = \frac{\rho_\mathrm{l} c_\mathrm{l}\left(T_\mathrm{l} - T_\mathrm{sat}\left(P_\mathrm{l}\right)\right)}{\rho_\mathrm{v} L_\mathrm{v}}. \tag{4.5}$$

The nondimensional radius and time are then expressed as

$$R_\mathrm{b}^* = \frac{R_\mathrm{b}}{R_\mathrm{ref}} \quad \text{and} \quad t^* = \frac{t}{t_\mathrm{ref}}. \tag{4.6}$$

Mikic et al. [52] reported an analytical formulation for bubble growth rate by combining Eq. (4.1) and Eq. (4.2) in terms of nondimensional parameters proposed by Lien [53] as

$$\frac{\mathrm{d}R_\mathrm{b}^*}{\mathrm{d}t^*} = \sqrt{t^* + 1} - \sqrt{t^*}. \tag{4.7}$$

The scaling proposed by Lien [53] works well only in the later period of the bubble lifetime when the growth is mainly controlled by inertia or thermal diffusion effect. Prosperetti and Plesset [99] later attempted to derive an approximate law of bubble growth based on the theory provided by Plesset and Zwick [48] for the bubbles that have grown sufficiently large beyond their critical radius, at least by about an order of magnitude. They proposed the scaling relations

$$\tilde{R_\mathrm{b}} = \frac{C^2 R_\mathrm{b}}{R_\mathrm{c}}, \quad \tilde{t} = DC^2 t, \tag{4.8}$$

and

$$C = \left(\frac{2\sigma\left(T_\mathrm{l}\right)\alpha_\mathrm{l}}{9\pi}\right)^{\frac{1}{2}} \frac{\rho_\mathrm{v} L_\mathrm{v}}{\lambda_\mathrm{l}} \frac{\left\{\rho_\mathrm{l}\left[P_\mathrm{v} - P_\mathrm{l}\right]\right\}^{-\frac{1}{2}}}{\left(T_\mathrm{l} - T_\mathrm{sat}\left(P_\mathrm{l}\right)\right)}, \tag{4.9}$$

$$D = \frac{\left[P_\mathrm{v} - P_\mathrm{l}\right]^{\frac{3}{2}}}{2\sigma\left(T_\mathrm{l}\right)\rho_\mathrm{l}^{\frac{1}{2}}}, \tag{4.10}$$

where '~' implies nondimensional quantities. The physical parameters of Eq. (4.9) and Eq. (4.10) are evaluated at $T_\mathrm{sat}\left(P_\mathrm{l}\right)$, except σ. In addition, they defined a more general scaling law, which was expected to work also in the surface tension-dominated growth phase,

$$\hat{R_\mathrm{b}} = \frac{R_\mathrm{b}}{R_\mathrm{c}}, \quad \hat{t} = Dt, \tag{4.11}$$

where '^' denotes nondimensional quantities. In addition, they also defined a more general scaling law, which was expected to work also in the surface tension-dominated growth phase. However, the detailed analysis of this scaling law was not reported as they found it to be of less practical interest compared to that shown in Eq. (4.8).

The surface tension-controlled growth may become relevant to automotive or cryogenic engine applications, such as injecting superheated liquid fuel into a combustion chamber. Here, the lifetime of the vapor bubbles becomes much shorter as the liquid jet undergoes bursting phenomena once the critical void fraction is reached [19]. In Chapter 2, it is observed that for moderate to high superheating degrees, the onset of droplet burst times, t_b, for highly volatile e-fuel microdroplets are in the order of $\mathcal{O}(t_\mathrm{b}) \approx 10^{-6} - 10^{-7}$ s. For the lower superheating degree case, the order of magnitude increases to $\mathcal{O}(t_\mathrm{b}) \approx 10^{-4}$ s. Due to the shorter droplet lifetime, the initial surface tension-controlled growth phase of the vapor bubbles becomes equally important to the inertia, transition, and thermal diffusion-controlled growth phases. This is because the shorter the ST growth stage is, the earlier the significant bubble growth starts and vice-versa, thus influencing the bubble-growth characteristics in the later bubble growth stages as well. However, the influence of the ST growth stage on the bubble dynamics becomes negligible when the bubble grows for a long period [47].

Recently, Saha et al. [100] derived two different analytical solutions for the vapor bubble growth rate in superheated single droplets for high and low bubble Reynolds numbers ($\mathrm{Re_b}$) using a similar general scaling law to that

proposed by Prosperetti and Plesset [99] as

$$\left.\frac{\mathrm{d}R_\mathrm{b}^+}{\mathrm{d}t^+}\right|_{\mathrm{High\,Re_b}} = \sqrt{\frac{2}{3}\left(P_\mathrm{v}^+ - P_\mathrm{g}^+\right)\left\{1-\left(\frac{1}{R_\mathrm{b}^+}\right)^3\right\} - \frac{2}{R_\mathrm{b}^+\mathrm{We_b}}\left\{1-\left(\frac{1}{R_\mathrm{b}^+}\right)^2\right\}}, \tag{4.12}$$

and

$$\left.\frac{\mathrm{d}R_\mathrm{b}^+}{\mathrm{d}t^+}\right|_{\mathrm{Low\,Re_b}} = -\frac{4}{3R_\mathrm{b}^+\mathrm{Re_b}} + \sqrt{\left(\frac{4}{3R_\mathrm{b}^+\mathrm{Re_b}}\right)^2 - \left\{\frac{4}{3R_\mathrm{b}^+\mathrm{We_b}} - \frac{2}{3}\left(P_\mathrm{v}^+ - P_\mathrm{g}^+\right)\right\}} \tag{4.13}$$

with

$$\begin{aligned} R_\mathrm{b}^+ &= \frac{R_\mathrm{b}}{R_\mathrm{c}}, \quad t^+ = \frac{tA}{R_\mathrm{c}}, \quad P_\mathrm{v}^+ = \frac{P_\mathrm{v}}{\rho_{l0}A^2}, \quad P_\mathrm{g}^+ = \frac{P_\mathrm{g}}{\rho_{l0}A^2}; \\ \mathrm{Re_b} &= \frac{\rho_{l0}AR_\mathrm{c}}{\mu_{l0}}, \quad \mathrm{We_b} = \frac{\rho_{l0}A^2R_\mathrm{c}}{\sigma_0} = \frac{4}{3}, \end{aligned} \tag{4.14}$$

where $\mathrm{We_b}$ the bubble Weber number. The superscript '+' and subscript '0' denote the nondimensional quantities and the initial values, respectively. However, the bubble-bubble interactions were neglected in that study.

Along these lines, the objectives of this chapter can be summarized as follows: (1) to highlight the limitations of the numerical solver for simulating the bubble growth with the newly derived RPE in a flash-boiling single droplet of highly volatile liquid fuels; (2) to explore a scaling law for evaluating its capability of describing the different bubble growth stages including ST, T, IC, and TD growth for a flash-boiling single droplet; and (3) to derive a semi-analytical solution in terms of nondimensional parameters for the bubble growth considering the bubble-bubble interactions to describe the bubble evolution with reasonable accuracy in different growth phases.

This chapter is organized as follows: in Section 4.2, the issues related to the use of large time-steps are illustrated for the simulation of highly volatile liquid fuels under various operating conditions considering the bubble-bubble interactions. The dimensional analysis of the modified RPE is described in Section 4.3. Finally, Section 4.5 summarizes the findings of this chapter.

4.2 Limitations of the Numerical Solver

Fig. 4.1 shows the variation of bubble growth rate for different time-step sizes for $\mathrm{OME_1}$ microdroplets under two different operating conditions considering

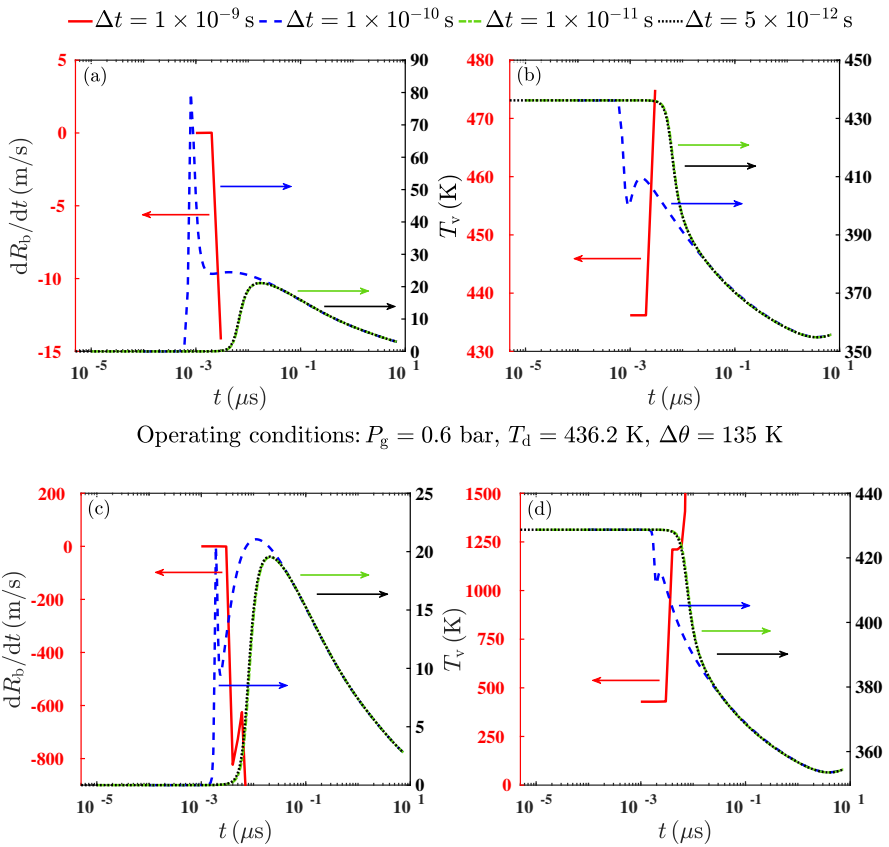

Figure 4.1: Bubble growth rate (left column) and vapor temperature (right column) variation for OME_1 microdroplets under various operating conditions and time-step sizes considering the bubble-bubble interactions.

the bubble-bubble interactions. For $\Delta\theta = 135$ K, it is observed that the time-step size of $\Delta t = 1 \times 10^{-9}$ s causes the growth rate to become negative in the very beginning (see Fig. 4.1a), which then causes an increasing vapor temperature, as shown in Fig. 4.1b. The simulation is not continued further since the Newton-Raphson iteration estimates an unrealistically negative vapor temperature with the negative bubble growth rate in the next time-step.

As the time-step size is decreased to $\Delta t = 1 \times 10^{-10}$ s, the bubble evolves well in the very beginning. However, it shows a sudden jump in growth rate at around 7 $\times 10^{-4}$ µs, followed by a sharp decline at 9 $\times 10^{-4}$ µs. A sudden drop in vapor temperature can also be seen from Fig. 4.1b due to a sudden rise in bubble growth rate. Nevertheless, the bubble growth rate increases further in time and subsequently results in decreasing T_{v}. This fluctuating growth behavior does not appear to be physical. The time-step sizes are then further reduced to $\Delta t = 1 \times 10^{-11}$ s and $\Delta t = 5 \times 10^{-12}$ s, which are found to eliminate the spurious fluctuations in the bubble growth rate curve, as obtained earlier with the larger time step sizes. All the physical phenomena associated with the bubble growth such as the surface-tension dominated extremely slow growth stage, followed by the rapid bubble surface acceleration and subsequent gradual deceleration are captured with the reduced Δt. Qualitatively, these results are in good agreement with previous publications [21, 45]. Fig. 4.1c & Fig. 4.1d depict the bubble growth rate and vapor temperature variation for $\Delta\theta = 120$ K. Similarly, $\Delta t = 1 \times 10^{-9}$ s and $\Delta t = 1 \times 10^{-10}$ s result in unrealistic growth rates and vapor temperatures, whereas $\Delta t = 1 \times 10^{-11}$ s and $\Delta t = 5 \times 10^{-12}$ s correctly predict the evolution of the bubble. The numerical issue with the time-step size is also demonstrated using another highly volatile cryogenic e-fuel microdroplets of DME and the results are included in Appendix D.

The numerical results described above are obtained using the explicit RK solver as mentioned in Section 3.2. An implicit ODE solver CVODE, which includes variable time-step, variable-order backward differentiation formulas, is also employed in this study to simulate the bubble growth characteristics. It is observed that the CVODE solver produces spurious fluctuations in the bubble growth rate curve near the beginning of the T growth stage. The simulation results obtained from the CVODE solver are shown here for $\Delta\theta = 90$ K with $\Delta t = 1 \times 10^{-9}$ s in Fig. 4.2a. As the time-step size is reduced to $\Delta t = 1 \times 10^{-10}$ s, the bubble growth rate is found to be well predicted by the CVODE solver similarly to the explicit RK solver, as shown in Fig. 4.2b. However, due to its implicit nature, the computational cost associated with the CVODE solver is higher compared to the explicit RK solver. For example, the simulated case with the CVODE solver is run on a machine using the Intel Broadwell processor architecture on a single core for 1.2585 CPUh, whereas the same case with the explicit RK solver is run on the same machine on a single core for 0.0186 CPUh.

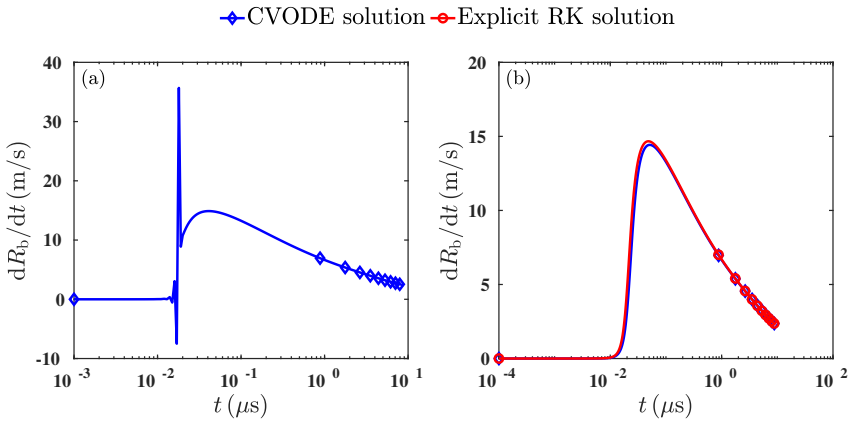

Figure 4.2: Bubble growth rate of OME_1 microdroplets obtained using different solvers for (a) $\Delta t = 1 \times 10^{-9}$ s and (b) $\Delta t = 1 \times 10^{-10}$ s considering the bubble-bubble interactions at $P_g = 1.0$ bar, $T_d = 404.86$ K, and $\Delta\theta = 90$ K.

4.3 Dimensional Analysis of RPE

In this section, first, we describe the nondimensional formulations of the modified RPE derived in Chapter 3. Next the applicability of different scaling laws in describing the bubble growth in a flash-boiling single droplet is highlighted under subatmospheric operating conditions. After that, dimensional analysis of the modified RPE (Eq. (4.16)) is performed to determine the magnitude of the different nondimensional force terms acting on the bubble surface for Reynolds numbers of different orders of magnitude. Based on the dimensional analysis, a semi-analytical solution for the bubble growth is then derived in terms of nondimensional parameters considering the bubble-bubble interactions to mitigate the numerical issues described in Section 4.2. Finally, the proposed semi-analytical solution is validated with the numerical solution of the modified RPE.

4.3.1 Nondimensionalization of RPE

The RPE is nondimensionalized using the critical bubble radius, R_c, as the length scale, A as the velocity scale (Eq. (4.4)), and the time scale, $t_\mathrm{ref} = R_\mathrm{c}/A$:

$$\begin{aligned} R_\mathrm{k}^+ &= \frac{R_\mathrm{k}}{R_\mathrm{c}}, \quad \dot{R}_\mathrm{k}^+ = \frac{\dot{R}_\mathrm{k}}{A}, \quad t^+ = \frac{t}{t_\mathrm{ref}}, \quad \mu_\mathrm{l}^+ = \frac{\mu_\mathrm{l}}{\mu_\mathrm{l0}}; \\ \rho_\mathrm{l}^+ &= \frac{\rho_\mathrm{l}}{\rho_\mathrm{l0}}, \quad P^+ = \frac{P}{\rho_\mathrm{l0} A^2}, \quad \sigma^+ = \frac{\sigma}{\sigma_0}, \quad n^+ = n R_\mathrm{c}^3, \end{aligned} \tag{4.15}$$

where the subscript 'k' can be replaced by subscripts 'd' and 'b' for droplet and bubble quantities, respectively. The superscript '+' denotes the nondimensional quantities and the subscript '0' represents the initial values.

The resulting nondimensional RPE for a spherically symmetric vapor bubble, considering the bubble-bubble interactions, in a finite-size single droplet of radius R_d is given as

$$\begin{aligned} \underbrace{P_\mathrm{v}^+ - P_\mathrm{g}^+}_{\Delta P^{+\prime}} &= \underbrace{\rho_\mathrm{l}^+ R_\mathrm{b}^+ \left(1 + 2\pi R_\mathrm{d}^{+2} n^+ R_\mathrm{b}^+\right) \frac{\mathrm{d}^2 R_\mathrm{b}^+}{\mathrm{d}t^{+2}}}_{P_\mathrm{hd,acc}^{+\prime}} \\ &+ \underbrace{\rho_\mathrm{l}^+ \left(\frac{3}{2} + 4\pi R_\mathrm{d}^{+2} n^+ R_\mathrm{b}^+\right) \left(\frac{\mathrm{d}R_\mathrm{b}^+}{\mathrm{d}t^+}\right)^2}_{P_\mathrm{hd,vel,b}^{+\prime}} + \underbrace{\frac{4}{R_\mathrm{b}^+} \frac{\mu_\mathrm{l}^+}{\mathrm{Re}_\mathrm{b}} \frac{\mathrm{d}R_\mathrm{b}^+}{\mathrm{d}t^+}}_{P_\mu^{+\prime}} \\ &+ \underbrace{4\pi n^+ \rho_\mathrm{l}^+ R_\mathrm{d}^+ R_\mathrm{b}^{+2} \left(\frac{\mathrm{d}R_\mathrm{d}^+}{\mathrm{d}t^+}\right) \left(\frac{\mathrm{d}R_\mathrm{b}^+}{\mathrm{d}t^+}\right)}_{P_\mathrm{hd,vel,db}^{+\prime}} + \underbrace{\frac{2\sigma^+}{\mathrm{We}_\mathrm{b}} \frac{1}{R_\mathrm{b}^+}}_{P_\sigma^{+\prime}}. \end{aligned} \tag{4.16}$$

Eq. (4.16) can be simplified for the bubble growth without bubble-bubble interactions as

$$\underbrace{P_\mathrm{v}^+ - P_\mathrm{g}^+}_{\Delta P^+} = \underbrace{\rho_\mathrm{l}^+ R_\mathrm{b}^+ \frac{\mathrm{d}^2 R_\mathrm{b}^+}{\mathrm{d}t^{+2}}}_{P_\mathrm{hd,acc}^+} + \underbrace{\rho_\mathrm{l}^+ \frac{3}{2} \left(\frac{\mathrm{d}R_\mathrm{b}^+}{\mathrm{d}t^+}\right)^2}_{P_\mathrm{hd,vel,b}^+} + \underbrace{\frac{4}{R_\mathrm{b}^+} \frac{\mu_\mathrm{l}^+}{\mathrm{Re}_\mathrm{b}} \frac{\mathrm{d}R_\mathrm{b}^+}{\mathrm{d}t^+}}_{P_\mu^+} + \underbrace{\frac{2\sigma^+}{\mathrm{We}_\mathrm{b}} \frac{1}{R_\mathrm{b}^+}}_{P_\sigma^+}. \tag{4.17}$$

The derivation of the nondimensional RPE with and without bubble-bubble interactions is given in Appendix E.

4.3.2 Scaling Law for Superheated Microdroplets

The scaling relationships of Lien [53] (Eq. (4.6)) work well only for the later bubble growth stages when the bubble surpasses the T stage and enters into the IC or TD growth stage [47]. This is expected because the effect of surface tension, which remains a dominating factor during the first two growth stages [45], is not considered in the Lien [53] formulation. The Prosperetti and Plesset [99] scaling law (Eq. (4.8)) also shows a behavior similar to the Lien [53] scaling law because it assumes a linear variation of saturated vapor pressure with temperature and constant physical properties in the formulations to describe the scaled bubble growth behavior.

In real engine conditions, liquid jets or droplets will not remain intact for a long period. They will rupture within a very short period (in the order of microseconds) due to the rapid growth of multiple vapor bubbles. Thus, the scaling laws, Eq. (4.6) and Eq. (4.8), which work well in later bubble growth stages when the bubbles are grown sufficiently large beyond their critical radius, will not be applicable for the realistic engine conditions. This is illustrated in Fig. 4.3, where the temporal variations of nondimensional bubble radii of OME_1 microdroplets are plotted using the Lien [53] scaling law considering the bubble-bubble interactions for various operating conditions, as listed in Table 4.1. Hence, the need arises for a more general scaling law, which reasonably models not only the later IC and TD growth stages but also the initial ST growth stage.

Fig. 4.4 shows the variation of dimensionless bubble radii plotted with Eq. (4.15) considering the bubble-bubble interactions for the similar pressure and temperature ranges, as shown in Table 4.1. It can be seen from Fig. 4.4 that all the dimensionless radius curves merge into a single curve of value unity in the regime of ST growth. In the later growth stages, however, the scaled radius-time curves do not perfectly collapse into a single curve. Thus, it is difficult to describe a reasonably accurate universal bubble growth behavior with a relation of the form

$$R_{\mathrm{b}}^{+} = f\left(t^{+}\right). \tag{4.18}$$

4.3.3 Derivation of Semi-analytical Solution

Fig. 4.5 illustrates the variation of $P^{+\prime}$ for three different Re with bubble-bubble interactions. The physical parameters and their values corresponding to the different Reynolds number cases are listed in Table 4.2. It is to be noted that the definition of the Re shown in Eq. (4.14) allows a maximum value of Re in the order of the magnitude of 2, which corresponds to a very

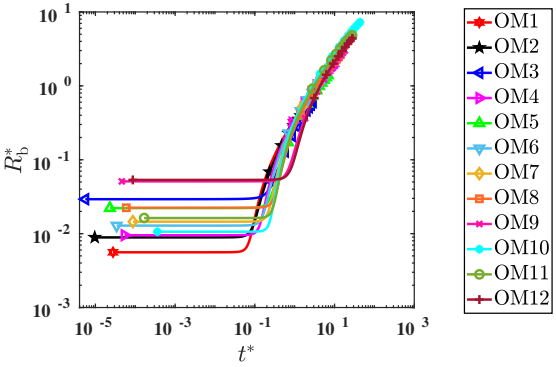

Figure 4.3: Nondimensional radius of the vapor bubbles in superheated OME_1 microdroplets scaled with Eq. (4.6) under subatmospheric pressure conditions, as listed in Table 4.1. The bubble radii are plotted in solid lines with various types of markers associated with different test cases considered for analyzing the behavior of the scaling laws.

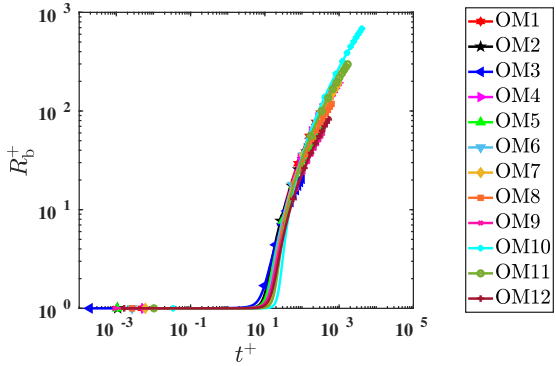

Figure 4.4: Nondimensional radius of the vapor bubbles in superheated OME_1 microdroplets scaled with Eq. (4.15) under subatmospheric pressure conditions, as listed in Table 4.1. The bubble radii are plotted in solid lines with various types of markers associated with different test cases considered for analyzing the behavior of the scaling laws.

Case $\downarrow$	P_l	T_d	$\Delta\theta$	R_c	A	B
Unit $\rightarrow$	bar	K	K	μm	m/s	m/$\sqrt{s}$
OM1	0.3	331.72	47	0.22	10.95	0.021
OM2	0.3	311.72	27	0.64	6.88	0.022
OM3	0.3	296.72	12	2.08	3.97	0.017
OM4	0.5	336.63	40	0.20	11.32	0.015
OM5	0.5	316.63	20	0.65	6.73	0.014
OM6	0.5	326.63	30	0.34	9.0	0.015
OM7	0.7	340.16	35	0.19	11.45	0.012
OM8	0.7	330.16	25	0.34	8.93	0.012
OM9	0.7	320.16	15	0.70	6.37	0.009
OM10	0.9	368.92	57	0.06	18.84	0.010
OM11	0.9	349.92	38	0.13	13.36	0.010
OM12	0.9	328.92	17	0.47	7.60	0.008

Table 4.1: Simulation test cases for OME_1 microdroplets.

Parameter	**Case #1 High $\mathrm{Re_b}$ (HRe)**	**Case #2 Moderate $\mathrm{Re_b}$ (MRe)**	**Case #3 Low $\mathrm{Re_b}$ (LRe)**
P_l (bar)	0.3	0.3	0.3
T_d (K)	290.72	355.72	434.72
$\Delta\theta$ (K)	6	71	150
R_c (μm)	4.83	0.0802	0.004
A (m/s)	2.64	16.62	44.49
$B\left(\mathrm{m/s^{\frac{1}{2}}}\right)$	0.011	0.017	0.008
$\mathrm{Re_b}$	31.35	5.06	0.85

Table 4.2: Simulation test cases of OME_1 microdroplets for validating the simplified semi-analytical solutions.

low superheating degree case ($\Delta\theta \approx \mathcal{O}(10^{-2}\,\mathrm{K})$). In this study, we have considered three different Re of 31.35, 5.06, and 0.85, termed as high Reynolds number ('HRe'), moderate Reynolds number ('MRe'), and low Reynolds number ('LRe'), respectively. It can be seen from Fig. 4.5a that for the case of 'HRe', the order of magnitude of $P_\mu^{+\prime}$ is negligible throughout the whole bubble lifetime compared to the other terms. However, with decreasing Re,

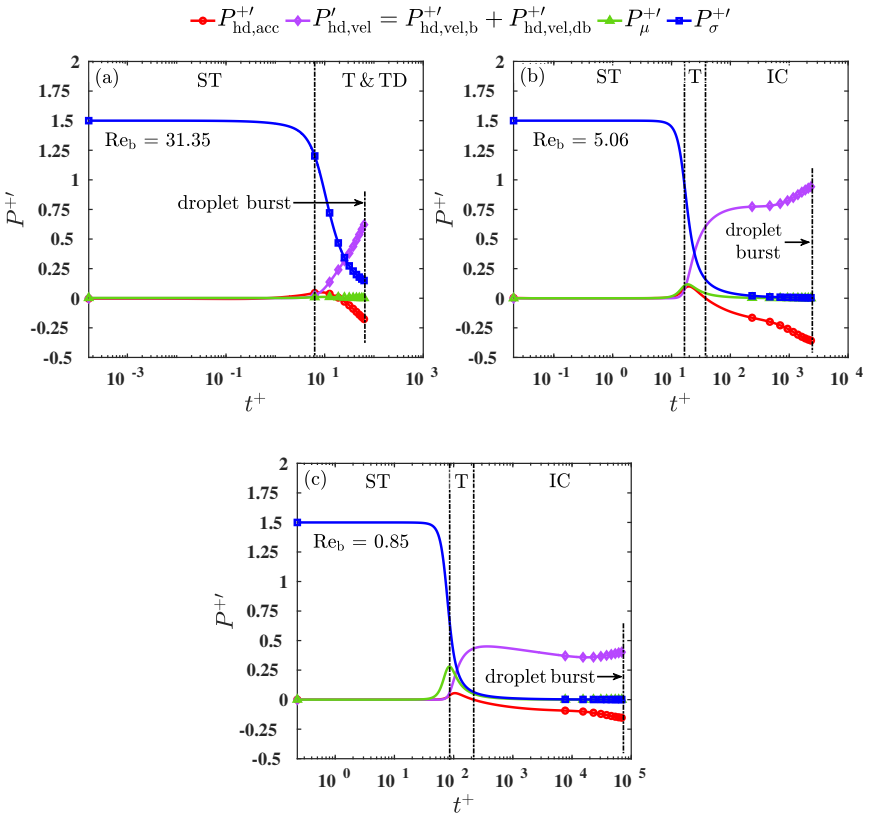

Figure 4.5: Comparison of the different nondimensional pressure terms of Eq. (4.16) as a function of nondimensional time for three different Reynolds numbers of (a) 31.35, (2) 5.06, and (c) 0.85, considering bubble-bubble interactions in $\mathrm{OME_1}$ microdroplets for operating conditions listed in Table 4.2. The pressure terms are plotted in solid lines with different types of markers in order to distinguish the contributions from the inertia, viscous, and surface tension forces

.

the influence of $P^{+\prime}_{\mu}$ becomes important already in the later period of the ST growth stage, as shown in Fig. 4.5c for 'LRe'. The order of magnitude of $P^{+\prime}_{\mathrm{hd,acc}}$ starts to become important towards the end of the ST growth stage

and becomes negative in the transition stage with gaining importance for later times. Nevertheless, as the $\mathrm{Re_b}$ is reduced, the rate of decrease in $P^{+\prime}_{\mathrm{hd,acc}}$ also decreases. Thus, it can be concluded that $P^{+\prime}_{\mathrm{hd,acc}}$ becomes less important in determining the bubble growth characteristics compared to $P^{+\prime}_{\mathrm{hd,vel}}$ as the $\mathrm{Re_b}$ is reduced from 31.35 to 0.85. Since $P^{+\prime}_{\mathrm{hd,acc}}$ has a tendency to become less significant with decreasing Re, we neglect this term in the following to derive an approximate semi-analytical solution of Eq. (4.16). The effect of neglecting $P^{+\prime}_{\mathrm{hd,acc}}$ on bubble growth behavior will be discussed later in detail. Neglecting $P^{+\prime}_{\mathrm{hd,acc}}$, Eq. (4.16) becomes

$$\begin{aligned} P_{\mathrm{v}}^{+} - P_{\mathrm{g}}^{+} = \rho_{\mathrm{l}}^{+} \left(\frac{3}{2} + 4\pi R_{\mathrm{d}}^{+2} n^{+} R_{\mathrm{b}}^{+} \right) \left(\frac{\mathrm{d}R_{\mathrm{b}}^{+}}{\mathrm{d}t^{+}} \right)^{2} + \frac{4}{R_{\mathrm{b}}^{+}} \frac{\mu_{\mathrm{l}}^{+}}{\mathrm{Re_b}} \frac{\mathrm{d}R_{\mathrm{b}}^{+}}{\mathrm{d}t^{+}} \\ + 4\pi n^{+} \rho_{\mathrm{l}}^{+} R_{\mathrm{d}}^{+} R_{\mathrm{b}}^{+2} \left(\frac{\mathrm{d}R_{\mathrm{d}}^{+}}{\mathrm{d}t^{+}} \right) \left(\frac{\mathrm{d}R_{\mathrm{b}}^{+}}{\mathrm{d}t^{+}} \right) + \frac{2\sigma^{+}}{\mathrm{We_b}} \frac{1}{R_{\mathrm{b}}^{+}}. \end{aligned} \tag{4.19}$$

Defining

$$X = \rho_{\mathrm{l}}^{+} \left(\frac{3}{2} + 4\pi R_{\mathrm{d}}^{+2} n^{+} R_{\mathrm{b}}^{+} \right), \tag{4.20}$$

$$Y = 4 \left\{ \frac{\mu_{\mathrm{l}}^{+}}{R_{\mathrm{b}}^{+} \mathrm{Re_b}} + \pi n^{+} \rho_{\mathrm{l}}^{+} R_{\mathrm{d}}^{+} R_{\mathrm{b}}^{+2} \left(\frac{\mathrm{d}R_{\mathrm{d}}^{+}}{\mathrm{d}t^{+}} \right) \right\}, \tag{4.21}$$

$$Z = \left\{ \frac{2\sigma^{+}}{\mathrm{We_b}} \frac{1}{R_{\mathrm{b}}^{+}} - \left(P_{\mathrm{v}}^{+} - P_{\mathrm{g}}^{+} \right) \right\}, \tag{4.22}$$

Eq. (4.19) becomes

$$X \left(\frac{\mathrm{d}R_{\mathrm{b}}^{+}}{\mathrm{d}t^{+}} \right)^{2} + Y \left(\frac{\mathrm{d}R_{\mathrm{b}}^{+}}{\mathrm{d}t^{+}} \right) + Z = 0. \tag{4.23}$$

Treating Eq. (4.23) as a quadratic equation for $\mathrm{d}R_{\mathrm{b}}^{+}/\mathrm{d}t^{+}$, it can be analytically solved for $\mathrm{d}R_{\mathrm{b}}^{+}/\mathrm{d}t^{+}$ as

$$\left(\frac{\mathrm{d}R_{\mathrm{b}}^{+}}{\mathrm{d}t^{+}} \right) = \frac{-Y \pm \sqrt{Y^2 - 4XZ}}{2X}. \tag{4.24}$$

Replacing X, Y, and Z from Eq. (4.20), Eq. (4.21), and Eq. (4.22), respectively, into Eq. (4.24) and assuming the temporal variation of ρ_{l}^{+}, μ_{l}^{+}, and σ^{+}, to

be negligible, one obtains

$$\left(\frac{\mathrm{d}R_\mathrm{b}^+}{\mathrm{d}t^+}\right) = -\frac{2\left\{\frac{1}{R_\mathrm{b}^+\mathrm{Re}} + \pi n^+ R_\mathrm{d}^+ R_\mathrm{b}^{+2}\left(\frac{\mathrm{d}R_\mathrm{d}^+}{\mathrm{d}t^+}\right)\right\}}{\frac{3}{2} + 4\pi R_\mathrm{d}^{+2} n^+ R_\mathrm{b}^+} + \sqrt{4\left\{\frac{\frac{1}{R_\mathrm{b}^+\mathrm{Re}_\mathrm{b}} + \pi n^+ R_\mathrm{d}^+ R_\mathrm{b}^{+2}\left(\frac{\mathrm{d}R_\mathrm{d}^+}{\mathrm{d}t^+}\right)}{\frac{3}{2} + 4\pi R_\mathrm{d}^{+2} n^+ R_\mathrm{b}^+}\right\}^2 - \frac{\left\{\frac{2}{R_\mathrm{b}^+\mathrm{We}_\mathrm{b}} - \left(P_\mathrm{v}^+ - P_\mathrm{g}^+\right)\right\}}{\left(\frac{3}{2} + 4\pi R_\mathrm{d}^{+2} n^+ R_\mathrm{b}^+\right)}}. \tag{4.25}$$

The negative root does not have physical significance in the context of vapor bubble growth in superheated microdroplets, and therefore is neglected in this study. Eq. (4.25) describes the simplified semi-analytical solution for the bubble growth, which needs to be numerically integrated to obtain the bubble radius. The assumptions considered to derive Eq. (4.25) are summarized as: (1) spherical symmetric bubble; (2) $R_\mathrm{b}/R_\mathrm{d} \ll 1$; (3) $n^+ =$ constant; (4) $P_{\mathrm{hd,acc}}^{+\prime} \approx 0$, and (5) $\rho_\mathrm{l}^+ \approx \mu_\mathrm{l}^+ \approx \sigma^+ \approx 1$.

Fig. 4.6 compares the numerically obtained nondimensional radius-time behavior of the OME_1 vapor bubble with the dimensionless semi-analytical solution for three Reynolds numbers of 31.35 (Fig. 4.6a), 5.06 (Fig. 4.6b), and 0.85 (Fig. 4.6c), as listed in Table 4.2. The three different Re_b cases are chosen based on the different superheating degrees ranging from very low ($\Delta\theta = 6$ K) to super-high ($\Delta\theta = 150$ K) values. We have considered the numerical solution of the modified RPE (Eq. (4.16)) as the reference to validate the proposed semi-analytical solution. It is observed from Fig. 4.6 that the semi-analytical solution underpredicts the bubble growth behavior for all the investigated cases. This is expected due to the neglection of the acceleration term in the derivation of Eq. (4.25). Nevertheless, it can be seen that the underprediction reduces with decreasing Re. This is because the acceleration term becomes less significant with decreasing Re as also revealed by the analysis of the order of magnitude of the different pressure terms in Fig. 4.5. Overall, it can be concluded that the simplified nondimensional semi-analytical solution provides a good approximation of the bubble evolution for the whole bubble lifetime.

It has to be noted that the derived semi-analytical solution does not depend on the source (e.g., turbulence, throttling effect, etc.) and location of inception (e.g., inside or outside of the injector nozzle) of the vapor bubble. As soon as a bubble nucleates in a superheated liquid medium, it can be used to reasonably predict the bubble evolution until the liquid jet (or droplet) bursts even with

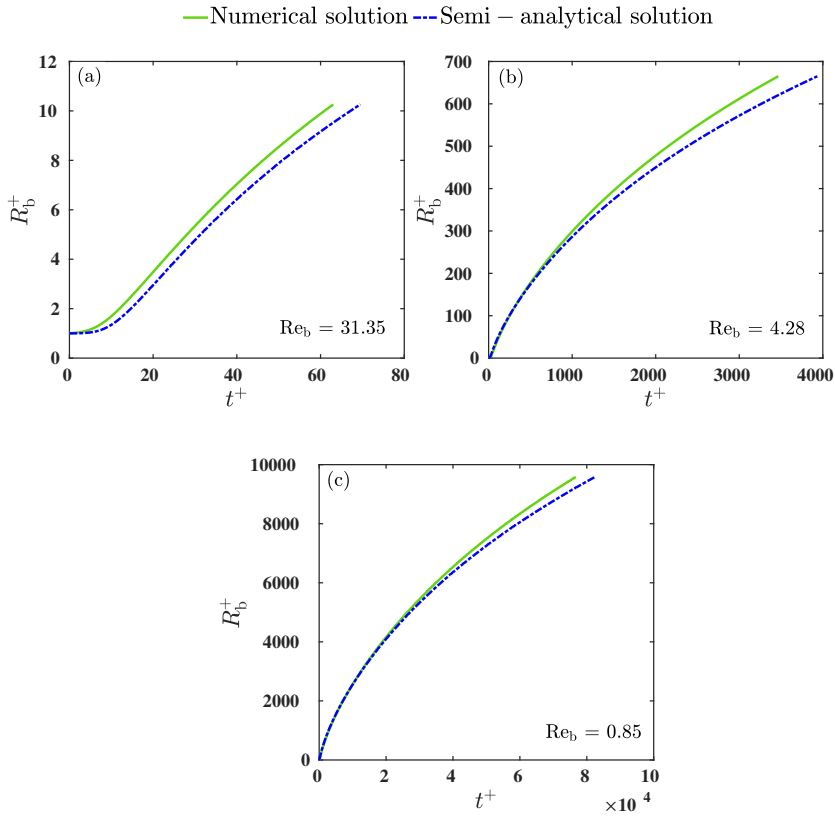

Figure 4.6: Comparison of the dimensionless radius of the superheated OME_1 vapor bubbles obtained from the numerical solution of Eq. (4.16)) with the simplified semi-analytical solution of Eq. (4.25) for (a) $\mathrm{Re_b} = 31.35$ (Case 'HRe'), (b) $\mathrm{Re_b} = 5.06$ (Case 'MRe'), and (d) $\mathrm{Re_b} = 0.85$ (Case 'LRe'). The detailed physical parameters of all the three simulated test cases are listed in Table 4.2.

the larger time-step sizes compared to the numerical approach.

4.4 Computational Cost

The proposed semi-analytical solution is found to accurately predict the bubble growth behavior with a time-step size of $\Delta t = 1 \times 10^{-8}$ s, whereas a much smaller time-step size is required by the numerical solver (as described in Section 4.2), thus substantially increasing the required number of time-steps. In order to demonstrate the capability of the derived semi-analytical solution, the numerical and semi-analytical predictions of the bubble growth characteristics for OME_1 microdroplet are shown in Fig. 4.7 for $P_g = 0.8$ bar, $T_d = 428.71$ K, and $\Delta\theta = 120$ K with $\Delta t = 1 \times 10^{-8}$ s. It is observed in Fig. 4.7 that the semi-analytical solution accurately captures the growth characteristics of the vapor bubbles regardless of the large time-step size, whereas the numerical approach results in an unphysical bubble growth rate and vapor temperature, as described in Section 4.2.

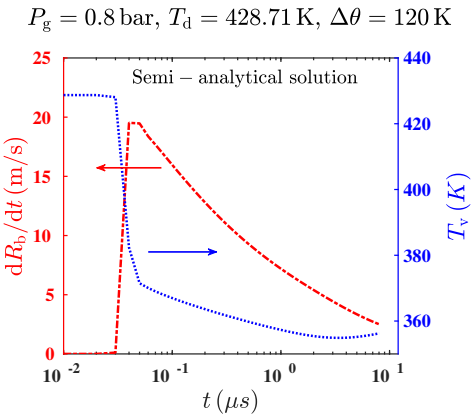

Figure 4.7: Bubble growth characteristics of OME_1 microdroplets considering the bubble-bubble interactions predicted by the proposed semi-analytical solution for bubble growth (Eq. (4.25)) with $\Delta t = 1 \times 10^{-8}$s.

Five different cases with superheating degrees ranging from 80 K (Case 'A-80') to 150 K (Case 'E-150') are investigated to illustrate the reduction of the computational cost with the derived semi-analytical formulation. In this work, all the simulations are performed on machines using the Intel Broadwell processor architecture. The simulation parameters are listed in Table 4.3. The semi-analytical solution is found to accelerate the computing speed

significantly for all the investigated cases, as shown by factor x in Table 4.3. Thus, for large-scale spray simulations with millions of microdroplets [93], the semi-analytical solution would be very beneficial to speed up the whole computation process.

Case ↓	P_l	T_d	$\Delta\theta$	Δt_{num}	Δt_{anlt}	t_{num}	t_{anlt}	**x**
Unit →	bar	K	K	s	s	CPUh	CPUh	-
A-80	0.3	364.72	80	1×10^{-9}	1×10^{-8}	0.0021	1.2792×10^{-4}	16.42
B-100	0.3	384.72	100	1×10^{-9}	1×10^{-8}	0.0016	9.8798×10^{-5}	16.19
C-120	0.8	428.71	120	1×10^{-11}	1×10^{-8}	0.6581	3.7546×10^{-4}	1752.78
D-135	0.6	436.20	135	1×10^{-11}	1×10^{-8}	0.6664	3.4923×10^{-4}	1908.20
E-150	0.3	434.72	150	1×10^{-11}	1×10^{-8}	0.1444	3.4146×10^{-4}	422.89

Table 4.3: Simulation test cases of OME_1 microdroplets for demonstrating the computational cost reduction with the proposed semi-analytical solution. Subscripts 'num' and 'anlt' denote numerical and analytical solver, respectively.

4.5 Conclusions

The numerical challenges associated with the proposed bubble growth model for the accurate prediction of the vapor bubble growth process were highlighted for highly volatile liquid fuels using OME_x as a generic example. It was found that for certain operating conditions, the numerical approach requires an extremely small time-step size to accurately capture the bubble growth rate as well as the temperature at the liquid-vapor interface, thus hindering the simulation of large-scale flash-boiling spray cases due to the high computational cost associated with it.

Realizing the need for developing a simple correlation for bubble growth, a scaling law was first explored in this study to assess its ability to characterize bubble growth for superheated microdroplet cases under subatmospheric operating conditions. It was observed that the scaling law does not result in a perfect collapse of the scaled radius-time curves over the whole lifetime of the vapor bubble.

To derive a simplified solution of the modified RPE, a dimensional analysis was performed for different orders of magnitudes of Reynolds numbers. It was revealed that the nondimensional acceleration term possesses much lower significance in determining the bubble growth characteristics as the order of

magnitude of the Re is decreased from $\mathcal{O}(10^1)$ to $\mathcal{O}(10^0)$. Thus, neglecting this term, a simple semi-analytical solution was derived for the bubble growth rate considering the bubble-bubble interactions and validated for different operating conditions against its numerical solution. The derived semi-analytical solution for bubble growth was found to provide a good approximation of the bubble radius as a function of nondimensional time.

A posteriori computational cost analysis for the single droplet cases also revealed that the proposed semi-analytical solver is significantly faster compared to the numerical solver; thus, it may be used in many practical applications including but not limited to flash-boiling spray simulations with millions of single droplets in automotive or cryogenic engines, where tracking of bubble growth phases in an individual droplet by solving the full RPE simultaneously with the energy balance at the liquid-vapor interface may be computationally very expensive.

5 LES of Flash-boiling Spray

In the previous chapter, a semi-analytical solution for bubble growth in a superheated microdroplet considering bubble-bubble interactions was developed, which was shown to be cost-efficient in comparison to the numerical solution of the modified RPE. In this chapter, an LES of flash-boiling spray is performed by incorporating the newly developed semi-analytical solution. Subsequently, the spray characteristics predicted by the simulation are compared with the experimental measurements. A two-way coupled 3D Eulerian-Lagrangian framework is considered, where the dispersed liquid phase is modeled as a Lagrangian point particle and the continuous gas phase is solved in Eulerian form.

The present chapter is organized as follows: The gas phase modeling is described in Section 5.1. Section 5.2 highlights the Lagrangian modeling approach for the liquid phase. The numerical methodology is discussed in Section 5.3. Section 5.4 outlines the liquid fuel injection method. The simulation setup is described in Section 5.5. The spray results are presented in Section 5.6. Finally, the findings are summarized in Section 5.7.

5.1 Gas Phase Modeling

The mass and momentum conservation governing the continuous compressible gas phase are given by the Navier-Stokes equations (NSEs) as

$$\frac{\partial \rho_{\mathrm{g}}}{\partial t} + \frac{\partial \rho_{\mathrm{g}} u_{\mathrm{g},j}}{\partial x_j} = \dot{S}_{\mathrm{m}}, \tag{5.1}$$

$$\frac{\partial \rho_{\mathrm{g}} u_{\mathrm{g},i}}{\partial t} + \frac{\partial \rho_{\mathrm{g}} u_{\mathrm{g},j} u_{\mathrm{g},i}}{\partial x_j} = -\frac{\partial P_{\mathrm{g}}}{\partial x_i} + \frac{\partial \tau_{ij}}{\partial x_j} + \dot{S}_{u_i}, \tag{5.2}$$

where 'i' and 'j' denote the Cartesian directions, u_{g} is the gas velocity, τ_{ij} the stress tensor, and x the spatial coordinate. The volumetric mass source term, $\dot{S}_{\mathrm{m}}$, represents the vapor mass added to the gas phase due to liquid evaporation. $\dot{S}_{u_i}$ describes the volumetric momentum source term resulting from the momentum transfer between the gas and liquid phase. In addition to the mass and momentum conservation, the compressibility of the gas phase

requires the solution of an energy conservation equation, which is formulated in this study based on the internal energy and given by

$$\frac{\partial \rho_{\mathrm{g}} e_{\mathrm{g}}}{\partial t}+\frac{\partial \rho_{\mathrm{g}} u_{\mathrm{g},j} e_{\mathrm{g}}}{\partial x_{\mathrm{j}}}=-P_{\mathrm{g}} \frac{\partial u_{\mathrm{g},j}}{\partial x_j}+\tau_{ij} \frac{\partial u_{\mathrm{g},i}}{\partial x_j}+\frac{\partial}{\partial x_j}\left(\lambda_{\mathrm{g}} \frac{\partial T_{\mathrm{g}}}{\partial x_j}\right)-\frac{\partial q''}{\partial x_j}+\dot{S}_e, \quad (5.3)$$

where e_{g} is the gas-phase internal energy, q'' the enthalpy flux due to mass diffusion, and $\dot{S}_{\mathrm{e}}$ the volumetric energy source/sink term. The source terms are calculated based on the dynamics of the dispersed liquid phase, which will be discussed in the following sections. An ideal gas equation of state is used to close the system of equations (Eq. (5.1)-(5.3)) shown above:

$$P_{\mathrm{g}}=\frac{\rho_{\mathrm{g}} \mathcal{R} T_{\mathrm{g}}}{W}, \quad (5.4)$$

where W denotes the gas-mixture molar mass. Although the governing equations completely describe the behavior of a flow field, it is computationally expensive to resolve all the lengths and time scales associated with it. Thus, a spatial low-pass filtering is performed in order to dampen out the smaller-scale motions while retaining the unsteady large-scale turbulent structures. The unclosed terms in the filtered governing equations are modeled using a dynamic Smagorinsky subfilter model considering Lagrangian averaging [101].

5.2 Liquid Phase Modeling

The Lagrangian point particle approach is considered in this study to model the dispersed liquid phase. The Lagrangian equations governing the single droplet position, velocity, mass, and temperature are solved [91]. Both the internal and external vaporization processes of the superheated droplets are considered. Due to the smaller size of the droplets in flash-boiling sprays, the conductive thermal resistance in the superheated liquid droplets is neglected and the droplet bulk temperature is modeled using an infinite conductivity model proposed by Miller and Bellan [91]. The breakup is modeled via a hybrid breakup model which considers both the aerodynamic and flash-boiling induced breakup mechanisms. The dispersed phase modeling approaches are discussed in detail in the following sections.

5.2.1 Modeling of Droplet Motion

The transient position ($x_{\mathrm{d},i}$) and velocity ($u_{\mathrm{d},i}$) of the Lagrangian droplets are obtained by solving [91]

$$\frac{\mathrm{d}x_{\mathrm{d},i}}{\mathrm{d}t} = u_{\mathrm{d},i}, \tag{5.5}$$

$$\frac{\mathrm{d}u_{\mathrm{d},i}}{\mathrm{d}t} = \dot{u}_{\mathrm{d},i} = \frac{f_1}{\tau_{\mathrm{d}}}\left(u_{\mathrm{g},i} - u_{\mathrm{d},i}\right), \tag{5.6}$$

where 'g' and 'd' the gas and droplet quantities, respectively. The particle drag force correction factor, f_1, is given by [102]

$$f_1 = 1 + 0.15{\mathrm{Re}_{\mathrm{d,sl}}}^{0.687} + \mathrm{H}\left(\mathrm{Re}_{\mathrm{d,sl}} - 100\right) \cdot \left(\frac{0.0175\mathrm{Re}_{\mathrm{d,sl}}}{1 + 4.25 \times 10^4 {\mathrm{Re}_{\mathrm{d,sl}}}^{-1.16}}\right), \tag{5.7}$$

where $\mathrm{Re}_{\mathrm{d,sl}}$ is the droplet slip Reynolds number expressed as

$$\mathrm{Re}_{\mathrm{d,sl}} = \frac{d_{\mathrm{d}}\rho_{\mathrm{g}}}{\mu_{\mathrm{g}}}\left\{\sum\left(u_{\mathrm{g,i}} - u_{\mathrm{d,i}}\right)^2\right\}^{1/2}. \tag{5.8}$$

In Eq. (5.7), H represents a Heaviside function, which becomes active only when $\mathrm{Re}_{\mathrm{d,sl}}$>100.

5.2.2 Modeling of Droplet Vaporization

As described in Chapter 2, the phase transition in superheated liquid droplet occurs in two distinct ways: (1) by spontaneous nucleation and subsequent growth of the vapor bubbles in the droplet and (2) by vaporization from the droplet's external surface due to the internal as well as external temperature gradient [59, 103]. The rate of change of fuel vapor mass flow due to the internal vaporization is obtained as

$$\frac{\mathrm{d}}{\mathrm{d}t}\left(m_{\mathrm{i}}\right) = \dot{m}_{\mathrm{i}} = 4\pi R_{\mathrm{b}}^2 \dot{R}_{\mathrm{b}} \rho_{\mathrm{v}} N_{\mathrm{bub}}, \tag{5.9}$$

where $\dot{R}_{\mathrm{b}}$ is the analytical bubble growth rate in a multibubble environment given by

$$\dot{R}_{\mathrm{b}} = -\frac{2\left[\frac{\mu_l}{R_{\mathrm{b}}} + \pi n \rho_{\mathrm{l}} R_{\mathrm{d}} R_{\mathrm{b}}^2 \left(\frac{\mathrm{d}R_{\mathrm{d}}}{\mathrm{d}t}\right)\right]}{\rho_l\left(\frac{3}{2} + 4\pi R_{\mathrm{d}}^2 n R_{\mathrm{b}}\right)} + \left\{4\left[\frac{\frac{\mu_l}{R_{\mathrm{b}}} + \pi n \rho_{\mathrm{l}} R_{\mathrm{d}} R_{\mathrm{b}}^2 \left(\frac{\mathrm{d}R_{\mathrm{d}}}{\mathrm{d}t}\right)}{\rho_l\left(\frac{3}{2} + 4\pi R_{\mathrm{d}}^2 n R_{\mathrm{b}}\right)}\right]^2 - \frac{\left\{\frac{2\sigma}{R_{\mathrm{b}}} - \left(P_{\mathrm{v}} - P_{\mathrm{g}}\right)\right\}}{\rho_l\left(\frac{3}{2} + 4\pi R_{\mathrm{d}}^2 n R_{\mathrm{b}}\right)}\right\}^{1/2}. \tag{5.10}$$

where T_{v} is assumed to be in equilibrium with the droplet bulk temperature T_{d}. The flash-boiled vapor mass flow rate due to the heat transfer from the droplet's inner core to the outer surface is calculated using the formulation proposed by Adachi et al. [25], as described in Chapter 2. The external phase transition may also take place due to the temperature gradient between the droplet outer interface and the ambient gas. In general, depending on the ambient conditions, the heat transfer would take place in two different ways: (1) when $T_{\mathrm{s}} > T_{\mathrm{g}}$, there will be heat transfer from the droplet external surface to the ambient; and (2) in the case of $T_{\mathrm{s}} < T_{\mathrm{g}}$, the heat transfer would take place from the external ambient medium to the droplet outer surface. In Chapter 2, the external phase transition rate was calculated using the model derived by Zuo et al. [68]. However, the formulation proposed by Zuo et al. [68] will not be valid for the case of $T_{\mathrm{s}} > T_{\mathrm{g}}$. Thus, in this chapter, a more general approach for the calculation of the fuel vapor mass flow rate due to the temperature gradient between the droplet external surface and the ambient medium is employed as [25]

$$\frac{\mathrm{d}}{\mathrm{d}t}\left(m_{\mathrm{ex}}\right) = \dot{m}_{\mathrm{ex}} = \frac{h_{\mathrm{ex}} f_3 \left|T_{\mathrm{g}} - T_{\mathrm{s}}\right| A}{L_{\mathrm{v}}\left(T_{\mathrm{s}}\right)}, \tag{5.11}$$

where h_{ex} represents the coefficient of heat transfer from the external ambient. The additional Stefan flow caused by the mass flux due to the heat transfer from the droplet inner core counteracts the external temperature gradient-based vaporization process and may significantly reduce the heat flux to/from the droplet outer surface [68]. The factor f_3 is an evaporative heat transfer correction factor, which is introduced here to take into account the above-mentioned phenomena, and is defined as

$$f_3 = \frac{1}{1 - \mathrm{PR}} \quad \text{with} \quad \mathrm{PR} = \frac{P_{\mathrm{g}}}{P_{\mathrm{v}}(T_{\mathrm{d}})}. \tag{5.12}$$

When the superheated liquid droplet cools down to the temperature below T_{b}, the standard non-equilibrium evaporation model proposed by Miller and Bellan [91] is used to model the vaporization process. The mass flow rate from the droplet external surface in the sub-cooled regime is given by [91]

$$\frac{\mathrm{d}}{\mathrm{d}t}\left(m_{\mathrm{ex}}\right) = \dot{m}_{\mathrm{ex}} = \frac{\mathrm{Sh}_{\mathrm{d}}}{3\mathrm{Sc}_{\mathrm{g}}} \frac{m_{\mathrm{d}}}{\tau_{\mathrm{d}}} \ln\left(1 + \mathrm{B}_{\mathrm{M,d}}\right), \tag{5.13}$$

where $\mathrm{B}_{\mathrm{M,d}}$ is the Spalding mass transfer number given by

$$\mathrm{B}_{\mathrm{M,d}} = \frac{Y_{\mathrm{v,s}} - Y_{\infty,\mathrm{v}}}{1 - Y_{\mathrm{v,s}}}, \tag{5.14}$$

where the non-equilibrium fuel vapor mass fraction at the droplet surface, $Y_{\mathrm{v,s}}$, is expressed as

$$Y_{\mathrm{v,s}} = \frac{\chi_{\mathrm{neq\ ,v,s}}}{\chi_{\mathrm{neq,v,s}} + (1 - \chi_{\mathrm{neq,v,s}})\,\mathrm{W_a/W_l}}. \tag{5.15}$$

$\mathrm{W_a}$ and $\mathrm{W_l}$ are the molar masses of ambient gas (excluding vapor) and liquid fuel, respectively, and $\chi_{\mathrm{neq,v,s}}$ the non-equilibrium droplet surface vapor mole fraction given by [91]

$$\chi_{\mathrm{neq,v,s}} = \chi_{\mathrm{eq,v,s}} - \left(\frac{2L_{\mathrm{k}}}{d_{\mathrm{d}}}\right)\xi_{\mathrm{sub}}. \tag{5.16}$$

The equilibrium surface vapor mole fraction, $\chi_{\mathrm{eq,v,s}}$, is obtained as

$$\chi_{\mathrm{eq,v,s}} = \frac{P_{\mathrm{v}}\,(T_{\mathrm{s}})}{P_{\mathrm{g}}}. \tag{5.17}$$

The vapor pressure P_{v} corresponding to T_{s} is calculated directly from the NIST property database [104]. In Eq. (5.16), L_{k} denotes the molecular Knudsen layer thickness and is defined as [91]

$$L_{\mathrm{k}} = \frac{\mu_{\mathrm{g}}\,(2\pi T_{\mathrm{s}}\mathcal{R}/W_{\mathrm{v}})^{1/2}}{\mathrm{Sc_g Pr_g}}, \tag{5.18}$$

where $\mathcal{R}$ is the universal gas constant. ξ_{sub} describes the dimensionless evaporation parameter in the subcooled regime:

$$\xi_{\mathrm{sub}} = -\left(\frac{3\mathrm{Pr_g}\tau_{\mathrm{d}}}{2}\right)\frac{\dot{m}_{\mathrm{ex}}}{m_{\mathrm{d}}}. \tag{5.19}$$

$\mathrm{Sh_d}$ is the Sherwood number computed using Ranz and Marshall [105] correlation as

$$\mathrm{Sh_d} = 2 + 0.552{\mathrm{Re_{d,sl}}}^{1/2}{\mathrm{Sc_g}}^{1/3}. \tag{5.20}$$

The gas-phase Schmidt number, $\mathrm{Sc_g}$, and Prandtl number, $\mathrm{Pr_g}$, are defined as

$$\mathrm{Sc_g} = \frac{\mu_{\mathrm{g}}\,(T_{\mathrm{ref}})}{\rho_{\mathrm{g}}\,(T_{\mathrm{ref}})\,\Gamma_{\mathrm{v,g}}\,(T_{\mathrm{ref}})}, \quad \mathrm{Pr_g} = \frac{\mu_{\mathrm{g}}\,(T_{\mathrm{ref}})\,C_{\mathrm{p,g}}\,(T_{\mathrm{ref}})}{\lambda_{\mathrm{g}}\,(T_{\mathrm{ref}})}, \tag{5.21}$$

where μ_{g} and ρ_{g} denote the viscosity and density of the gas-phase mixture evaluated at reference temperature (T_{ref}) obtained by the one-third rule as [92]

$$T_{\mathrm{ref}} = \frac{T_{\mathrm{g}} + 2T_{\mathrm{s}}}{3}. \tag{5.22}$$

The droplet surface temperature T_{s} is assumed to be equal to T_{b} and T_{d} in the superheated and subcooled regimes, respectively.

5.2.3 Modeling of Heat Transfer Process

Due to the smaller size of the droplets in flash-boiling sprays, the conductive thermal resistance in the superheated liquid droplets is neglected and the droplet bulk temperature is modeled using an infinite conductivity model proposed by Miller and Bellan [91]. The rate of change of droplet bulk droplet temperature in the superheated regime is obtained as

$$\frac{\mathrm{d}T_\mathrm{d}}{\mathrm{d}t} = \frac{\mathrm{Nu_d}}{3\mathrm{Pr_g}} \frac{C_\mathrm{p,g}}{C_\mathrm{l}} \frac{f_\mathrm{2,sup}}{\tau_\mathrm{d}} \left(T_\mathrm{g} - T_\mathrm{s}\right) - \frac{\dot{m}_\mathrm{i} L_\mathrm{v}\left(T_\mathrm{d}\right)}{m_\mathrm{d} C_\mathrm{l}} - \frac{\dot{m}_\mathrm{t} L_\mathrm{v}\left(T_\mathrm{s}\right)}{m_\mathrm{d} C_\mathrm{l}}, \tag{5.23}$$

where $\dot{m}_\mathrm{t}$ describes the total fuel vapor mass flow rate from the droplet's external surface and is defined as

$$\frac{\mathrm{d}}{\mathrm{d}t}\left(m_\mathrm{t}\right) = \dot{m}_t = \dot{m}_\mathrm{f} + \dot{m}_\mathrm{ex}. \tag{5.24}$$

The Nusselt number $\mathrm{Nu_d}$ is computed using Ranz and Marshall [105] correlations as

$$\mathrm{Nu_d} = 2 + 0.552 {\mathrm{Re_{d,sl}}}^{1/2} {\mathrm{Pr_g}}^{1/3}. \tag{5.25}$$

In Eq. (5.24), $f_\mathrm{2,sup}$ denotes the external heat transfer correction factor in the superheated regime and is given by

$$f_\mathrm{2,sup} = \frac{\xi_\mathrm{sup}}{e^{\xi_\mathrm{sup}} - 1} \quad \text{with} \quad \xi_\mathrm{sup} = -\left(\frac{3\mathrm{Pr_g}\tau_\mathrm{d}}{2}\right)\frac{\dot{m}_\mathrm{t}}{m_\mathrm{d}}. \tag{5.26}$$

For subcooled droplet, the conductive heat flow and the external vaporization are solely responsible for the change in droplet bulk temperature, and thus energy balance at the droplet surface can be expressed as

$$\frac{\mathrm{d}T_\mathrm{d}}{\mathrm{d}t} = \frac{\mathrm{Nu_d}}{3\mathrm{Pr_g}} \frac{C_\mathrm{p,g}}{C_\mathrm{l}} \frac{f_\mathrm{2,sub}}{\tau_\mathrm{d}} \left(T_\mathrm{g} - T_\mathrm{s}\right) - \frac{\dot{m}_\mathrm{ex} L_\mathrm{v}\left(T_\mathrm{s}\right)}{m_\mathrm{d} C_\mathrm{l}}, \tag{5.27}$$

where

$$f_\mathrm{2,sub} = \frac{\xi_\mathrm{sub}}{e^{\xi_\mathrm{sub}} - 1}. \tag{5.28}$$

5.2.4 Modeling of Droplet Breakup

The superheating degree plays an important role in determining the flash-boiling spray atomization characteristics. The spontaneous growth of the vapor bubbles and the aerodynamic forces compete with each other during the flash-boiling spray atomization process. Micro-explosions due to the

bubble growth dominate in the regime of high superheating degrees, whereas aerodynamic forces dominate in low superheating degree regimes [72]. Thus, in this work, a hybrid breakup model which includes both the aerodynamic and flash-boiling induced breakup (herein referred to as 'thermal breakup') mechanisms is considered for modeling the droplet breakup processes.

Thermal Breakup

Bubbles inside the superheated liquid droplet can grow up to a certain limit, which, if exceeded, will lead to the bursting of the droplet. The onset of droplet bursting depends on several parameters such as surface tension, viscosity of the liquid, and the droplet diameter. The number density of the bubble nuclei, the growth rate, and the interaction between multiple bubbles also play an important role in determining the onset of droplet burst [106]. The void fraction, ϵ, is used to obtain the limit of the bubble growth [19]. The droplet is considered to burst when ϵ reaches its critical value of ϵ_{crit}. The definition of ϵ proposed by Senda et al. [19] is considered here, as already described in Chapter 2 and a critical void fraction value of 0.55 is used, as suggested by Kawano et al. [58].

The total number of child droplets ($N_{\text{c,thm}}$) resulting from the thermal breakup is considered to be twice the number of vapor bubbles in the respective parent droplet [19]. Based on mass conservation, the child droplet diameter, $d_{\text{c,thm}}$, is calculated as

$$m_{\text{p}} = N_{\text{c,thm}} \frac{4}{3} \pi \rho_{\text{l}} r_{\text{c,thm}}^3, \tag{5.29}$$

$$d_{\text{c,thm}} = 2 \left(\frac{3 m_{\text{p}}}{4 N_{\text{c,thm}} \pi \rho_{\text{l}}} \right)^{1/3}, \tag{5.30}$$

where m_{p} is the mass of the parent droplet and $r_{\text{c,thm}}$ the child droplet radius. The velocity of the child droplets is calculated as

$$u_{\text{c},i} = u_{\text{p},i} + u_{\text{r},i}, \tag{5.31}$$

where $u_{\text{p},i}$ denotes the parent droplet velocity and $u_{\text{r},i}$ the additional radial velocity induced on the parent droplet due to the expansion of the vapor bubbles. The magnitude of this radial velocity is calculated as

$$u_{\text{r}} = \sqrt{2 E_{\text{drup}} / m_{\text{p}}}. \tag{5.32}$$

E_{drup} is the disruption energy resulting from the micro-explosion defined as [59]

$$E_{\mathrm{drup}} = -\frac{1}{\gamma - 1} P_{\mathrm{v}} V_{\mathrm{bub}} \left[\left(\frac{P_{\mathrm{v}}}{P_{\mathrm{g}}} \right)^{(1-\gamma)/\gamma} - 1 \right], \tag{5.33}$$

where γ represents the specific heat ratio of the fuel vapor in the bubbles.

Aerodynamic Breakup

Aerodynamic breakup is described using the Kelvin-Helmholtz (KH) – Rayleigh-Taylor (RT) hybrid breakup model. In the KH model, the breakup is assumed to be caused by the instabilities on the liquid surface. The radius of a child droplet resulting from the KH breakup is given by [107]

$$r_{\mathrm{c,KH}} = B_0 \Lambda_{\mathrm{KH}}, \tag{5.34}$$

where the wavelength of the fastest growing KH wave is denoted by Λ_{KH}, and B_0 the model constant equal to 0.61. The wavelength (Λ) and the corresponding frequency (Ω) associated with the fastest growing KH wave can be obtained by numerically solving the dispersion relationship as [108]

$$\Omega_{\mathrm{KH}} = \frac{0.34 + 0.38 \mathrm{We_g}^{1.5}}{(1 + \mathrm{Oh})\left(1 + 1.4 \mathrm{Ta}^{0.6}\right)} \sqrt{\frac{\sigma}{\rho_{\mathrm{l}} r_{\mathrm{p}}^3}}, \tag{5.35}$$

$$\Lambda_{\mathrm{KH}} = \frac{9.02 r_{\mathrm{p}} (1 + 0.45\sqrt{\mathrm{Oh}}) \left(1 + 0.4 \mathrm{Ta}^{0.7}\right)}{\left(1 + 0.865 \mathrm{We_g}^{1.67}\right)^{0.6}}. \tag{5.36}$$

The gas-phase Weber number and Ohnesorge number are defined as

$$\mathrm{We_g} = \frac{\rho_{\mathrm{g}} u_{\mathrm{rel}}^2 r_{\mathrm{p}}}{\sigma}, \quad \mathrm{Oh} = \frac{\sqrt{\mathrm{We_l}}}{\mathrm{Re_l}}, \tag{5.37}$$

where u_{rel} is the relative velocity between the liquid droplets and the gas phase and r_{p} is the parent droplet radius. The liquid Weber number and Reynolds number are defined as

$$\mathrm{We_l} = \frac{\rho_{\mathrm{l}} u_{\mathrm{rel}}^2 r_{\mathrm{p}}}{\sigma}, \quad \mathrm{Re_l} = \frac{\rho_{\mathrm{g}} u_{\mathrm{rel}} r_{\mathrm{p}}}{\mu_{\mathrm{g}}}. \tag{5.38}$$

The Taylor number Ta is defined as

$$\mathrm{Ta} = \mathrm{Oh}\sqrt{\mathrm{We_g}}. \tag{5.39}$$

The regression rate of the parent droplet radius due to the mass loss resulting from the generation of the child droplets is expressed as

$$\frac{\mathrm{d}}{\mathrm{d}t}\left(r_{\mathrm{p}}\right) = \frac{r_{\mathrm{p}} - r_{\mathrm{c,KH}}}{\tau_{\mathrm{KH}}}, \tag{5.40}$$

where the breakup time, τ_{KH}, is defined as [107]

$$\tau_{\mathrm{KH}} = \frac{3.788 B_1 r_{\mathrm{p}}}{\Omega_{\mathrm{KH}} \Lambda_{\mathrm{KH}}}. \tag{5.41}$$

B_1 is an arbitrary model constant which was introduced to consider the unknown effect of in-nozzle flow-field on the initial injected droplet. The value of B_1 lies between 1.73 and 60 [107]. As a second competing breakup mechanism, the RT wave instability on the droplet surface is also considered together with the KH wave breakup model. The wavelength and the corresponding frequency of the fastest-growing RT wave are given by [107]

$$\Lambda_{\mathrm{RT}} = 2\pi\sqrt{\frac{3\sigma}{a\rho_{\mathrm{l}}}}, \quad \Omega_{\mathrm{RT}} = \sqrt{\frac{2a}{3}}\left[\frac{a\rho_{\mathrm{l}}}{3\sigma}\right]^{1/4}, \tag{5.42}$$

where a denotes the droplet acceleration given by [107]

$$a = \frac{3}{8} C_{\mathrm{D}} \frac{\rho_{\mathrm{g}} u_{\mathrm{rel}}^2}{\rho_{\mathrm{l}} r_{\mathrm{p}}}. \tag{5.43}$$

The diameter of the child droplets generated via the RT breakup mechanism is calculated as [107]

$$d_{\mathrm{c,RT}} = C_{\mathrm{RT}} \Lambda_{\mathrm{RT}}, \tag{5.44}$$

where C_{RT} represents the RT breakup model constant. The time scale associated with the RT breakup is calculated by taking the inverse of the fastest growing RT wave frequency as

$$\tau_{\mathrm{RT}} = C_\tau / \Omega_{\mathrm{RT}}, \tag{5.45}$$

where C_τ is the RT breakup time constant. The values of the breakup parameters used in this chapter are summarized in Table 6.4.

Model	Constant	Present work
Kelvin-Helmholtz	B_0	0.61
	B_1	2.0
Rayleigh-Taylor	C_{RT}	0.11
	C_τ	0.4

Table 5.1: Breakup model constants for the aerodynamic breakup mechanism.

5.3 Numerical Methodology

The in-house code CIAO is used to solve the compressible NSEs. CIAO is a structured, high-order, finite-difference code, which solves the NSEs using a central difference scheme. A spatially staggered grid arrangement is incorporated in CIAO to increase the discretization accuracy of the stencils. For time-marching, CIAO uses a low-storage five-stage, explicit Runge-Kutta (RK) scheme. An adaptive time-stepping technique is employed in CIAO during the run time based on a Courant-Friedrichs-Lewy (CFL) criterion. The subgrid stresses are modeled using a dynamic Smagorinsky subfilter model considering Lagrangian averaging [101]. For more details about the flow solver in CIAO, the reader is referred to Desjardins et al. [85] and Mittal et al. [86].

5.4 Liquid Fuel Injection

A blob injection method [108, 109] is incorporated in this study, which injects the droplet with a diameter equivalent to the size of effective nozzle hole diameter into the gas phase. However, during flash-boiling injection, near-nozzle droplet shattering due to rapid disintegration of the superheated liquid jet results in a significant reduction in droplet diameter at the nozzle exit (as low as $\sim$ 10 % of the nozzle hole diameter) [73, 84]. In-nozzle phase change due to the cavitation phenomenon may further enhance the near nozzle atomization characteristics of the superheated liquid jet [110]. The use of an initial droplet of size comparable to the nozzle exit diameter at the flash-boiling conditions would result in an unrealistic flash-boiling spray with no plume merging or spray collapse. The size of the initial droplet diameter is thus crucial in determining the global characteristics of a flash-boiling spray [73, 83]. A correlation proposed by Gemci et al. [110] is used to

compute the initial droplet diameter ($\mathsf{D_o}$) as

$$D_\mathrm{o} = 118.40 - 28.29\,(\Delta\theta^* - \mathrm{CN})\,, \tag{5.46}$$

where

$$\Delta\theta^* = \frac{T_\mathrm{inj} - T_\mathrm{b}\,(P_\mathrm{g})}{T_\mathrm{b}\,(P_\mathrm{inj}) - T_\mathrm{b}\,(P_\mathrm{g})} \quad \text{and} \quad \mathrm{CN} = \frac{P_\mathrm{inj} - P_\mathrm{v}\,(T_\mathrm{inj})}{P_\mathrm{inj} - P_\mathrm{g}}, \tag{5.47}$$

where P_inj is the injection pressure, $\Delta\theta^*$ the dimensionless superheating degree, and CN the cavitation number. The mass flow rate is generated using the virtual injection rate generator provided by CMT [111], which is then used to calculate the velocity profile at the nozzle exit.

An accurate prediction of the widening of the spray plume during flash-boiling injection is necessary to reasonably quantify the macroscopic spray characteristics. In this work, the spray cone angle, θ_1 (in degree), is calculated as [18]

$$\theta_1 = \log\left(\frac{R_\mathrm{p}^2\Theta^3}{m_\mathrm{a}^2}\right), \tag{5.48}$$

where R_p denotes the ratio of saturated vapor pressure (P_v) corresponding to the injection temperature (T_inj) and ambient gas pressure (P_g), and m_a the atomic mass of the injected fuel. Θ is the nondimensional surface tension defined as [112]

$$\Theta = \frac{a\sigma}{k_\mathrm{b}T_\mathrm{inj}} \qquad \text{with} \qquad a = \left(36\pi v_\mathrm{l}^2\right)^{1/3}, \tag{5.49}$$

where k_b is the Boltzmann constant, a the molecular surface area, v_l the liquid molecular volume, and σ the surface tension.

5.5 Simulation Setup

A rectangular box of length $L_\mathrm{x} = 77.5$ mm, width $L_\mathrm{y} = 28$ mm, and depth $L_\mathrm{z} = 28$ mm with no-slip walls is considered as the computational domain. The simulation has been performed on a structured grid with a cell size of 180 μm for a single plume of a 6-hole asymmetric injector nozzle. This resulted in a total cell count of 10.33 million. A schematic of the computational domain is shown in Fig. 5.1. A schematic of the injector used in this study is included in Appendix F. n-pentane is chosen as liquid fuel for the present spray simulation due to its high volatility. It is injected into an ambient environment ($P_\mathrm{g} = 1$

bar) at an injection pressure of $P_{\mathrm{inj}} = 150$ bar. The fuel temperature is set at $T_{\mathrm{inj}} = 363.15$ K, which upon entering the environment would lead to a superheating degree of 54 K.

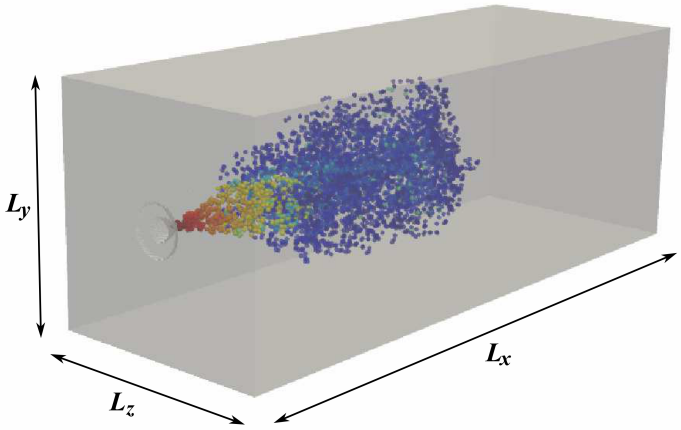

Figure 5.1: Schematic of the computational domain

5.6 Results and Discussion

Fig. 5.2 to Fig. 5.4 describe the spray development of flash-boiling n-pentane fuel at $\Delta\theta = 54$ K. It can be observed from Fig. 5.2 that the superheated liquid fuel droplets gradually cool down over time due to the internal as well as external vaporization processes and eventually enter into the subcooled regime ($T_{\mathrm{d}} < 309$ K). The droplets' temperature is reduced from $T_{\mathrm{inj}} = 363.15$ K to a minimum value of ≈ 245 K as these move downstream. Fig. 5.3 shows that the greater evaporation and enhanced atomization of the liquid droplets cause violent disintegration into smaller child droplets in the near-nozzle region. The smaller droplets are then decelerated slowly due to the aerodynamic drag forces induced by the ambient gas, as shown in Fig. 5.4. Similar to the experiments (see Fig. 5.7), a considerable amount of droplet recirculation due

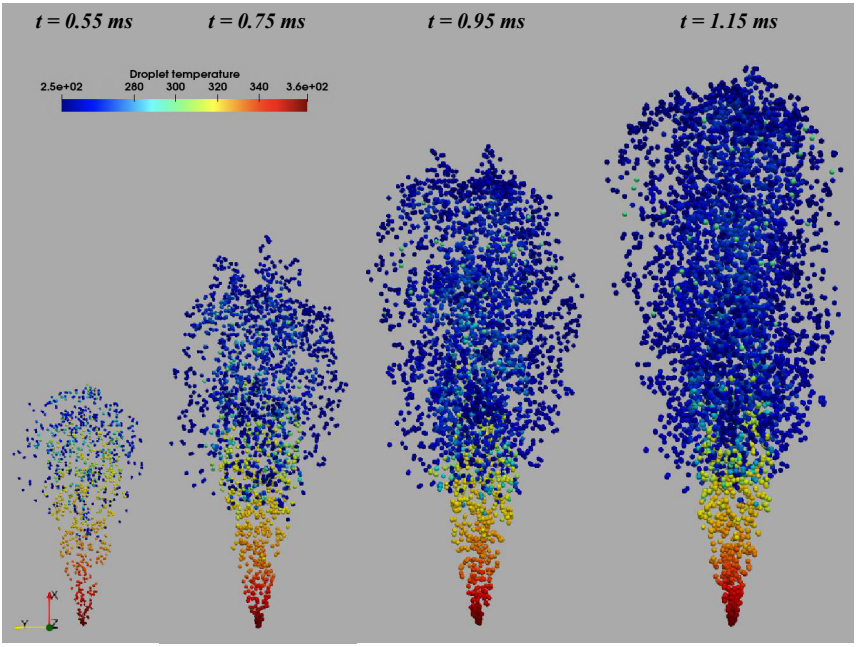

Figure 5.2: Droplet temperature variation in flash-boiling n-pentane spray at $P_{\text{inj}} = 150$ bar, $P_{\text{g}} = 1.0$ bar, and $T_{\text{inj}} = 363.15$ K. The time mentioned above already includes an injector driver delay of 0.3 ms.

to the explosive vaporization and atomization under flash-boiling condition is also observed in the spray plume tip, as can be seen from Fig. 5.4.

Fig. 5.5 shows the comparison between the simulated liquid penetration length of flash-boiling n-pentane spray and the experimental measurements of Aleiferis and van Romunde [4]. Considering the complexity of the flash-boiling phenomena, the liquid penetration length obtained from the LES shows reasonable agreement with the experiment. Fig. 5.6 depicts the variation in Sauter-mean diameter (SMD) predicted from the simulation. It can be seen that a steady-state SMD value of ≈ 7.65 μm is achieved in the simulation, whereas Aleiferis and van Romunde [4] reported a value of 7.89 μm for the steady-state SMD. The SMD value was measured using a Laser diffraction technique at 30 mm along the injector central axis downstream of the nozzle exit in the experiment. For the simulation results, a distance equivalent to that of the experiment is calculated along the spray plume centerline based

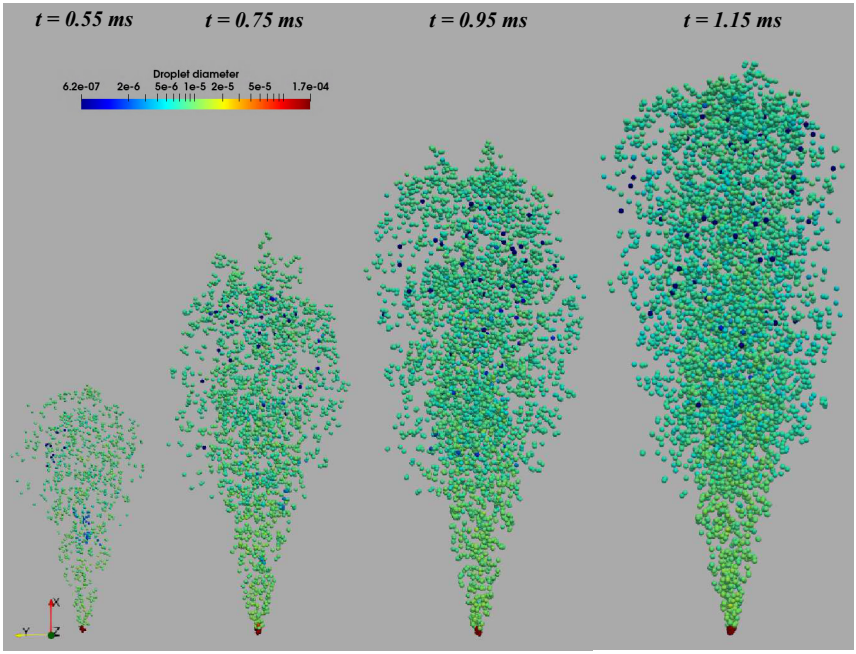

Figure 5.3: Droplet diameter variation in flash-boiling n-pentane spray at $P_{\text{inj}} = 150$ bar, $P_{\text{g}} = 1.0$ bar, and $T_{\text{inj}} = 363.15$ K. The time mentioned above already includes an injector driver delay of 0.3 ms.

on the injector orifice orientations.

It is now worthwhile to assess the effects that the flash-boiling model has made in reproducing the spray characteristics. Therefore, an additional simulation is conducted without the flash-boiling model. The initial droplet diameter for this simulation case is assumed to be equivalent to the nozzle exit diameter and the initial spray cone angle is predicted using the Hiroyasu and Arai [113] correlation (see Appendix G). The breakup of spray droplets is modeled only via the aerodynamic breakup mechanisms with the similar breakup parameters, as listed in Table 6.4. Fig. 5.8 illustrates the comparison between the liquid and vapor penetrations predicted with and without the flash-boiling model. It is observed that liquid and vapor penetrations are clearly overestimated without the flash-boiling model.

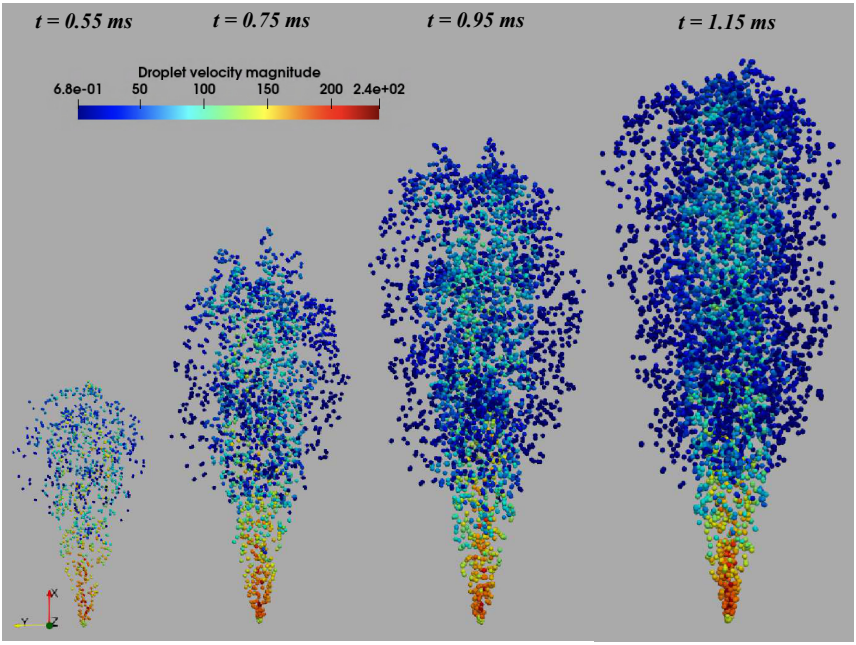

Figure 5.4: Droplet velocity variation in flash-boiling n-pentane spray at $P_{\mathrm{inj}} = 150$ bar, $P_{\mathrm{g}} = 1.0$ bar, and $T_{\mathrm{inj}} = 363.15$ K. The time mentioned above already includes an injector driver delay of 0.3 ms.

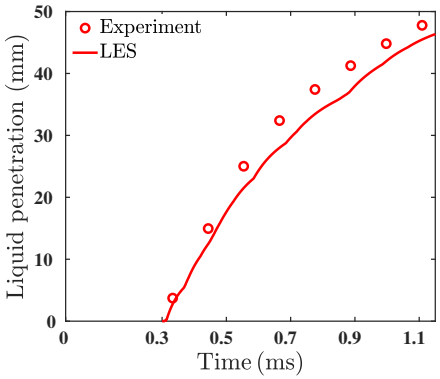

Figure 5.5: Comparison of the liquid penetration length of n-pentane fuel at $P_{\text{inj}} = 150$ bar, $P_{\text{g}} = 1.0$ bar, and $T_{\text{inj}} = 363.15$ K. Experimental results are taken from Aleiferis and van Romunde [4].

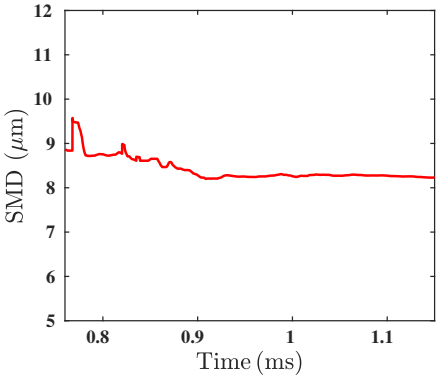

Figure 5.6: Simulated SMD variation of flash-boiling n-pentane fuel spray at $P_{\text{inj}} = 150$ bar, $P_{\text{g}} = 1.0$ bar, and $T_{\text{inj}} = 363.15$ K.

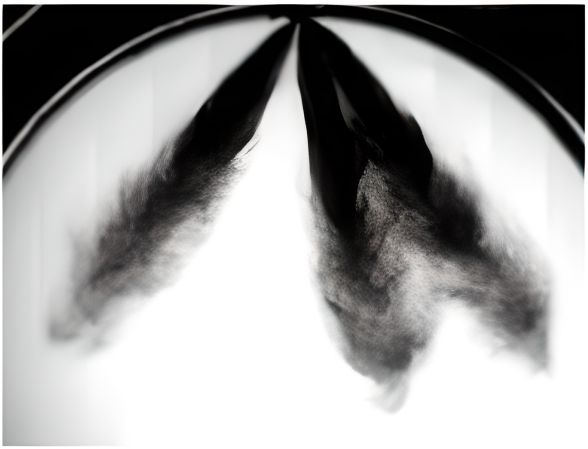

Figure 5.7: Flash-boiling n-pentane spray image measured via Shadowgraphy technique at $P_{\text{inj}} = 150$ bar, $P_{\text{g}} = 1.0$ bar, and $T_{\text{inj}} = 363.15$ K [4].

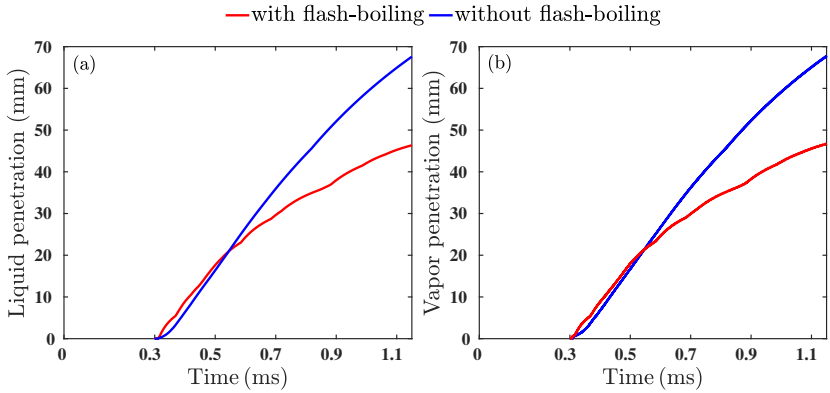

Figure 5.8: Liquid and vapor penetration lengths of n-pentane spray with and without flash-boiling model at $P_{\text{inj}} = 150$ bar, $P_{\text{g}} = 1.0$ bar, and $T_{\text{inj}} = 363.15$ K.

5.7 Conclusions

An LES of a flash-boiling spray was performed using a two-way coupled LPT technique with the newly derived bubble growth model considering bubble interactions. The superheated droplet vaporization was modeled considering both the internal and external vaporization processes. In the subcooled regime, a standard non-equilibrium vaporization model was used. A hybrid breakup model that combines both aerodynamic and flash-boiling induced breakup mechanisms was utilized to simulate the process of droplet breakup. The experimental measurements of liquid penetration length and steady-state SMD were used as benchmarks for comparing the simulation results. The comparison showed reasonable agreement between the simulation and the experiment. The effective improvements of the spray characteristics with the integrated flash-boiling model were also highlighted.

6 Cross-sectionally Averaged Spray Model

Most of the previous studies related to the topic focused on modeling flash-boiling sprays using 3D CFD techniques such as DNS, LES, and RANS. Although it is necessary to study the detailed spray characteristics using 3D CFD approaches, reduced-order models can have significant advantages for applications such as the design of experiments, screening novel fuel candidates, and creating digital twins for instance, because of the lower computational cost.

Wan [114] was the first to derive a 1D cross-sectionally averaged spray model (CAS) from 3D multiphase governing equations for diesel sprays in the context of compression-ignition (CI) engines considering droplet dynamics. Recently, Deshmukh et al. [77] proposed some crucial improvements to the original CAS model by incorporating an additional vapor transport equation and state-of-the-art droplet breakup and evaporation models and found that the CAS model is able to predict the trend in inert subcooled spray characteristics reasonably well compared to the original work by Wan [114] for different fuels under a wide range of operating conditions. Although considerable efforts have been made to the development of the ROMs for subcooled sprays, studies on the 1D physics-based ROM development for macroscopic characterization of the flash-boiling sprays are still scarce in the literature. In this chapter, the CAS model developed by Deshmukh et al. [77] is further extended for the simulation of flash-boiling sprays. The extended CAS model is applied to different fuels under engine-like conditions, which are susceptible to flash-boiling. It incorporates several important physical sub-processes in flash-boiling sprays including air entrainment, drag, droplet internal as well as external vaporization, droplet heating, flash-boiling induced breakup, and aerodynamic breakup models. The proposed physics-based ROM for flash-boiling sprays is found to capture reasonable trends in spray penetration lengths for different fuels under flash-boiling conditions.

This chapter is structured as follows. Section 6.1 introduces the new extended CAS model in detail. The numerical methods and the solution procedure are briefly discussed in Section 6.2. The detailed description of the experimental cases used for model validation is presented in Section 6.3. In Section 6.4, the macroscopic spray characteristics predicted by the previous CAS model as well as the newly developed CAS model are discussed. Finally,

the findings of the present study are summarized in Section 6.6.

6.1 Models

The 3D multiphase governing equations for a complete spray [113] are reduced to 2D by assuming azimuthal symmetry and then radially integrated to obtain a one-dimensional system of equations. The reader is referred to Wan [114] for more details about the model reduction. The governing equations (GEs) for the newly developed CAS model are given by

$$\mathrm{D_g}(\bar{\rho}\hat{Y}_\mathrm{a}b^2) = \dot{\omega}_{\mathrm{ent,a}}b, \tag{6.1}$$

$$\mathrm{D_g}(\bar{\rho}\hat{Y}_\mathrm{v}b^2) = \langle\dot{\omega}_{\mathrm{vap,ext}} + \dot{\omega}_{\mathrm{vap,exp}}\rangle\, b^2, \tag{6.2}$$

$$\mathrm{D_g}((\bar{\rho}\hat{Y}_\mathrm{g}\hat{u}_\mathrm{g}b^2) = -\langle\dot{\omega}_{\mathrm{drag}}\rangle\, b^2 + \langle\dot{\omega}_{\mathrm{vap,ext}} + \dot{\omega}_{\mathrm{vap,exp}}\rangle\, \hat{u}_\mathrm{l}b^2, \tag{6.3}$$

$$\begin{aligned}\mathrm{D_g}(\bar{\rho}\hat{Y}_\mathrm{g}\hat{T}_\mathrm{g}b^2) = &-\langle\dot{\omega}_{\mathrm{heat}}\rangle\,\frac{C_\mathrm{l}}{C_{\mathrm{p,g}}}b^2 + \langle(\dot{\omega}_{\mathrm{vap,ext}} + \dot{\omega}_{\mathrm{vap,exp}})\rangle\,\frac{C_{\mathrm{p,v}}}{C_{\mathrm{p,g}}}\hat{T}_\mathrm{v}b^2 \\ &+\dot{\omega}_{\mathrm{ent,a}}\frac{C_{\mathrm{p,a}}}{C_{\mathrm{p,g}}}\hat{T}_\mathrm{a}b,\end{aligned} \tag{6.4}$$

$$\mathrm{D_l}((\bar{\rho}\hat{Y}_\mathrm{l}b^2) = -\langle\dot{\omega}_{\mathrm{vap,ext}} + \dot{\omega}_{\mathrm{vap,exp}}\rangle\, b^2, \tag{6.5}$$

$$\mathrm{D_l}((\bar{\rho}\hat{Y}_\mathrm{l}\hat{u}_\mathrm{l}b^2) = \langle\dot{\omega}_{\mathrm{drag}}\rangle\, b^2 - \langle\dot{\omega}_{\mathrm{vap,ext}} + \dot{\omega}_{\mathrm{vap,exp}}\rangle\, \hat{u}_\mathrm{l}b^2, \tag{6.6}$$

$$\mathrm{D_l}(\bar{\rho}\hat{Y}_\mathrm{l}\langle\hat{d}_\mathrm{d}\rangle b^2) = -\left\langle\frac{\dot{\omega}_{\mathrm{bre}}}{2\hat{d}_\mathrm{d}}\right\rangle b^2 - \frac{4}{3}\left\langle\dot{\omega}_{\mathrm{vap,ext}}\hat{d}_\mathrm{d}\right\rangle b^2 - \frac{2}{3}\left\langle\dot{\omega}_{\mathrm{vap,exp}}\hat{d}_\mathrm{d}\right\rangle b^2, \tag{6.7}$$

$$\mathrm{D_l}(\bar{\rho}\hat{Y}_\mathrm{l}\hat{T}_\mathrm{d}b^2) = \langle\dot{\omega}_{\mathrm{heat}}\rangle\, b^2 - \langle(\dot{\omega}_{\mathrm{vap,ext}} + \dot{\omega}_{\mathrm{vap,exp}})\rangle\,\hat{T}_\mathrm{d}b^2, \tag{6.8}$$

where ρ denotes the density, $b(z,t)$ the spray width, z the axial coordinate, t the temporal coordinate, Y the mass fraction, u the velocity, d the droplet diameter, C the specific heat capacity, C_p the specific heat capacity at constant pressure, and T the temperature. The subscripts 'd', 'l', 'g', 'a', and 'v' refer to the droplet variables, liquid phase, gas phase, ambient gas, and vapor, respectively. The radially integrated differential operator, $\mathrm{D_i}(\bar{\rho}\hat{\phi}b^2)$, is defined as

$$\mathrm{D_i}(\bar{\rho}\hat{\phi}b^2) = \frac{\partial}{\partial t}(\bar{\rho}\hat{\phi}b^2) + \frac{\partial}{\partial z}(\bar{\rho}\hat{\phi}\hat{u}_\mathrm{i}b^2) \qquad \text{with} \qquad i = \mathrm{g},\,\mathrm{l}, \tag{6.9}$$

where ϕ represents the quantity of interest. The density-weighted cross-sectional average of ϕ is defined as

$$\bar{\rho}\hat{\phi}b^2 = 2\int_0^\infty \rho\phi r\ \mathrm{d}r, \tag{6.10}$$

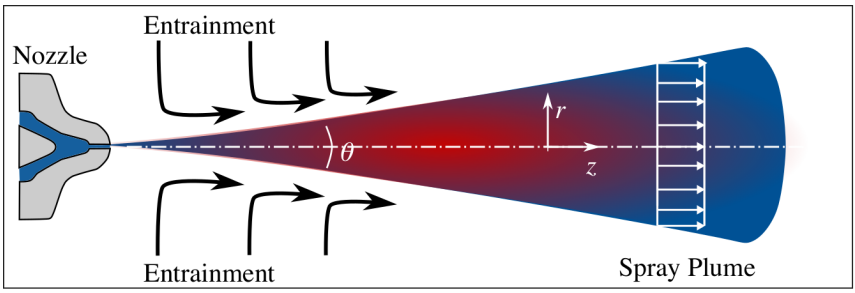

Figure 6.1: Schematic of the CAS model.

where r is the radial coordinate. The cross-sectional averaging with $\phi = 1$ and density-weighted cross-sectional averaging are denoted by the 'overline' $(\bar{\cdot})$ and 'hat' $(\hat{\cdot})$ operators, respectively. The operator, $\langle\cdot\rangle$, in the GEs represents the expectation value of any term, which is a function of droplet diameter and is defined as

$$\langle\zeta\rangle = \int \zeta(\hat{d}')\mathcal{P}(\hat{d}')\mathrm{d}\hat{d}', \tag{6.11}$$

where $\mathcal{P}(\hat{d}')$ denotes the droplet size distribution. However, due to the difficulties associated with the use of polydisperse droplet size distribution [77], the droplets are assumed to be mono-disperse in this study. A schematic of the CAS model is shown in Fig. 6.1. The source terms $(\dot{\omega}/\dot{S})$ on the right-hand side of the GEs describe different sub-models for the physical processes, such as air-entrainment $(\dot{\omega}_{\mathrm{ent,a}})$, drag $(\dot{\omega}_{\mathrm{drag}})$, heat transfer $(\dot{\omega}_{\mathrm{heat}})$, droplet breakup $(\dot{\omega}_{\mathrm{bre}})$, vaporization $(\dot{\omega}_{\mathrm{vap,ext}})$, and droplet expansion $(\dot{\omega}_{\mathrm{vap,exp}})$ in flash-boiling sprays. The details of the sub-models are discussed in the next subsections.

6.1.1 Air Entrainment Model

Air entrainment into the spray plume describes the air mass flow across the spray boundary. The spray morphology is significantly influenced by the entrained air [115]. The higher the entrainment rate, the better will be the mixing between the injected fuel and ambient air, and subsequently, the combustion performance will be improved. The air entrainment source term is modeled as

$$\dot{\omega}_{\mathrm{ent,a}} = \rho_{\mathrm{a}}\beta\hat{u}_{\mathrm{g}}, \tag{6.12}$$

where β is the spreading coefficient defined as $\beta = \tan(\theta_1/2)$. The spray cone angle, θ_1 (in degree), which was previously modeled using the Hiroyasu and Arai [113] correlation, is updated for superheated conditions with the formulation described in Eq. (5.48) in the previous chapter.

6.1.2 Drag Model

The steady-state drag force on a droplet can be expressed as [102]

$$F_{\mathrm{ss,drag}} = \frac{1}{2}\rho_{\mathrm{g}} C_{\mathrm{drag}} A_{\mathrm{d}} \left(u_{\mathrm{g}} - u_{\mathrm{l}}\right) \left|u_{\mathrm{g}} - u_{\mathrm{l}}\right|, \tag{6.13}$$

where A_{d} is the droplet surface area and C_{drag} the droplet drag coefficient computed as [116]

$$C_{\mathrm{drag}} = \begin{cases} \frac{24}{\mathrm{Re}_{\mathrm{d,sl}}}\left(1 + \frac{1}{6}{\mathrm{Re}_{\mathrm{d,sl}}}^{2/3}\right) & \text{for } \mathrm{Re}_{\mathrm{d,sl}} \leq 1000 \\ 0.424 & \text{for } \mathrm{Re}_{\mathrm{d,sl}} > 1000. \end{cases} \tag{6.14}$$

$\mathrm{Re}_{\mathrm{d,sl}}$ denotes the droplet Reynolds number and is given by

$$\mathrm{Re}_{\mathrm{d,sl}} = \rho_{\mathrm{g}} \left|u_{\mathrm{g}} - u_{\mathrm{l}}\right| \hat{d}_{\mathrm{d}} / \mu_{\mathrm{g}}, \tag{6.15}$$

where μ_{g} is the gas-phase molecular viscosity. The source term due to the steady-state drag force on a droplet of diameter $\hat{d}_{\mathrm{d}}$ is thus computed as

$$\dot{\omega}_{\mathrm{drag}} = \frac{3 C_{\mathrm{drag}} \rho_{\mathrm{g}} \bar{\rho} \hat{Y}_{\mathrm{l}} (\hat{u}_{\mathrm{g}} - \hat{u}_{\mathrm{l}}) |\hat{u}_{\mathrm{g}} - \hat{u}_{\mathrm{l}}|}{4 \rho_{\mathrm{l}} \hat{d}_{\mathrm{d}}}. \tag{6.16}$$

6.1.3 Superheated Droplet Breakup Model

Deshmukh et al. [77] modeled the droplet breakup only via aerodynamic breakup mechanism as the sub-cooled liquid droplet atomization is known to be mainly controlled by the aerodynamic forces acting on the droplet surface. However, as described in the previous chapter, the breakup process in the superheated droplets is mainly governed by the competition between micro-explosions resulting from the spontaneous bubble growth in the droplets and aerodynamic forces acting on the droplets' surface [72]. Thus, the CAS model has been integrated with a hybrid breakup model which includes both the thermal and the aerodynamic breakup mechanisms.

A liquid droplet generates multiple child droplets at the end of the breakup. However, a continuous thermal and aerodynamic breakup approach is considered in the CAS model for simplicity, which results in a continuous reduction of

the droplet diameter rather than generating multiple child droplets [77]. The source term due to the droplet breakup is expressed as $\dot{\omega}_{\mathrm{bre}} = K_{\mathrm{bre}}\bar{\rho}$, where K_{bre} is the breakup coefficient modeled either via $K_{\mathrm{bre,thm}}$ or via $K_{\mathrm{bre,aero}}$ depending on the breakup length and time scales. $K_{\mathrm{bre,thm}}$ and $K_{\mathrm{bre,aero}}$ describe the breakup coefficients resulting from the micro-explosion (herein referred to as 'thermal breakup') and aerodynamic force-induced breakup (herein referred to as 'aerodynamic breakup') mechanism, respectively. Details on the calculation of the breakup coefficients are discussed in the following subsections.

Thermal Breakup

The breakup coefficient of the thermal breakup is modeled as

$$K_{\mathrm{bre,thm}} = \frac{2\hat{d}_{\mathrm{d}}(\hat{d}_{\mathrm{d}} - d_{\mathrm{st,thm}})}{\tau_{\mathrm{b,thm}}}, \tag{6.17}$$

where $d_{\mathrm{st,thm}}$ and $\tau_{\mathrm{b,thm}}$ denote the stable droplet diameter and breakup time associated with the thermal breakup mechanism, respectively, defined as

$$\tau_{\mathrm{b,thm}} = A_0 \frac{\hat{d}_{\mathrm{d}}}{\eta_{\mathrm{thm}}\Omega_{\mathrm{thm}}} \quad \text{and} \quad d_{\mathrm{st,thm}} = A_1\eta_{\mathrm{thm}}. \tag{6.18}$$

The amplitude of the disturbance due to the bubble growth (η_{thm}) and the disturbance growth rate (Ω_{thm}) are defined as

$$\eta_{\mathrm{thm}} = \left(\frac{6\epsilon_{\mathrm{crit}}V_{\mathrm{l}}}{\pi N_{\mathrm{bub}}\left(1-\epsilon_{\mathrm{crit}}\right)}\right)^{1/3} \quad \text{and} \quad \Omega_{\mathrm{thm}} = \frac{2\dot{R}_{\mathrm{b}}}{\mathsf{D_o}}, \tag{6.19}$$

where $\dot{R}_{\mathrm{b}}$ is the bubble growth rate obtained using Rayleigh solution as

$$\dot{R}_{\mathrm{b}} = \sqrt{\frac{2}{3}\frac{P_{\mathrm{v}}\left(\hat{T}_{\mathrm{d}}\right) - P_{\mathrm{g}}}{\rho_{\mathrm{l}}}}. \tag{6.20}$$

In the CAS model, a value of 0.55 is considered for ϵ_{crit} [58]. N_{bub} represents the total number of vapor bubbles in the superheated droplet and is calculated using the empirical bubble number density proposed by Senda et al. [19], as shown in Eq. (2.1) in the previous chapter.

Aerodynamic Breakup

A combined Kelvin–Helmholtz (KH) - Rayleigh–Taylor (RT) breakup model is incorporated in the CAS model for the aerodynamic breakup. The aerodynamic breakup coefficient is expressed as

$$K_{\mathrm{bre,aero}} = \frac{2\hat{d}_{\mathrm{d}}(\hat{d}_{\mathrm{d}} - d_{\mathrm{st,aero}})}{\tau_{\mathrm{b,aero}}}. \tag{6.21}$$

The stable droplet diameter ($d_{\mathrm{st,aero}}$) is considered to be proportional to the wavelength of the fastest growing KH/RT waves. The wavelength and breakup time ($\tau_{\mathrm{b,aero}}$) associated with the aerodynamic breakup are computed either via the KH model or via the RT model. The detailed formulation of Λ and Ω corresponding to the KH-RT breakup model are already presented in the previous chapter.

The breakup is modeled via the thermal breakup mechanism if $\hat{d}_{\mathrm{d}} > d_{\mathrm{st,thm}}$ and $\tau_{\mathrm{b,thm}} < \tau_{\mathrm{b,aero}}$, otherwise, the breakup takes place via the aerodynamic breakup mechanism. The RT model is used for aerodynamic breakup if $\hat{d}_{\mathrm{d}} > d_{\mathrm{st,RT}}$ and $\tau_{\mathrm{b,RT}} < \tau_{\mathrm{b,KH}}$, else the KH model is considered. The breakup model constants, A_0, A_1, B_1, C_{RT}, and C_τ, depend on the injector nozzle geometry and therefore need to be tuned for a given injector to match the experimental liquid length [77]. It is to be noted that for a given injector, once the tuning is performed, the breakup model can be used for any fuel under any operating conditions without further tuning the model constants.

6.1.4 Superheated Droplet Vaporization Model

Deshmukh et al. [77] previously modeled evaporation using the Miller and Bellan [91] model, which is not valid for superheated droplets. As described in the previous chapters, the superheated liquid droplet phase transition occurs via the internal as well as external vaporization phenomena. The evaporation model in the CAS formulation is thus updated with the above-mentioned vaporization processes.

Internal Vaporization

The internal vaporization via the formation of vapor bubbles causes the droplet to expand in the radially outward direction in the superheated regime. The source term of droplet expansion is modeled as

$$\dot{\omega}_{\mathrm{vap,exp}} = \frac{3K_{\mathrm{vap,exp}}\bar{\rho}\hat{Y}_{\mathrm{l}}}{2\hat{d}_{\mathrm{d}}^2}, \tag{6.22}$$

where $K_{\text{vap,exp}}$ is expressed as [117]

$$K_{\text{vap,exp}} = \frac{4\hat{d}_{\text{d}}\rho_v \dot{R}_{\text{b}}}{\rho_l} N_{\text{bub}}. \tag{6.23}$$

External Vaporization

The source term for the vaporization due to the heat flux from the droplet's inner core is modeled as $\dot{\omega}_{\text{vap,ht1}} = 3K_{\text{vap,ht1}}\bar{\rho}\hat{Y}_{\text{l}}/(2\hat{d}_{\text{d}}^2)$. The flash vaporization coefficient, $K_{\text{vap,ht1}}$, is given by [25]

$$K_{\text{vap,ht1}} = \frac{4\hat{d}_{\text{d}} h_{\text{f}}(\hat{T}_{\text{d}} - T_{\text{b}})}{\rho_{\text{l}} L_{\text{v}}(T_{\text{b}})}. \tag{6.24}$$

The flashing heat transfer coefficient, h_{f} (in kW/m^{2}K), is approximated using the correlation proposed by Adachi et al. [25], as shown in Eq. (2.10). Depending on the ambient conditions, the superheated liquid droplet would either consume its own energy to vaporize (for $T_{\text{b}} > T_{\text{g}}$) or utilize the heat flux from the ambient gas for the phase transition (for $T_{\text{b}} < T_{\text{g}}$). The vaporization source term due to the temperature gradient between the droplet's external surface and the surrounding gas is modeled as $\dot{\omega}_{\text{vap,ht2}} = 3K_{\text{vap,ht2}}\bar{\rho}\hat{Y}_{\text{l}}/(2\hat{d}_{\text{d}}^2)$, where the vaporization coefficient, $K_{\text{vap,ht2}}$, is given by Adachi et al. [25]

$$K_{\text{vap,ht2}} = \frac{4\hat{d}_{\text{d}} f_3 h_{\text{ex}} |\hat{T}_{\text{g}} - \hat{T}_{\text{s}}|}{\rho_{\text{l}} L_{\text{v}}(\hat{T}_{\text{s}})}, \tag{6.25}$$

where h_{ex} represents the external heat transfer coefficient. Combining the contributions from the different external vaporization sources, such as $\dot{\omega}_{\text{vap,ht1}}$ and $\dot{\omega}_{\text{vap,ht2}}$, yields the source term due to the total external vaporization in the superheated regime as

$$\dot{\omega}_{\text{vap,ext}} = \frac{3K_{\text{vap,ext}}\bar{\rho}\hat{Y}_{\text{l}}}{2\hat{d}_{\text{d}}^2} \quad \text{with} \quad K_{\text{vap,ext}} = K_{\text{vap,ht1}} + K_{\text{vap,ht2}}. \tag{6.26}$$

When the superheated liquid droplet cools down to a temperature below T_{b}, the standard non-equilibrium evaporation model proposed by Miller and Bellan [91] is used to model the vaporization process. The vaporization coefficient in this sub-cooled regime is given by [77]

$$K_{\text{vap,ext}} = 4\frac{\rho_{\text{g}}\Gamma_{\text{v,g}}}{\rho_{\text{l}}} \ln(1 + \text{B}_{\text{M,d}})\text{Sh}_{\text{d}}, \tag{6.27}$$

where $\Gamma_{\mathrm{v,g}}$ denotes the diffusion coefficient of fuel vapor in the ambient gas mixture. For additional details on the subcooled vaporization modeling, the reader is referred to the Chapter 5. In the CAS model, the liquid properties such as density (ρ_{l}), viscosity (μ_{l}), and surface tension (σ) are assumed to be constant throughout the liquid phase and computed at the injection temperature (T_{inj}). Wilke [118] formula is used to evaluate the gas-phase mixture properties such as viscosity (μ_{g}) and thermal conductivity (λ_{g}), whereas the mixture-specific heat capacity at constant pressure ($C_{\mathrm{p,g}}$) is evaluated using the linear mixing rule [77]. All the gas-phase mixture properties and the correlations in the CAS model are computed at reference temperature (T_{ref}) obtained by the one-third rule [92]. The derivation of the vaporization coefficients are provided in Appendix H.1.

6.1.5 Gas-phase Energy Transport

Deshmukh et al. [77] calculated the gas phase temperature, $\hat{T}_{\mathrm{g}}$, by assuming a homogeneous mixture of fuel vapor and ambient gas. In the present work, a more accurate formulation has been incorporated for obtaining $\hat{T}_{\mathrm{g}}$ considering the following physical phenomena: (1) the energy dissipation/deposition due to the heat transfer between the droplets and the gas-phase denoted by $\dot{\omega}_{\mathrm{heat}}(C_{\mathrm{l}}/C_{\mathrm{p,g}})b^2$, (2) the energy transport by the vaporized fuel into the gas phase expressed as $(\dot{\omega}_{\mathrm{vap,ext}} + \dot{\omega}_{\mathrm{vap,exp}})(C_{\mathrm{p,v}}/C_{\mathrm{p,g}})\hat{T}_{\mathrm{v}}b^2$, and (3) the energy transport by the fresh ambient air into the spray plume due to the air-entrainment phenomenon given by $\dot{\omega}_{\mathrm{ent,a}}(C_{\mathrm{p,a}}/C_{\mathrm{p,g}})\hat{T}_{\mathrm{a}}b$. The fuel vapor temperature, $\hat{T}_{\mathrm{v}}$, in Eq. (6.4) is calculated based on the energy balance between the liquid and the fuel vapor as

$$\hat{T}_{\mathrm{v}} = \frac{C_{\mathrm{l}}\hat{T}_{\mathrm{d}} - L(\hat{T}_{\mathrm{s}})}{C_{\mathrm{p,v}}}. \tag{6.28}$$

6.1.6 Heat Transfer Model

The droplet bulk temperature in the CAS model was calculated using the infinite-conductivity model proposed by Miller and Bellan [91] only considering subcooled heat transfer. For the superheated droplet, the heat transfer

coefficient has been updated as

$$K_{\text{heat}} = \underbrace{\frac{6f_{2,\text{sup}}\text{Nu}_\text{d}\lambda_\text{g}(T_\text{ref})(\hat{T}_\text{g}-\hat{T}_\text{s})}{\rho_\text{l}\hat{d}_\text{d}^2 C_\text{l}(\hat{T}_\text{d})}}_{\text{conductive heat flow}} - \underbrace{\overbrace{\frac{3K_{\text{vap,ext}}L(\hat{T}_\text{s})}{2\hat{d}_\text{d}{}^2 C_\text{l}(\hat{T}_\text{d})}}^{\text{external vaporization}} - \overbrace{\frac{3K_{\text{vap,exp}}L(\hat{T}_\text{d})}{2\hat{d}_\text{d}{}^2 C_\text{l}(\hat{T}_\text{d})}}^{\text{internal vaporization}}}_{\text{evaporative cooling}}. \tag{6.29}$$

The derivation of K_{heat} is given in H.2. In Eq. (6.29), the first term on the right-hand side describes the conductive heat flow per unit time between the droplet surface and the external ambient. The second and third terms represent the evaporative cooling of the droplet due to the external and internal vaporization [25], respectively. The nondimensional superheated evaporation parameter, ξ_{sup}, determines the value of $f_{2,\text{sup}}$, as discussed in the previous chapter (see Eq. (5.26)). In the CAS model, ξ_{sup} is expressed as

$$\xi_{\text{sup}} = \left(\frac{\text{Pr}_\text{g}\hat{d}_\text{d}}{2\mu_\text{g}}\right)\left[\frac{h_\text{f}(\hat{T}_\text{d}-\hat{T}_\text{s})}{L(\hat{T}_\text{s})} + \frac{f_3 h_\text{ex}|\hat{T}_\text{g}-\hat{T}_\text{s}|}{L(\hat{T}_\text{s})}\right]. \tag{6.30}$$

For subcooled droplets, the conductive heat flow and the external vaporization are solely responsible for the change in droplet bulk temperature, and thus K_{heat} can be expressed as

$$K_{\text{heat}} = \underbrace{\frac{6f_{2,\text{sub}}\text{Nu}_\text{d}\lambda_\text{g}(T_\text{ref})(\hat{T}_\text{g}-\hat{T}_\text{s})}{\rho_\text{l}\hat{d}_\text{d}^2 C_\text{l}(\hat{T}_\text{d})}}_{\text{conductive heat flow}} - \underbrace{\overbrace{\frac{3K_{\text{vap,ext}}L(\hat{T}_\text{s})}{2\hat{d}_\text{d}{}^2 C_\text{l}(\hat{T}_\text{d})}}^{\text{external vaporization}}}_{\text{evaporative cooling}}. \tag{6.31}$$

In the subcooled regime, $\hat{T}_\text{s}$ is considered to be equal to the droplet bulk temperature $\hat{T}_\text{d}$. The value of $f_{2,\text{sub}}$ depends on the nondimensional subcooled evaporation parameter, ξ_{sub}, which is defined as [77]

$$\xi_{\text{sub}} = \frac{1}{2}\frac{\text{Pr}_\text{g}}{\text{Sc}_\text{g}}\ln(1+\text{B}_{\text{M,d}})\text{Sh}_\text{d}. \tag{6.32}$$

The source term due to heat transfer is thus modeled as

$$\dot{\omega}_{\text{heat}} = K_{\text{heat}}\bar{\rho}\hat{Y}_\text{l}. \tag{6.33}$$

6.1.7 Nozzle Exit Conditions

A blob injection model [108, 109] was incorporated by Deshmukh et al. [77] which is known to work well in the subcooled liquid injection cases. In the case of flash-boiling injection, a significant reduction in the initial droplet diameter can occur via the rapid disintegration of the liquid close to the nozzle exit itself. The CAS model has been integrated with a correlation proposed by Gemci et al. [110] to compute the initial droplet diameter ($\mathsf{D_o}$) as described in Chapter 5 by Eq. (5.46). The in-nozzle cavitation effects are also taken into account in their correlation. The nozzle exit velocity ($\mathsf{U_o}$) is computed from the Bernoulli equation considering the losses in the nozzle through the measured discharge coefficient (C_d) as [119]

$$\mathsf{U_o} = C_\mathrm{d}\sqrt{\frac{2\left(P_\mathrm{inj} - P_\mathrm{g}\right)}{\rho_\mathrm{l}}}. \tag{6.34}$$

6.2 Numerical Methodology

The hyperbolic GEs shown in Eq. (6.1)-(6.8) are non-dimensionalized using the initial droplet diameter ($\mathsf{D_o}$) as the length scale, the nozzle exit velocity ($\mathsf{U_o}$) as the velocity scale, and $\tau = \mathsf{D_o}/\mathsf{U_o}$ as the time scale. The non-dimensional GEs are then solved numerically in conservative form using the Lax-Friedrichs scheme incorporating Rusanov fluxes [120] with local wave speeds. The GEs are advanced in time using an explicit Euler scheme. The initialization of the non-dimensional variables in the GEs is performed in the 1D discretized domain with the left boundary treated as the liquid jet and the right boundary as the far-field condition. The initial and boundary conditions used in the CAS model are summarized in Table 6.1. For more details on the numerical methods and solution procedure, the reader is referred to Deshmukh et al. [77]. A Courant-Friedrichs-Lewy (CFL) number of 0.1 is used for all CAS simulations in this work. The CAS model is implemented in an in-house serial FORTRAN90 code framework.

6.3 Description of Cases for Model Validation

The newly developed CAS model results on the evaluation of flash-boiling spray characteristics are validated against the experimental measurements reported by Aleiferis and van Romunde [4] and Duronio et al. [75] for two different injector nozzles. The first is a 6-hole asymmetric injector (herein

Variable	Definition	Initial conditions	Left BC	Right BC	Bounds
Y_{l}^*	$\hat{Y}_{\mathrm{l}}$	0.0	Dirichlet 1.0	Neumann 0.0	[0.0,1.0]
Y_{v}^*	$\hat{Y}_{\mathrm{v}}$	0.0	Dirichlet 0.0	Neumann 0.0	[0.0,1.0]
Y_{a}^*	$\hat{Y}_{\mathrm{a}}$	1.0	Dirichlet 0.0	Neumann 0.0	[0.0,1.0]
ρ^*	$\bar{\rho}/\rho_{\mathrm{l}}$	$\rho_{\mathrm{a}}/\rho_{\mathrm{l}}$	Dirichlet 1.0	Neumann 0.0	[$\rho_{\mathrm{g}}/\rho_{\mathrm{l}}$,1.0]
u_{l}^*	$\hat{u}_{\mathrm{l}}/\mathsf{U_o}$	0.0	Dirichlet 1.0	Neumann 0.0	[0.0,1.0]
u_{g}^*	$\hat{u}_{\mathrm{g}}/\mathsf{U_o}$	0.0	Dirichlet 0.0	Neumann 0.0	[0.0,1.0]
$\langle d_{\mathrm{d}}^* \rangle$	$\langle \hat{d}_{\mathrm{d}} \rangle / \mathsf{D_o}$	0.0	Dirichlet 0.1-1.0	Neumann 0.0	[0.0,1.0]
T_{d}^*	$\hat{T}_{\mathrm{d}}/T_{\mathrm{inj}}$	0.0	Dirichlet 1.0	Neumann 0.0	[0.0,1.0]
T_{g}^*	$\hat{T}_{\mathrm{g}}/T_{\mathrm{inj}}$	$T_{\mathrm{amb}}/T_{\mathrm{inj}}$	Neumann 0.0	Neumann 0.0	[$T_{\mathrm{amb}}/T_{\mathrm{inj}}$,1.0]
b^*	$b/\mathsf{D_o}$	0.5	Dirichlet 0.5	Neumann 0.0	[0.5,∞)
z^*	$z/\mathsf{D_o}$	-	0.0	800.0	[0.0,800.0]
t^*	t/τ	0.0	-	-	[0.0,∞)

Table 6.1: Initial and boundary conditions used in the CAS model.

referred to as 'Aleiferis injector'), where the Shadowgraphy technique was used to visualize the spray and hence only the liquid phase was measured in their experiments [4]. Differently, Duronio et al. [75] measured both the liquid and vapor phase using Mie scattering and Schlieren techniques, respectively, for the ECN Spray G injector (8-hole asymmetric) [121]. The geometric details of both injectors are listed in Table 6.2. A detailed description of the cases selected for model validation is summarized in Table 6.3. The tuned values of the breakup model constants for different injector nozzles are shown in Table 6.4. The injection rate profiles for all the investigated cases are generated using the virtual injection rate generator provided by CMT [111].

Parameter	Symbol	Unit	Injectors	
			Aleiferis [4]	Spray G [121]
# no of holes	-	-	6	8
Orifice diameter	$\mathsf{D_{noz}}$	μm	200	165
Length to diameter ratio	$\mathsf{L_{noz}}/\mathsf{D_{noz}}$	-	1.0−1.1	1.4
Outer spray angle	θ_2	°	60	80
Discharge coefficient	C_{d}	-	0.6	0.64

Table 6.2: Geometric details of the different injector nozzles.

No ↓	Case	Injector	Fuel	P_{inj}	T_{inj}	P_g	T_g	$\Delta\theta$
Unit →	-	-	-	bar	K	bar	K	K
1	'PEN54'	Aleiferis	n-pentane	150	363.15	1.0	298.15	54
2	'PEN84'	Aleiferis	n-pentane	150	393.15	1.0	298.15	84
3	'PEN103'	Aleiferis	n-pentane	150	393.15	0.5	298.15	103
4	'ETH29'	Aleiferis	ethanol	150	363.15	0.5	298.15	29
5	'ETH42'	Aleiferis	ethanol	150	393.15	1.0	298.15	42
7	'OCT44'	Aleiferis	iso-octane	150	393.15	0.5	298.15	44
6	'G200'	Spray G	iso-octane	200	363.15	0.2	333.15	39
8	'G150'	Spray G	iso-octane	150	363.15	0.2	333.15	39
9	'G100'	Spray G	iso-octane	100	363.15	0.2	333.15	39

Table 6.3: Test cases chosen for model validation. The values of $\Delta\theta$ are given to its nearest degree. The breakup model constants are tuned for injector nozzles for cases no. 1 and 6.

Model	Constant	Present work	
Kelvin-Helmholtz	B_0		0.61
	B_1		5.0
Rayleigh-Taylor	C_{RT}		0.45
	C_τ		1.0
Thermal breakup	A_0	Aleiferis:	1.0
		Spray G:	0.5
	A_1	Aleiferis:	0.85
		Spray G:	0.75

Table 6.4: Tuned breakup model constants for Aleiferis and Spray G injectors.

6.4 Results and Discussion

In this section, first, the performance of the CAS model without the model extensions is evaluated with the experimental measurements for different fuels and operating conditions, as listed in Table 6.3. Then, the improvements in the CAS model predictions with the proposed model extensions are discussed. Since the liquid and vapor penetration lengths are considered as the most important performance metric in determining the spray characteristics [122,

123], the simulation results are compared in terms of the penetration lengths, which are calculated based on the ECN guidelines [121].

6.4.1 Results without Model Extensions

The spray penetration lengths predicted by the CAS model without the model extensions described in Section 6.1 are compared with the experimental measurements in Fig. 6.2 for different fuels and operating conditions. The detailed simulation parameters of the investigated cases are listed in Table 6.3. It is observed that the physical submodels used by Deshmukh et al. [77] are unable to reproduce the enhanced evaporation and atomization behavior of flash-boiling sprays, thus resulting in significant over-prediction in the spray penetrations for both injectors. The model even fails to capture the trends in spray characteristics for n-pentane and ethanol fuels. Fig. 6.2a depicts that for n-pentane fuel, the predicted penetration length increases with increasing superheating degree from $\Delta\theta = 84$ K (case 'PEN84') to 103 K (case 'PEN103'), whereas a decreasing trend was observed in the experiments. A similar increasing trend is also predicted for ethanol with increasing $\Delta\theta$ from 29 K (case 'ETH29') to 42 K (case 'ETH42'), which is in contradiction with the experimental measurements. These emphasize the importance of the model extension for accurately predicting the spray characteristics under flash-boiling conditions.

6.4.2 Results with Model Extensions

This section discusses the gradual enhancements made in the previous CAS model performance, highlighting the inclusion or substitution of the new sub-models, as described in Section 6.1.

Spray Cone Angle and Initial Droplet Size Models

Flash-boiling sprays are characterized by a widening of the spray plume due to the increased radial expansion resulting from the bubble growth and micro-explosion [18]. Thus, accurate predictions of the spray cone angle as well as the initial droplet diameter plays a crucial role in determining the global spray characteristics. Fig. 6.3 shows the CAS model performance with the upgraded models for spray cone angle (Eq. (5.48)) and initial droplet size (Eq. (5.46)) in comparison with the previous version during flash-boiling conditions. Here, the droplet heat transfer and vaporization processes are modeled via the standard Miller and Bellan model. For the droplet breakup, only KH–RT

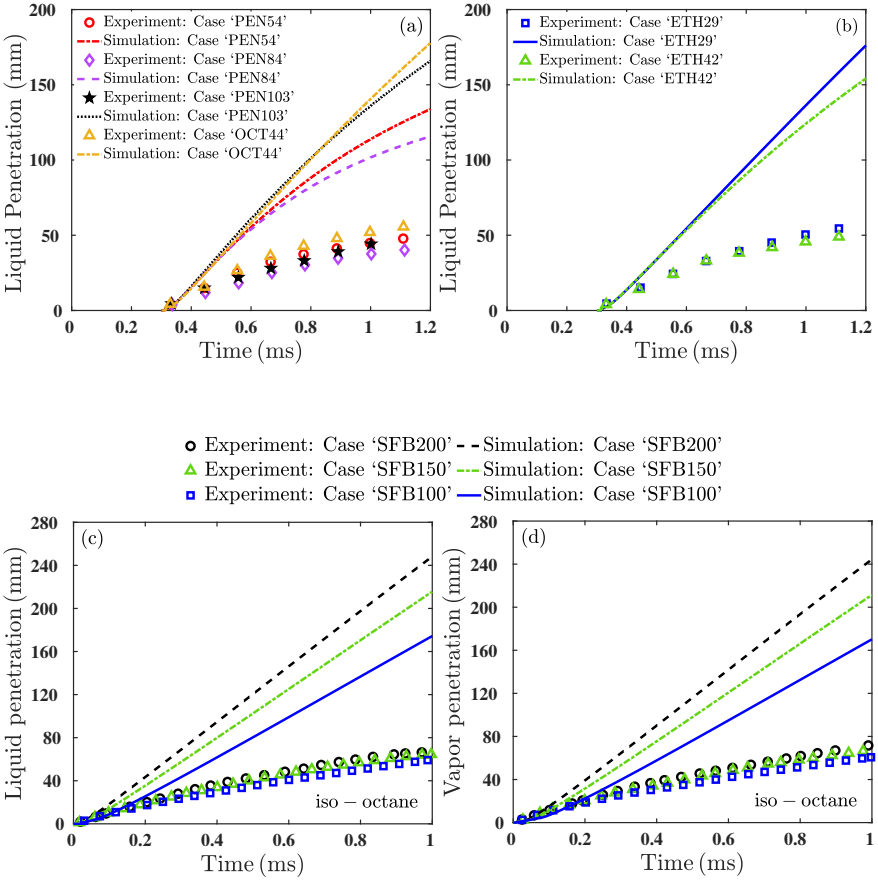

Figure 6.2: Comparison of the spray characteristics predicted by the CAS model without the model extensions and the experiments. Subfigures (a) & (b) show the comparison of liquid penetration lengths for the Aleiferis injector [4] under different operating conditions for three different fuels, whereas subfigures (c) & (d) illustrate the comparison of liquid and vapor penetration lengths of iso-octane fuel, respectively, at different injection pressures for the ECN spray G injector.

breakup model is incorporated. The gas phase temperature is obtained via the approach considered by Deshmukh et al. [77]. It is observed from Fig. 6.3

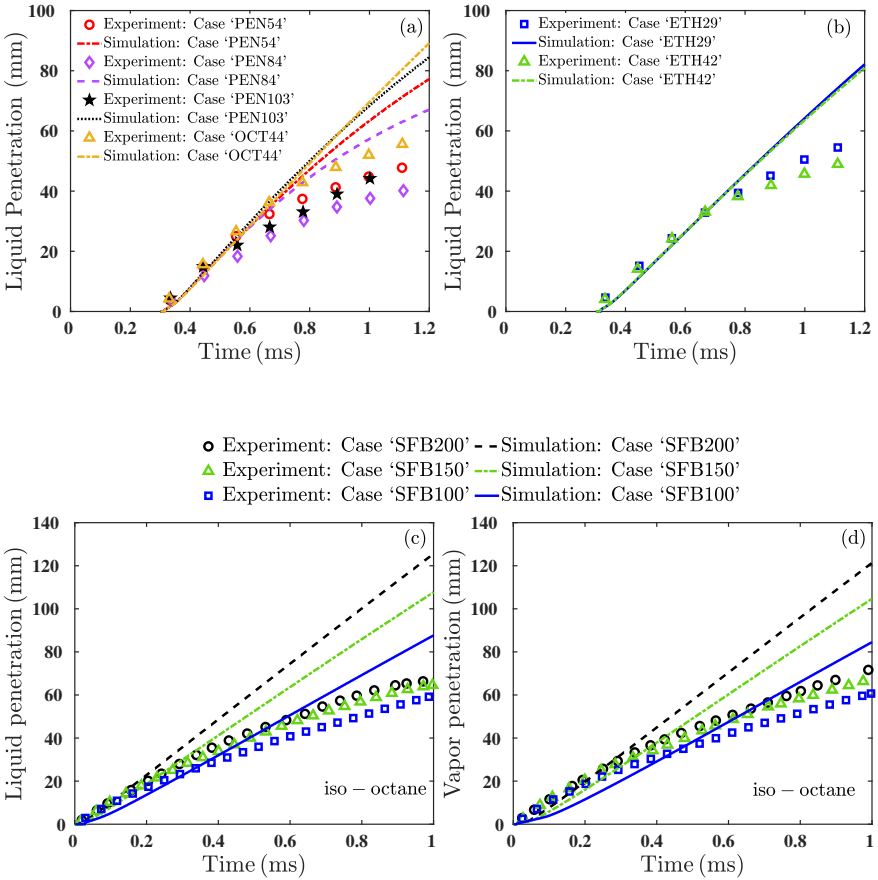

Figure 6.3: Spray characteristics predicted by the CAS model with updated spray cone angle (Eq. (5.48)) and initial droplet size (Eq. (5.46)) models. Subfigures (a) & (b) describe the comparison of liquid penetration lengths for the Aleiferis injector [4] under different operating conditions for three different fuels, whereas subfigures (c) & (d) illustrate the comparison of liquid and vapor penetration lengths of iso-octane fuel, respectively, at different injection pressures for the ECN spray G injector.

that the predictive capabilities of the CAS model are significantly improved with the updated cone angle and initial droplet diameter models compared to the previous version. However, quantitatively, the penetration lengths are still overpredicted compared to the experimental measurements.

Superheated Droplet Vaporization, Heat Transfer, and Breakup Models

This section concludes the extension of the CAS model with the upgrade of the standard evaporation, heat transfer, and breakup models to that of the superheated vaporization, heat transfer, and hybrid aerodynamic-thermal breakup models, as described in Section 6.1. Here, Eq. (6.4) is incorporated for the calculation of the gas phase temperature. The improvements in the spray characteristics obtained from the fully updated CAS model are shown in Fig. 6.4 for different fuels under varying superheating degrees for the Aleiferis injector. Fig. 6.4a shows that the predicted spray penetration decreases with increasing T_{inj}, from 363.15 K (case 'PEN54') to 393.15 K (case 'PEN84'), at constant $P_{\mathrm{g}} = 1.0$ bar for n-pentane fuel, as observed in the experiments. The increase in T_{inj} leads to an increase in liquid superheating degree ($\Delta\theta$) for the case 'PEN84', thus enhancing the evaporation rate and thermally induced breakup [5], which in turn produces the smaller droplets. These droplets then substantially decelerate due to the aerodynamic drag forces of the ambient gas, resulting in shorter spray penetrations. A similar trend is observed for flash-boiling ethanol (case 'ETH29' and 'ETH42'), as illustrated in Fig. 6.4b.

With the system pressure P_{g}, decreasing from 1.0 bar (case 'PEN84') to 0.5 bar (case 'PEN103'), at $T_{\mathrm{inj}} = 393.15$ K for n-pentane fuel, Fig. 6.4a shows that the predicted penetration length increases, as also reported in the experimental findings by Aleiferis and van Romunde [4]. Table 6.3 shows that decreasing the system pressure for these n-pentane test cases leads to an increase in $\Delta\theta$ from 84 K to 103 K. The reason behind this phenomenon is the lower saturation temperature of the liquid under reduced pressure conditions. As described above, the liquid at higher $\Delta\theta$ is associated with increased evaporation and enhanced atomization effects, thus expected to result in smaller spray droplets and eventually shorter spray penetrations compared to the case with lower $\Delta\theta$. However, the resulting opposite trend in penetrations for these n-pentane test cases can be attributed to the lower system pressures. By lowering the pressures, the reduced aerodynamic drag forces are likely to outweigh the enhanced evaporation and atomization effects at high $\Delta\theta$, leading to an increase in penetration lengths. The predicted penetration length for iso-octane fuel at $\Delta\theta = 44$ K (case 'OCT44') also agrees well with the experiment, as shown in Fig. 6.4a. Overall, the present CAS

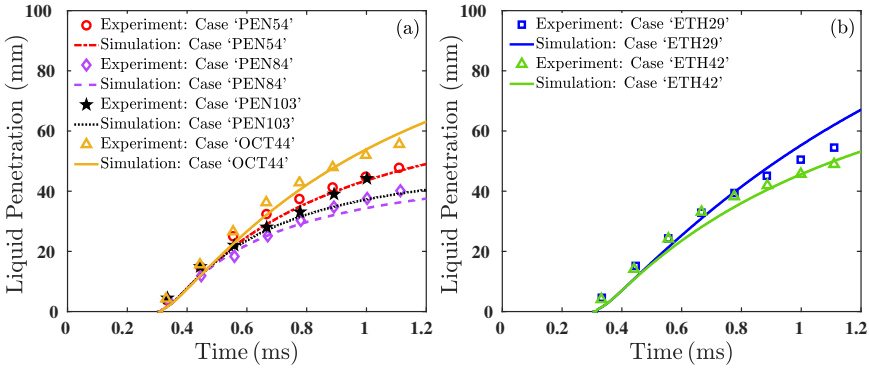

Figure 6.4: Spray characteristics predicted by the upgraded CAS model. Subfigures (a) & (b) describe the comparison of liquid penetration lengths for the Aleiferis injector [4] for different fuels and operating conditions, as listed in Table 6.3.

model is able to predict the trends in macroscopic spray characteristics similar to the experiments for different fuel properties and operating conditions for a given injector.

Fig. 6.5 depicts the improved spray characteristics of the ECN spray G injector for varying injection pressures at a constant R_p of 0.26. The decreasing injection pressure leads to a reduction in the mass flow rate and subsequently, the residence time within the nozzle hole will be increased. Due to the longer residence time, the vapor bubbles start nucleating inside the injector nozzle leading to the formation of a well-atomized spray with a shorter penetration length. It is observed that the extended CAS model is able to predict the decreasing trend of spray penetrations with decreasing injection pressures, as also observed in the experiments.

However, quantitatively, for some test cases, the present CAS model still over- and/or under-predicts the penetration lengths for both injectors. Although this is expected due to the averaged approach of the CAS model, the use of more accurate models for calculating the spray cone angle and initial droplet diameter is expected to improve the prediction towards the experiments vastly. This is because the increased radial expansion resulting from the bubble growth and micro-explosion would widen the spray plume as well as reduce initial droplet sizes under flash-boiling conditions [18]. For a multi-hole injector, the wider spray plumes emerging from different injector

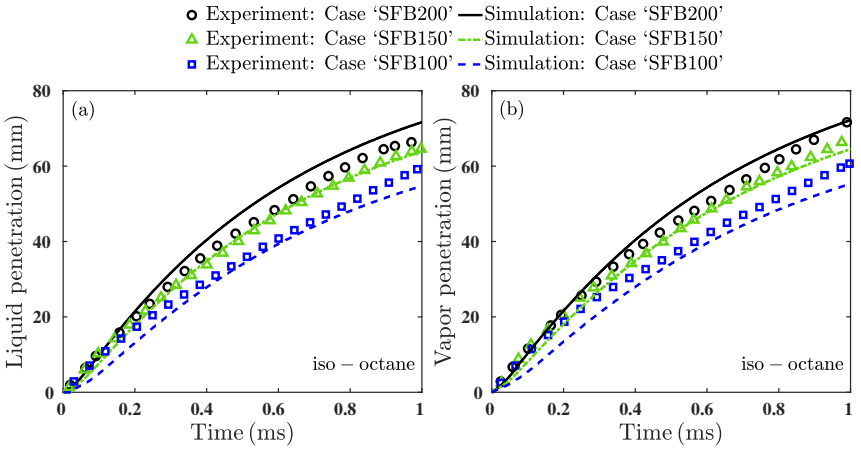

Figure 6.5: Spray characteristics predicted by the upgraded CAS model. Subfigures (a) & (b) illustrate the comparison of liquid and vapor penetration lengths of iso-octane fuel, respectively, for the ECN spray G injector at different injection pressures, as listed in Table 6.3.

holes could easily merge with each other depending on the inter-spacing and directions of the holes, thus resulting in even higher total plume widening compared to a single-hole injector. The present CAS model would not be able to capture the shattering of the child droplets due to micro-explosion and subsequent widening of the spray plume and reduced droplet sizes because of the continuous breakup approach considered. Thus, the spray cone angle and the initial droplet size models used in this study play a crucial role to mimic the above-mentioned phenomena. The influence of θ_1 and $\mathsf{D_o}$ on the penetration length is illustrated in Fig. 6.6a and Fig. 6.6b for un-collapsed (case 'ETH-29') and collapsed (case 'PEN103') sprays, respectively. It can be seen that the reduced initial droplet size and higher spray cone angle improve the quantitative prediction of liquid penetration for the un-collapsed spray, whereas the increased droplet diameter associated with higher spray cone angle provide a more reasonable prediction of the liquid penetration length for the fully collapsed spray.

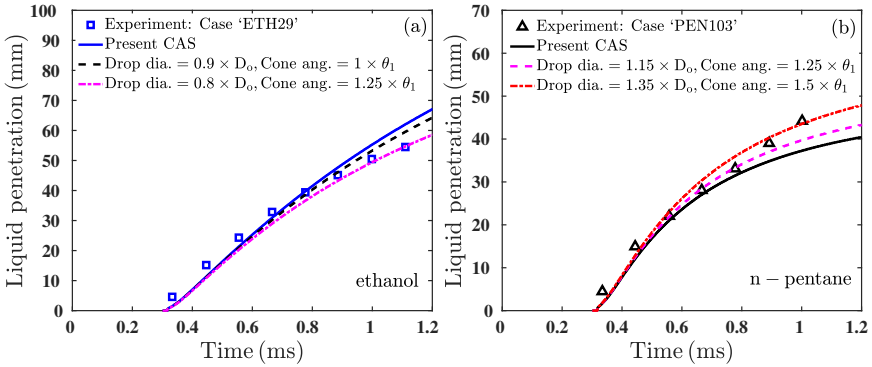

Figure 6.6: Influence of the spray cone angle and initial droplet diameter on the liquid penetration for (a) un-collapsed and (b) collapsed sprays of ethanol and n-pentane fuels, respectively.

6.5 Computational Cost

A posteriori computational cost analysis is performed for case 'PEN54' to investigate the cost reduction factor associated with using the CAS model in comparison to the 3D simulation. Both the 1D and 3D simulations were run on machines that use the Intel Broadwell processor architecture. The 3D LES was run on 480 cores for $\approx$ 3.5 h leading to a total of 1680 CPUh. The 1D CAS was run on the same machine on 1 core for $\approx$ 205 s resulting in a total of 0.057 CPUh. Thus, the CAS model is faster by up to 4 orders of magnitude compared to the 3D LES while providing reasonable predictions in flash-boiling spray characteristics such as liquid and vapor penetration lengths for different operating conditions and fuels.

6.6 Conclusions

In this study, the previously developed CAS model was first applied to predict the spray characteristics such as penetration lengths for different fuels under flash-boiling conditions. It was found that the CAS model fails to reproduce the trend in the flash-boiling spray penetration lengths. An extension of the CAS model was then proposed to improve its predictive capabilities for the simulation of flash-boiling sprays. The important physical subprocesses in flash-boiling sprays such as internal vaporization, external vaporization, and

thermally driven breakup were incorporated in the newly developed CAS model. The upgraded CAS model performance was then compared with the experimental measurements of two different injector nozzles for varying injection pressures and superheating degrees. It was found that the trends in liquid and vapor penetration lengths predicted by the updated CAS model agree well with the experiments. Though in some cases, the penetration lengths were found to be under-and/or over-predicted due to the averaged approach of the CAS model, it was shown that the prediction could be improved with the more accurate modeling of the spray cone angle and initial droplet diameter. A 3D LES of a flash-boiling spray was also performed in order to assess the computational efficiency of the CAS model. The 1D CAS model was shown to be faster by up to four orders of magnitude in comparison to the 3D LES, thus making it really useful in many practical applications related to flash-boiling including but not limited to the design of experiments, rapid fuel-screening, and creating digital twins.

7 Concluding Remarks

Due to its superior spray atomization characteristics, the flash-boiling injection technique can play a major role in improving the combustion characteristics of DISI engines. It has already shown a great potential in overcoming the crucial drawbacks associated with the DISI engines such as irregular combustion behavior due to spray impingement in the cylinder liner/piston head, formation of soot and unburnt hydrocarbons. In addition, the use of e-fuels in DISI engines, which are produced from renewable electricity and carbon sources, also has a huge potential in reducing the GHG and pollutant emissions. Compared to conventional fuels, such fuels can have very different thermophysical properties depending on their molecular structure. Particularly, fuels with high vapor pressures are highly susceptible to flash boiling depending on boundary conditions. Thus, it is necessary to improve the understanding associated with this complex injection strategy in detail at a microscopic level such that the macroscopic spray characteristics can be accurately quantified.

This dissertation, on the one hand, focused on the investigation of the microscopic processes of flash-boiling phenomena and developing improved subgrid-scale models using reduced-order modeling approaches, and subsequently applying them into large-scale 3D LPT spray simulations, and on the other hand, on the model order reduction of the flash-boiling spray from 3D to 1D to create affordable computational simulations of this intricate higher-order phenomena in numerous practical applications including but not limited to design of experiments, system simulations, creating digital twins, and rapid fuel screening.

First, a reduced-order single droplet flash-boiling model was presented in Chapter 2 utilizing an LPT framework to evaluate the influence of internal bubble dynamics, and the relative significance of internal and external vaporization processes in the overall flash vaporization of droplets. The experimental data of superheated water available in the literature was used to validate the proposed model. The present model demonstrated a reasonable agreement with the experimental results in terms of the predicted bubble radii. The flash-boiling behavior of high volatility e-fuels such as OME_x was investigated at various sub-atmospheric operating conditions. It was found that the thermal diffusion does not exert any influence on the growth of bubbles in the moderate to high superheating degree cases, a finding that

has not been previously reported. It was observed that increasing the degree of superheat at constant pressure causes a significant decrease in the time until the droplet bursts. The effects of the molecular structure of different fuel candidates was also studied for OME_x fuels with varying chain lengths. A significant difference in bubble growth characteristics was observed as the chain length was increased from x = 0 to 4. DME droplets of molecules with no $-CH_2O-$, were found to burst at a faster rate compared to the other molecules. Moreover, it was concluded that the internal vaporization via the formation and subsequent growth of the vapor bubbles is mainly responsible for driving the vaporization process in the superheated regime.

Next, a novel ROM for bubble growth considering bubble interactions and finite droplet-size effects was proposed in Chapter 3. This model was validated with the multibubble DNS results available in the literature for superheated LOx jets. The present reduced-order bubble-growth model was shown to capture the trend in considerably smaller volumetric droplet expansion relative to the single isolated bubble case. The dynamics of the vapor bubbles in OME_1 fuel droplets was studied with this newly derived bubble growth model highlighting the influence of bubble interactions on the bubble growth characteristics. The vapor bubbles were found to expand at a much slower rate while considering the bubble interactions due to the additional inertia forces induced by the surrounding vapor bubbles. The onset of droplet bursting was also found to decrease due to bubble interactions.

After that, in the Chapter 4, the limitations associated with the numerical solver of the proposed bubble growth model was outlined. It was shown that the accurate prediction of the bubble growth dynamics requires an extremely small time-step size depending on the operating conditions. The use of larger time-step size was found to result in unrealistic bubble growth behavior. An approximate semi-analytical solution for the bubble growth rate was then derived based on the dimensional analysis of the RPE, which was found to provide reasonable predictions of the bubble evolution with small computational expenses compared to the numerical solver.

This novel bubble growth model is then applied to simulate the large-scale spray for flash-boiling condition using LES in Chapter 5. A two way coupled LPT approach was incorporated for the spray simulation. The liquid spray penetration length and steady-state SMD obtained from the LES were shown to have good agreement with the experimental measurements. The impact of the newly integrated flash-boiling model on the simulation results was also discussed in terms of the macroscopic spray characteristics.

In Chapter 6, a novel reduced-order flash-boiling spray model termed

CAS was developed to reduce the computational cost of the 3D LPT spray simulations even further such that this 1D model can be easily employed for simulations of many practical applications which requires cost-effective computational representations of this complex higher-order injection phenomena. The inclusion of droplet diameter and cone angle prediction models, a superheated vaporization model, and a breakup model was found to significantly improve the CAS model performance during the flash-boiling injection conditions. The reduction in computational time with the new CAS model when simulating the flash-boiling spray was highlighted. The CAS model demonstrated a speedup of up to four orders of magnitude compared to the 3D LES, thus making them highly valuable for various applications related to flash-boiling.

Appendices

A Justification of Neglecting the Liquid Viscosity

In Fig. A.1, the comparison of various pressure forces is shown for OME_1 droplet at $P_g = 0.3$ bar. The pressure due to viscous force, P_μ, is found to remain negligible compared to the other pressure terms throughout the bubbles' lifetime. Similar findings are observed for the other operating conditions considered in this study, thus, justifying the neglection of the influence of viscosity in the original Rayleigh-Plesset equation, as shown in Chapter 2. In the case of DME and OME_4, P_μ is also found to exhibit similar behavior. The results are not included here for the sake of brevity.

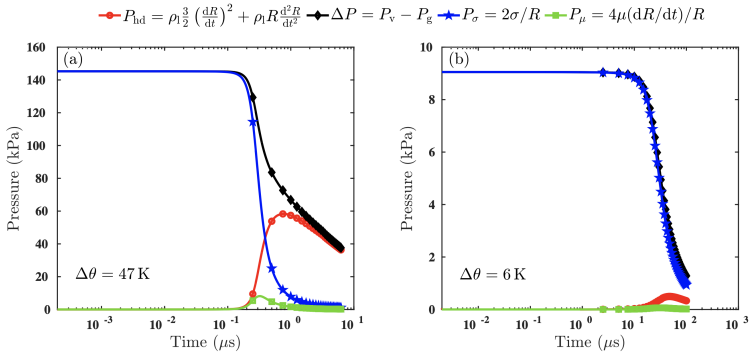

Figure A.1: The dependency of the rate of change of ΔP on the hydrodynamic pressure for the OME_1 droplet at $T_g = 323$ K, $P_g = 0.3$ bar with different superheating degrees, (a) $\Delta\theta = 47$ K and (b) $\Delta\theta = 6$ K.

B Comparison of the Theoretically Predicted Thermophysical Properties with the Measured One

Figs. B.1, B.2, and B.3 show the comparison of the theoretical prediction of the thermophysical properties with those calculated from the polynomial fitted with experimental measurements [95, 97] for DME, OME_1, and OME_4, respectively. Whereas for the theoretical prediction of surface tension, perturbed chain polar - statistical associating fluid theory (PCP-SAFT) was used, other properties were predicted using group contribution methods (GCM) [124, 125] as well as molecular transport calculations [126]. To compute the surface tension of the fuel, here, PCP-SAFT equation of state was combined with classical density functional theory [127, 128]. The fuel-specific interaction parameters required for PCP-SAFT modeling are usually determined from experimental data. In this study, these parameters were estimated from molecular properties computed by quantum chemical calculations [129, 130] and refitted to the normal boiling point from the experimental data. It is observed that the properties calculated from the polynomial fitted with experimental measurements agree with the trends of the theoretical prediction reasonably well even beyond its limit, in which extrapolation was performed. However, it is to be noted that the difference between extrapolated and predicted properties will not have any qualitative impact on the conclusions drawn in this dissertation.

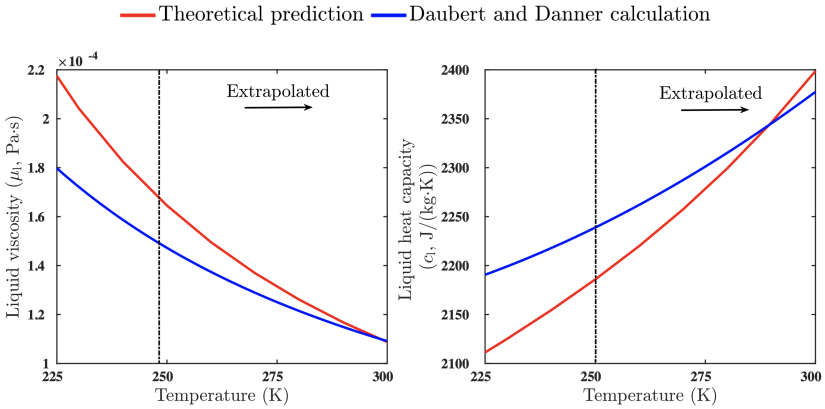

Figure B.1: Comparison of the temperature variation of the theoretically predicted thermophysical properties with the one obtained from Daubert and Danner [95] for DME.

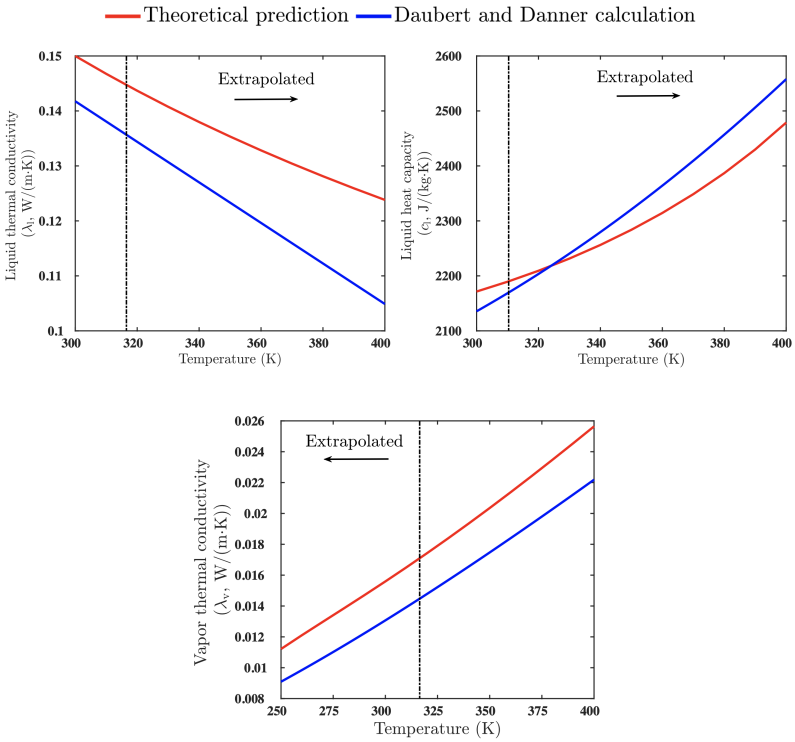

Figure B.2: Comparison of the temperature variation of the theoretically predicted thermophysical properties with the one obtained from Daubert and Danner [95] for OME_1.

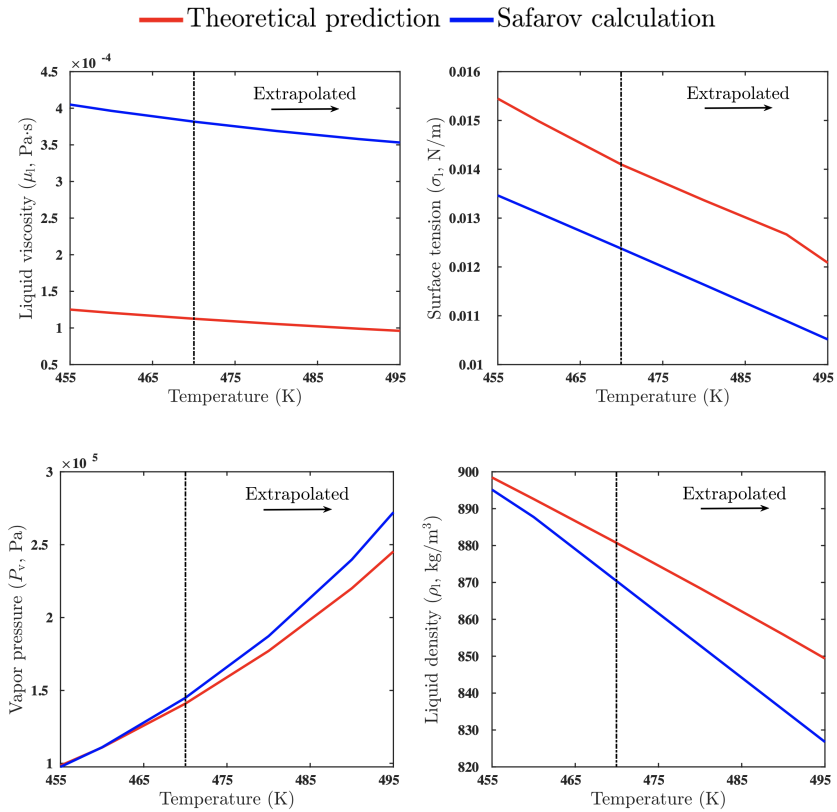

Figure B.3: Comparison of the temperature variation of the theoretically predicted thermophysical properties with the one calculated from the polynomial fitted with the experimental measurements by Safarov *et al.*[97] for OME_4.

C Derivation of the Pressure Force due to Bubble Interactions

Let us consider a spherically symmetric superheated microdroplet containing multiple bubbles. The pressure force, P_{inter}, induced by the i-th bubble on the target bubble, located at the center of the droplet can be obtained by solving the continuity and momentum equations for an inviscid incompressible liquid flow [61]. The one-dimensional momentum and continuity equations in spherical coordinates are given by:

$$\frac{\partial u_{\text{l}}}{\partial t} + u_{\text{l}} \frac{\partial u_{\text{l}}}{\partial r} = -\frac{1}{\rho_{\text{l}}} \frac{\partial P_{\text{inter}}}{\partial r}, \tag{C.1}$$

$$\frac{\partial}{\partial r} \left(u_{\text{l}} r^2 \right) = 0, \tag{C.2}$$

where $u_{\text{l}}(r,t)$ describes the velocity in the liquid phase relative to the interface, r denotes the radial coordinate with the origin at the droplet center, and t is the time. Integrating the continuity equation (Eq. (C.2)) in radial direction yields

$$u_{\text{l}}(r,t) = \frac{F(t)}{r^2}. \tag{C.3}$$

$F(t)$ can be obtained by prescribing the kinematic boundary condition at the bubble surface.

The vapor mass flow rate for a single bubble can be computed as

$$\dot{m}_{\text{b}} = 4\pi R_{\text{b}}^2 \rho_v \frac{\mathrm{d}R_{\text{b}}}{\mathrm{d}t} + \frac{4}{3}\pi R_{\text{b}}^3 \frac{\mathrm{d}\rho_v}{\mathrm{d}t}, \tag{C.4}$$

where ρ_{v} is the saturated vapor density at T_{v}. Neglecting the second term on the right hand side of Eq. (C.4), as it can be shown to be very small compared to the first term, $\dot{m}_b$ can be expressed as [89]

$$\dot{m}_{\text{b}} = 4\pi R_{\text{b}}^2 \rho_v \frac{\mathrm{d}R_{\text{b}}}{\mathrm{d}t}. \tag{C.5}$$

Equating Eq. (C.5) with the inward liquid mass flux yields

$$\rho_{\mathrm{l}} u_{\mathrm{l,a}} = \rho_{\mathrm{v}} \frac{\mathrm{d}R_{\mathrm{b}}}{\mathrm{d}t}, \tag{C.6}$$

$$u_{\mathrm{l,a}} = \frac{\rho_{\mathrm{v}}}{\rho_{\mathrm{l}}} \frac{\mathrm{d}R_{\mathrm{b}}}{\mathrm{d}t}, \tag{C.7}$$

where subscript 'a' represents absolute quantity and ρ_{l} the saturated liquid density at T_{v}. Thus, the relative velocity of the liquid across the interface ($r = R_{\mathrm{b}}$),

$$u_{\mathrm{l}}(R_{\mathrm{b}}, t) = \frac{\mathrm{d}R_{\mathrm{b}}}{\mathrm{d}t} - \frac{\rho_{\mathrm{v}}\left(T_{\mathrm{v}}\right)}{\rho_{\mathrm{l}}} \frac{\mathrm{d}R_{\mathrm{b}}}{\mathrm{d}t} = \left[1 - \frac{\rho_{\mathrm{v}}\left(T_{\mathrm{v}}\right)}{\rho_{\mathrm{l}}}\right] \frac{\mathrm{d}R_{\mathrm{b}}}{\mathrm{d}t}. \tag{C.8}$$

Substituting Eq. (C.8) into Eq. (C.3), $F(t)$ at the liquid/vapor interface can be obtained as

$$F(t) = \left[1 - \frac{\rho_v\left(T_{\mathrm{v}}\right)}{\rho_{\mathrm{l}}}\right] R_{\mathrm{b}}^2 \frac{\mathrm{d}R_{\mathrm{b}}}{\mathrm{d}t}. \tag{C.9}$$

Assuming $\rho_{\mathrm{v}} \ll \rho_{\mathrm{l}}$, Eq. (C.9) becomes

$$F(t) = R_{\mathrm{b}}^2 \frac{\mathrm{d}R_{\mathrm{b}}}{\mathrm{d}t}. \tag{C.10}$$

Substituting $F(t)$ into Eq. (C.3) yields,

$$u(r, t) = \frac{R_{\mathrm{b}}^2}{r^2} \frac{\mathrm{d}R_{\mathrm{b}}}{\mathrm{d}t}. \tag{C.11}$$

Replacing $u(r, t)$ in Eq. (C.3) with Eq. (C.11) yields

$$\frac{\partial}{\partial t}\left(\frac{R_{\mathrm{b}}^2}{r^2} \frac{\mathrm{d}R_{\mathrm{b}}}{\mathrm{d}t}\right) + \left(\frac{R_{\mathrm{b}}^2}{r^2} \frac{\mathrm{d}R_{\mathrm{b}}}{\mathrm{d}t}\right) \frac{\partial}{\partial r}\left(\frac{R_{\mathrm{b}}^2}{r^2} \frac{\mathrm{d}R_{\mathrm{b}}}{\mathrm{d}t}\right) = -\frac{1}{\rho_{\mathrm{l}}} \frac{\partial P_{\mathrm{inter}}}{\partial r}. \tag{C.12}$$

Assuming $P_{\mathrm{inter}}(r \to \infty, t) = 0$ and integrating Eq. (C.12) along r, P_{inter} can be expressed as

$$P_{\mathrm{inter}} = \frac{\rho_{\mathrm{l}}}{r} \frac{\mathrm{d}}{\mathrm{d}t}\left(R_{\mathrm{b}}^2 \frac{\mathrm{d}R_{\mathrm{b}}}{\mathrm{d}t}\right) + O\left(\frac{1}{r^4}\right). \tag{C.13}$$

Neglecting the higher order term in Eq. (C.13) and summing over multiple bubbles, P_{inter} finally becomes

$$P_{\mathrm{inter}} = \rho_{\mathrm{l}} \frac{\mathrm{d}}{\mathrm{d}t}\left(\sum \frac{R_{\mathrm{b}}^2}{r_i} \frac{\mathrm{d}R_{\mathrm{b}}}{\mathrm{d}t}\right). \tag{C.14}$$

D Limitations of Numerical Solver for DME

The numerical issue with the time-step size is also demonstrated using another highly volatile cryogenic e-fuel microdroplets of DME in Fig. D.1 for $\Delta\theta = 150$ K (Case 'DM-150'), $\Delta\theta = 100$ K (Case 'DM-100'), and $\Delta\theta = 80$ K (Case 'DM-80'), with bubble-bubble interactions. The simulation parameters are listed in Table D.1. As described for OME_1 microdroplets, the smaller time-step size is also required for the accurate prediction of vapor bubble growth in DME microdroplets. For a very high superheating degree of $\Delta\theta = 150$ K, the time-step size needs to be further reduced to the order of picoseconds $\left(\mathcal{O}\left(10^{-12}\,\mathrm{s}\right)\right)$ to avoid unphysical prediction of bubble growth and vapor temperature.

Case	$P_\mathrm{l}\,(\mathrm{bar})$	$T_\mathrm{d}\,(\mathrm{K})$	$\Delta\theta\,(\mathrm{K})$
DM-150	0.3	373.58	150
DM-100	0.7	340.2	100
DM-80	0.9	325.68	80

Table D.1: Simulation test cases of superheated DME microdroplets for illustrating the limitations of the numerical solver.

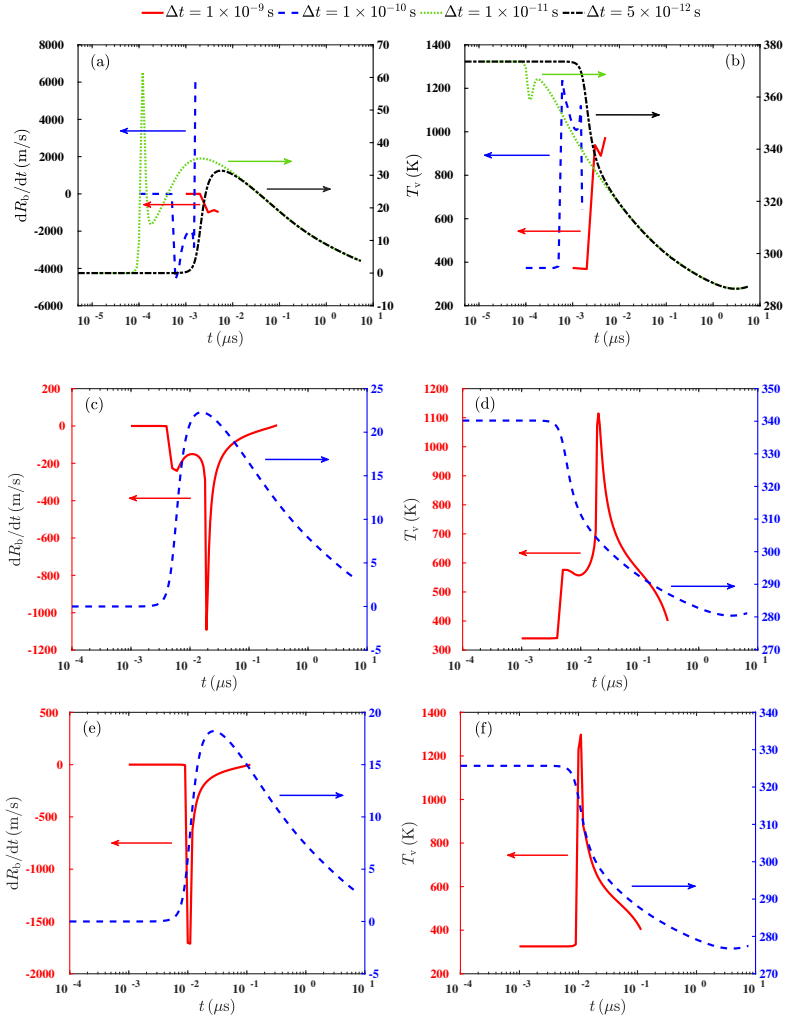

Figure D.1: Bubble growth rate (left column) and vapor temperature (right column) variation for DME microdroplets under various operating conditions and time-step sizes considering the bubble-bubble interactions. Subfigures (a) & (b), (c) & (d), and (e) & (f) depict the cases 'DM-150', 'DM-100', and 'DM-80', respectively.

E Derivation of Nondimensional RPE

The RPE for an isolated spherically symmetric vapor bubble in a homogeneous infinite liquid medium is given by

$$P_{\mathrm{v}} - P_{\mathrm{g}} = \rho_{\mathrm{l}} \left[R_{\mathrm{b}} \frac{\mathrm{d}^2 R_{\mathrm{b}}}{\mathrm{d}t^2} + \frac{3}{2} \left(\frac{\mathrm{d}R_{\mathrm{b}}}{\mathrm{d}t} \right)^2 \right] + \frac{4\mu_{\mathrm{l}}}{R_{\mathrm{b}}} \frac{\mathrm{d}R_{\mathrm{b}}}{\mathrm{d}t} + \frac{2\sigma}{R_{\mathrm{b}}}. \tag{E.1}$$

The modified RPE for spherically symmetric vapor bubble in a single droplet of radius R_{d} considering bubble-bubble interactions is given by

$$\begin{aligned} P_{\mathrm{v}} - P_{\mathrm{g}} = \rho_{\mathrm{l}} \Bigg[R_{\mathrm{b}} \left(1 + 2\pi R_{\mathrm{d}}^2 n R_{\mathrm{b}} \right) \frac{\mathrm{d}^2 R_{\mathrm{b}}}{\mathrm{d}t^2} + \left(\frac{3}{2} + 4\pi R_{\mathrm{d}}^2 n R_{\mathrm{b}} \right) \left(\frac{\mathrm{d}R_{\mathrm{b}}}{\mathrm{d}t} \right)^2 \Bigg] \\ + \frac{4\mu_{\mathrm{l}}}{R_{\mathrm{b}}} \frac{\mathrm{d}R_{\mathrm{b}}}{\mathrm{d}t} + 4\pi n \rho_{\mathrm{l}} R_{\mathrm{d}} R_{\mathrm{b}}^2 \left(\frac{\mathrm{d}R_{\mathrm{d}}}{\mathrm{d}t} \right) \left(\frac{\mathrm{d}R_{\mathrm{b}}}{\mathrm{d}t} \right) + \frac{2\sigma}{R_{\mathrm{b}}}. \end{aligned} \tag{E.2}$$

Substituting the following relationships

$$\begin{aligned} R_{\mathrm{b}}^+ = \frac{R_{\mathrm{b}}}{R_{\mathrm{c}}}, \quad \dot{R_{\mathrm{b}}^+} = \frac{\dot{R}_{\mathrm{b}}}{A}, \quad t^+ = \frac{t}{\tau}, \quad R_{\mathrm{d}}^+ = \frac{R_{\mathrm{d}}}{R_{\mathrm{c}}}, \quad n^+ = n R_{\mathrm{c}}^3; \\ \rho_{\mathrm{l}}^+ = \frac{\rho_{\mathrm{l}}}{\rho_{\mathrm{l}0}}, \quad P^+ = \frac{P}{\rho_{\mathrm{l}0} A^2}, \quad \sigma^+ = \frac{\sigma}{\sigma_0}, \quad \mu_{\mathrm{l}}^+ = \frac{\mu_{\mathrm{l}}}{\mu_{\mathrm{l}0}}, \end{aligned} \tag{E.3}$$

into Eq. (E.1) yields,

$$\begin{aligned} \left(P_{\mathrm{v}}^+ - P_{\mathrm{g}}^+ \right) \rho_{\mathrm{l}0} A^2 = \rho_{\mathrm{l}}^+ R_{\mathrm{b}}^+ \rho_{\mathrm{l}0} A^2 \frac{\mathrm{d}^2 R_{\mathrm{b}}^+}{\mathrm{d}t^{+2}} + \rho_{\mathrm{l}}^+ \rho_{\mathrm{l}0} A^2 \frac{3}{2} \left(\frac{\mathrm{d}R_{\mathrm{b}}^+}{\mathrm{d}t^+} \right)^2 + \frac{4\mu_{\mathrm{l}}^+ \mu_{\mathrm{l}0} A}{R_{\mathrm{b}}^+ R_{\mathrm{c}}} \frac{\mathrm{d}R_{\mathrm{b}}^+}{\mathrm{d}t^+} \\ + \frac{2\sigma^+ \sigma_0}{R_{\mathrm{b}}^+ R_{\mathrm{c}}}. \end{aligned} \tag{E.4}$$

Dividing both sides of Eq. (E.4) by $\rho_{\mathrm{l}0} A^2$ one obtains

$$P_{\mathrm{v}}^+ - P_{\mathrm{g}}^+ = \rho_{\mathrm{l}}^+ R_{\mathrm{b}}^+ \frac{\mathrm{d}^2 R_{\mathrm{b}}^+}{\mathrm{d}t^{+2}} + \rho_{\mathrm{l}}^+ \frac{3}{2} \left(\frac{\mathrm{d}R_{\mathrm{b}}^+}{\mathrm{d}t^+} \right)^2 + \frac{4\mu_{\mathrm{l}}^+ \mu_{\mathrm{l}0}}{R_{\mathrm{b}}^+ \rho_{\mathrm{l}0} A R_{\mathrm{c}}} \frac{\mathrm{d}R_{\mathrm{b}}^+}{\mathrm{d}t^+} + \frac{2\sigma^+ \sigma_0}{R_{\mathrm{b}}^+ \rho_{\mathrm{l}0} A^2 R_{\mathrm{c}}}. \tag{E.5}$$

Defining $\mathrm{Re} = \frac{\rho_{l0} A R_c}{\mu_{l0}}$ and $\mathrm{We} = \frac{\rho_{l0} A^2 R_c}{\sigma_0}$, the nondimensional RPE for an isolated vapor bubble in an infinite liquid medium without bubble-bubble interactions is expressed as

$$P_v^+ - P_g^+ = \rho_l^+ R_b^+ \frac{\mathrm{d}^2 R_b^+}{\mathrm{d}t^{+2}} + \rho_l^+ \frac{3}{2} \left(\frac{\mathrm{d}R_b^+}{\mathrm{d}t^+} \right)^2 + \frac{4\mu_l^+ \mu_{l0}}{R_b^+ \mathrm{Re}_b} \frac{\mathrm{d}R_b^+}{\mathrm{d}t^+} + \frac{2\sigma^+}{R_b^+ \mathrm{We}_b}. \quad \text{(E.6)}$$

Substituting the scaling relations shown in Eq. (E.3) into Eq. (E.2) yields

$$\begin{aligned} \left(P_v^+ - P_g^+\right) \rho_{l0} A^2 &= \rho_l^+ R_b^+ \rho_{l0} A^2 \left(1 + 2\pi R_d^{+2} n^+ R_b^+\right) \frac{\mathrm{d}^2 R_b^+}{\mathrm{d}t^{+2}} \\ &+ \rho_l^+ \rho_{l0} A^2 \left(\frac{3}{2} + 4\pi R_d^{+2} n^+ R_b^+ \right) \left(\frac{\mathrm{d}R_b^+}{\mathrm{d}t^+} \right)^2 + \frac{4\mu_l^+ \mu_{l0} A}{R_b^+ R_c} \frac{\mathrm{d}R_b^+}{\mathrm{d}t^+} \\ &+ 4\pi n^+ \rho_l^+ R_d^+ R_b^{+2} \rho_{l0} A^2 \left(\frac{\mathrm{d}R_d^+}{\mathrm{d}t^+} \right) \left(\frac{\mathrm{d}R_b^+}{\mathrm{d}t^+} \right) + \frac{2\sigma^+ \sigma_0}{R_b^+ R_c}. \end{aligned} \quad \text{(E.7)}$$

Dividing both sides by $\rho_{l0} A^2$, Eq. (E.7) becomes

$$\begin{aligned} P_v^+ - P_g^+ &= \rho_l^+ R_b^+ \left(1 + 2\pi R_d^{+2} n^+ R_b^+\right) \frac{\mathrm{d}^2 R_b^+}{\mathrm{d}t^{+2}} + \rho_l^+ \left(\frac{3}{2} + 4\pi R_d^{+2} n^+ R_b^+ \right) \left(\frac{\mathrm{d}R_b^+}{\mathrm{d}t^+} \right)^2 \\ &+ \frac{4\mu_l^+ \mu_{l0}}{R_b^+ \rho_{l0} A R_c} \frac{\mathrm{d}R_b^+}{\mathrm{d}t^+} + 4\pi n^+ \rho_l^+ R_d^+ R_b^{+2} \left(\frac{\mathrm{d}R_d^+}{\mathrm{d}t^+} \right) \left(\frac{\mathrm{d}R_b^+}{\mathrm{d}t^+} \right) + \frac{2\sigma^+ \sigma_0}{R_b^+ \rho_{l0} A^2 R_c}. \end{aligned} \quad \text{(E.8)}$$

Substituting $\mathrm{Re}_b = \frac{\rho_{l0} A R_c}{\mu_{l0}}$ and $\mathrm{We}_b = \frac{\rho_{l0} A^2 R_c}{\sigma_0}$, the nondimensional RPE of a spherically symmetric vapor bubble in a single droplet configuration considering bubble-bubble interactions is given by

$$\begin{aligned} P_v^+ - P_g^+ &= \rho_l^+ R_b^+ \left(1 + 2\pi R_d^{+2} n^+ R_b^+\right) \frac{\mathrm{d}^2 R_b^+}{\mathrm{d}t^{+2}} + \rho_l^+ \left(\frac{3}{2} + 4\pi R_d^{+2} n^+ R_b^+ \right) \left(\frac{\mathrm{d}R_b^+}{\mathrm{d}t^+} \right)^2 \\ &+ \frac{4\mu_l^+}{R_b^+ \mathrm{Re}_b} \frac{\mathrm{d}R_b^+}{\mathrm{d}t^+} + 4\pi n^+ \rho_l^+ R_d^+ R_b^{+2} \left(\frac{\mathrm{d}R_d^+}{\mathrm{d}t^+} \right) \left(\frac{\mathrm{d}R_b^+}{\mathrm{d}t^+} \right) + \frac{2\sigma^+}{R_b^+ \mathrm{We}_b}. \end{aligned} \quad \text{(E.9)}$$

F Schematic of the Multi-hole Injector

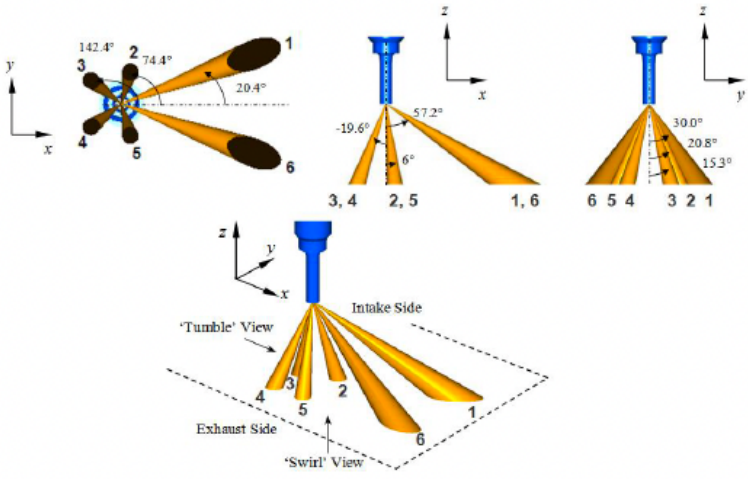

Figure F.1: Schematic of the multi-hole injector and the spray plumes.

G Hiroyasu and Arai Correlation

The spray cone angle for the simulations without the flash-boiling model is predicted by the correlation proposed by Hiroyasu and Arai [113] as

$$\theta = C_{\mathrm{noz}} \left(\frac{\rho_{\mathrm{a}}}{\rho_{\mathrm{l}}} \right)^{0.26} , \tag{G.1}$$

where

$$C_{\mathrm{noz}} = 83.5 \left(\frac{\mathsf{L_{noz}}}{\mathsf{D_{noz}}} \right)^{-0.22} \left(\frac{\mathsf{D_{noz}}}{\mathsf{D_{sac}}} \right)^{0.15} , \tag{G.2}$$

where $\mathsf{D_{noz}}$ is the nozzle exit diameter and $\mathsf{D_{sac}}$ the sac diameter of the nozzle.

H Derivation of the Extended CAS Model Coefficients

H.1 Derivation of the Superheated Vaporization Coefficients

H.1.1 Internal Vaporization

The vaporization of the superheated liquid causes the vapor bubbles to grow in size and subsequently leads to the expansion of the liquid droplet. For a single bubble, from the mass continuity

$$\rho_{\mathrm{l}} \frac{\mathrm{d}R_{\mathrm{d}}}{\mathrm{d}t} = \rho_{\mathrm{v}} \frac{\mathrm{d}R_{\mathrm{b}}}{\mathrm{d}t}. \tag{H.1}$$

Rearranging H.1 yields

$$\frac{\mathrm{d}d_{\mathrm{d}}^2}{\mathrm{d}t} = 4d_{\mathrm{d}} \frac{\rho_{\mathrm{v}}}{\rho_{\mathrm{l}}} \frac{\mathrm{d}R_{\mathrm{b}}}{\mathrm{d}t} \tag{H.2}$$

Summing over the total number of vapor bubbles, H.2 becomes

$$\frac{\mathrm{d}d_{\mathrm{d}}^2}{\mathrm{d}t} = N_{\mathrm{bub}} \times 4d_{\mathrm{d}} \frac{\rho_{\mathrm{v}}}{\rho_{\mathrm{l}}} \frac{\mathrm{d}R_{\mathrm{b}}}{\mathrm{d}t} = K_{\mathrm{vap,exp}} \tag{H.3}$$

H.1.2 External Vaporization

The vapor mass flux from the droplet outer surface due to the heat transfer from the droplet inner core is modeled as [25]

$$\rho_{\mathrm{s}} v_{\mathrm{s}} = \frac{h_{\mathrm{f}} \left(T_{\mathrm{d}} - T_{\mathrm{b}}\right)}{L\left(T_{\mathrm{b}}\right)}, \tag{H.4}$$

where v_{s} denotes the vapor flow rate from the droplet outer surface. From the mass continuity at the droplet surface

$$\frac{\rho_{\mathrm{l}}}{2} \frac{\mathrm{d}d_{\mathrm{d}}}{\mathrm{d}t} = \rho_{\mathrm{s}} v_{\mathrm{s}}. \tag{H.5}$$

Equating Eq. (H.5) with the Eq. (H.4) yields

$$\frac{\rho_{\mathrm{l}}}{2} \frac{\mathrm{d}d_{\mathrm{d}}}{\mathrm{d}t} = \frac{h_{\mathrm{f}} \left(T_{\mathrm{d}} - T_{\mathrm{b}}\right)}{L\left(T_{\mathrm{b}}\right)}. \tag{H.6}$$

Rearranging Eq. (H.6), the rate of change of d_d^2 can be expressed as

$$\frac{\mathrm{d}d_\mathrm{d}^2}{\mathrm{d}t} = \frac{4d_\mathrm{d}h_\mathrm{f}\left(T_\mathrm{d}-T_\mathrm{b}\right)}{\rho_\mathrm{l}L\left(T_\mathrm{b}\right)} = K_{\mathrm{vap,ht1}}. \tag{H.7}$$

Similarly, the vapor mass flux due to the temperature gradient between the droplet surface and the external ambient is expressed as

$$\rho_s v_s = \frac{h_\mathrm{ex}f_3\left|T_\mathrm{g}-T_\mathrm{s}\right|}{L\left(T_\mathrm{s}\right)}. \tag{H.8}$$

Using mass continuity at the droplet surface (Eq. (H.5)) and rearranging Eq. (H.8) yields

$$\frac{\mathrm{d}d_\mathrm{d}^2}{\mathrm{d}t} = \frac{4d_\mathrm{d}f_3h_\mathrm{ex}\left|T_\mathrm{g}-T_\mathrm{s}\right|}{\rho_\mathrm{l}L\left(T_\mathrm{s}\right)} = K_{\mathrm{vap,ht2}}. \tag{H.9}$$

H.2 Derivation of the Heat Transfer Coefficient

The energy balance of the droplet-bubble system in the superheated regime can be written as

$$m_\mathrm{d}C_\mathrm{l}\left(T_\mathrm{d}\right)\frac{\mathrm{d}T_\mathrm{d}}{\mathrm{d}t} = 4\pi r_\mathrm{d}^2Q_\mathrm{d} - 4\pi r_\mathrm{d}^2\rho_\mathrm{s}v_\mathrm{s}L\left(T_\mathrm{s}\right) - 4\pi R_\mathrm{b}^2\rho_\mathrm{v}N_\mathrm{bub}\dot{R}_\mathrm{b}L\left(T_\mathrm{d}\right). \tag{H.10}$$

Substituting

$$Q_\mathrm{d} = \frac{\lambda_\mathrm{g}\left(T_\mathrm{ref}\right)\left(T_\mathrm{g}-T_\mathrm{s}\right)}{d_\mathrm{d}}f_{2,\mathrm{sup}}\mathrm{Nu_d} \tag{H.11}$$

and

$$\rho_s v_s = \frac{h_\mathrm{f}\left(T_\mathrm{d}-T_\mathrm{b}\right)}{L\left(T_\mathrm{b}\right)} + \frac{f_3h_\mathrm{ex}|T_\mathrm{g}-T_\mathrm{s}|}{L\left(T_\mathrm{b}\right)} \tag{H.12}$$

in Eq. (H.10) and rearranging yields

$$\frac{\mathrm{d}T_\mathrm{d}}{\mathrm{d}t} = \frac{6f_{2,\mathrm{sup}}\mathrm{Nu_d}\lambda_\mathrm{g}(T_\mathrm{ref})(T_\mathrm{g}-T_\mathrm{s})}{\rho_\mathrm{l}d_\mathrm{d}^2C_\mathrm{l}(T_\mathrm{d})} - \frac{3K_{\mathrm{vap,ext}}L\left(T_\mathrm{s}\right)}{2d_\mathrm{d}^2C_\mathrm{l}\left(T_\mathrm{d}\right)} - \frac{3K_{\mathrm{vap,exp}}L\left(T_\mathrm{d}\right)}{2d_\mathrm{d}^2C_\mathrm{l}\left(T_\mathrm{d}\right)}. \tag{H.13}$$

The energy balance of the droplet-bubble system in the subcooled regime can be written as

$$m_\mathrm{d}C_\mathrm{l}\left(T_\mathrm{d}\right)\frac{\mathrm{d}T_\mathrm{d}}{\mathrm{d}t} = 4\pi r_\mathrm{d}^2Q_\mathrm{d} - 4\pi r_\mathrm{d}^2\rho_\mathrm{s}v_\mathrm{s}L\left(T_\mathrm{s}\right). \tag{H.14}$$

Substituting

$$Q_{\mathrm{d}} = \frac{\lambda_{\mathrm{g}}\left(T_{\mathrm{ref}}\right)\left(T_{\mathrm{g}} - T_{\mathrm{s}}\right)}{d_{\mathrm{d}}} f_{2,\mathrm{sub}} \mathrm{Nu}_{\mathrm{d}} \quad \text{and} \quad \rho_{\mathrm{s}} v_{\mathrm{s}} = 2\rho_{\mathrm{s}} \Gamma_{\mathrm{v,g}} \frac{ln(1 + B_{\mathrm{M,d}})}{d_{\mathrm{d}}} \tag{H.15}$$

in Eq. (H.14) and rearranging yields

$$\frac{\mathrm{d}T_{\mathrm{d}}}{\mathrm{d}t} = \frac{6 f_{2,\mathrm{sub}} \mathrm{Nu}_{\mathrm{d}} \lambda_{\mathrm{g}}(T_{\mathrm{ref}})(T_{\mathrm{g}} - T_{\mathrm{s}})}{\rho_{\mathrm{l}} d_{\mathrm{d}}^2 C_{\mathrm{l}}(T_{\mathrm{d}})} - \frac{3 K_{\mathrm{vap,ext}} L\left(T_{\mathrm{s}}\right)}{2 d_{\mathrm{d}}^2 C_{\mathrm{l}}\left(T_{\mathrm{d}}\right)}. \tag{H.16}$$

Bibliography

[1] A Clean Planet for all. A European long-term strategic vision for a prosperous, modern, competitive and climate neutral economy. Technical report, European Commission, 2018.

[2] F. Leach, R. Stone, D. Fennell, D. Hayden, D. Richardson, and N. Wicks. *Internal Combustion Engines: Performance, Fuel Economy and Emissions*, pages 193–202. Woodhead Publishing, London, November 2013. doi: https://doi.org/10.1533/9781782421849.5.193.

[3] R.D. Reitz. Directions in internal combustion engine research. *Combustion and Flame*, 160(1):1–8, January 2013. doi: https://doi.org/10.1016/j.combustflame.2012.11.002.

[4] P. Aleiferis and Z.R. van Romunde. An analysis of spray development with iso-octane, n-pentane, gasoline, ethanol and n-butanol from a multi-hole injector under hot fuel conditions. *Fuel*, 105:143–168, 2013. doi: http://dx.doi.org/10.1016/j.fuel.2012.07.044.

[5] S. Yang, Z. Song, T. Wang, and Z. Yao. An experimental study on phenomenon and mechanism of flash boiling spray from a multi-hole gasoline direct injector. *Atomization and Sprays*, 23(5):379–399, 2013. doi: 10.1615/AtomizSpr.2013007539.

[6] H. Zhao. *Advanced Direct Injection Combustion Engine Technologies and Development: Gasoline and Gas Engines*. Cambridge: Woodhead, 2010.

[7] M. Xu, Y. Zhang, W. Zeng, G. Zhang, and M. Zhang. Flash Boiling: Easy and Better Way to Generate Ideal Sprays than the High Injection Pressure. *SAE International Journal of Fuels and Lubricants*, 6(1): 137–148, April 2013. doi: 10.4271/2013-01-1614.

[8] Z. Zhao. *High injection pressure impinging diesel spray characteristics and subsequent soot formation in reacting conditions*. PhD thesis, Michigan Technical University, 2021.

[9] M.A. Ratcliff, J. Burton, P. Sindler, E. Christensen, L. Fouts, G.M. Chupka, and R.L. McCormick. Knock resistance and fine particle emissions for several biomass-derived oxygenates in a direct-injection spark-ignition engine. *SAE International Journal of Fuels and Lubricants*, 9 (1):59–70, apr 2016. ISSN 1946-3952. doi: https://doi.org/10.4271/2016-01-0705. URL `https://doi.org/10.4271/2016-01-0705`.

[10] A.H. Lefebvre. *Atomization and Sprays*. Hemisphere Publishing Cooperation, New York, USA, 1988.

[11] Z. Sun, M. Cui, M. Nour, X. Li, D. Hung, and M. Xu. Study of flash boiling combustion with different fuel injection timings in an optical engine using digital image processing diagnostics. *Fuel*, 284:119078, 2021. ISSN 0016-2361. doi: https://doi.org/10.1016/j.fuel.2020.119078.

[12] J. She. Experimental study on improvement of diesel combustion and emissions using flash boiling injection. In *SAE 2010 World Congress & Exhibition*. SAE International, apr 2010. doi: https://doi.org/10.4271/2010-01-0341. URL `https://doi.org/10.4271/2010-01-0341`.

[13] I. Schmitz, W. Ipp, and A. Leipertz. Flash Boiling Effects on the Development of Gasoline Direct-Injection Engine Sprays. *SAE Journal of Fuels and Lubricants*, 111:1025–1032, 2002. URL `https://www.jstor.org/stable/44734585`.

[14] H. Fujimoto, Y. Iwami, and J. Senda. Atomization Characteristics of Liquefied n-Butane Spray with Flash Boiling Phenomena. *International Journal of Fluid Mechanics Research*, 24(1–3):273–282, 1997. doi: 10.1615/InterJFluidMechRes.v24.i1-3.270.

[15] N. Yamazaki, N. Miyamoto, and T. Murayama. The Effects of Flash Boiling Fuel Injection on Spray Characteristics, Combustion, and Engine Performance in DI and IDI Diesel Engines. *SAE Transactions*, 94:388–395, 1985. URL `https://www.jstor.org/stable/44467680`.

[16] T. Badawy, H. Xu, and Y. Li. Macroscopic spray characteristics of iso-octane, ethanol, gasoline and methanol from a multi-hole injector under flash boiling conditions. *Fuel*, 307:121820, 2022. doi: https://doi.org/10.1016/j.fuel.2021.121820.

[17] W. Zeng, M. Xu, G. Zhang, Y. Zhang, and D.J. Cleary. Atomization and vaporization for flash-boiling multi-hole sprays with alcohol fuels. *Fuel*, 95:287–297, 2012. doi: 10.1016/j.fuel.2011.08.048.

[18] C. Price, A. Hamzehloo, P. Aleiferis, and D. Richardson. Numerical modelling of fuel spray formation and collapse from multi-hole injectors under flash-boiling conditions. *Fuel*, 221:518–541, 2018. doi: 10.1016/j.fuel.2018.01.088.

[19] J. Senda, Y. Hojyo, and H. Fujimoto. Modelling of atomization process in flash boiling spray. In *International Fuels & Lubricants Meeting & Exposition*. SAE International, oct 1994. doi: https://doi.org/10.4271/941925.

[20] J. Wang, X. Qiao, D. Ju, C. Sun, and T. Wang. Bubble nucleation, micro-explosion and residue formation in superheated jatropha oil droplet: The phenomena of vapor plume and vapor cloud. *Fuel*, 261:116431, 2020. ISSN 0016-2361. doi: https://doi.org/10.1016/j.fuel.2019.116431. URL `https://www.sciencedirect.com/science/article/pii/S0016236119317855`.

[21] X. Xi, H. Liu, M. Jia, M. Xie, and H. Yin. A new flash boiling model for single droplet. *Fuel*, 107:1129–1137, 2017. ISSN 00179310. doi: 10.1016/j.ijheatmasstransfer.2016.11.027.

[22] S. Li, Y. Zhang, W. Qi, and B. Xu. Quantitative observation on characteristics and breakup of single superheated droplet. *Experimental Thermal and Fluid Science*, 80:305–312, 2017. doi: https://doi.org/10.1016/j.expthermflusci.2016.09.004.

[23] R. Brown and J. York. Sprays formed by flashing liquid jets. *AIChE Journal*, 8(2):149–53, 1962.

[24] E. Sher and C. Elata. Spray Formation from Pressure Cans by Flashing. *Ind. Eng. Chem., Process Des. Dev.*, 16(2):237–242, 1977. doi: https://doi.org/10.1021/i260062a014.

[25] M. Adachi, V.G. McDonell, D. Tanaka, J. Senda, and H. Fujimoto. Characterization of fuel vapor concentration inside a flash boiling spray. *SAE Technical Paper*, 1997. ISSN 0148-7191. doi: https://doi.org/10.4271/970871.

[26] B.A. Vanderwege and S. Hochgreb. The effect of fuel volatility on sprays from high-pressure swirl injectors. *Symposium (International) on Combustion*, 27(2):1865–1871, 1998. doi: https://doi.org/10.1016/S0082-0784(98)80029-5.

[27] R. Kale and R. Banerjee. Understanding spray and atomization characteristics of butanol isomers and isooctane under engine like hot injector body conditions. *Fuel*, 237:191–201, 2019. doi: https://doi.org/10.1016/j.fuel.2018.09.142.

[28] J. Senda, Y. Wada, D. Kawano, and H. Fujimoto. Improvement of combustion and emissions indiesel engines by means of enhanced mixtureformation based on flash boiling of mixed fuel. *International Journal of Engine Research*, 9(1):15–27, 2008. doi: 10.1243/14680874JER02007.

[29] P. Aleiferis, J. Serras-Pereira, A. Augoye, T.J. Davies, R.F. Cracknell, and D. Richardson. Effect of fuel temperature on in-nozzle cavitation and spray formation of liquid hydrocarbons and alcohols from a real-size optical injector for direct-injection spark-ignition engines. *International Journal of Heat and Mass Transfer*, 53:4588–4606, 2010. doi: 10.1016/j.ijheatmasstransfer.2010.06.033.

[30] J. Serras-Pereira, Z. van Romunde, P. Aleiferis, D. Richardson, S. Wallace, and R.F. Cracknell. Cavitation, primary break-up and flash boiling of gasoline, iso-octane and n-pentane with a real-size optical direct-injection nozzle. *Fuel*, 89:2592–2607, 2010. doi: https://doi.org/10.1016/j.fuel.2010.03.030.

[31] Z. Sun, M. Cui, C. Ye, S. Yang, X. Li, D. Hung, and M. Xu. Split injection flash boiling spray for high efficiency and low emissions in a gdi engine under lean combustion condition. *Proceedings of the Combustion Institute*, 38(4):5769–5779, 2021. ISSN 1540-7489. doi: https://doi.org/10.1016/j.proci.2020.05.037.

[32] Z. Sun, S. Yang, M. Nour, X. Li, D. Hung, and M. Xu. Significant impact of flash boiling spray on in-cylinder soot formation and oxidation process. *Energy Fuels*, 34:10030–10038, 2020. doi: https://doi.org/10.1021/acs.energyfuels.0c01942.

[33] H. Guo, B. Wang, Y. Li, H. Xu, and Z. Wu. Characterizing external flashing jet from single-hole gdi injector. *International Journal of Heat and Mass Transfer*, 121:924–932, 2018. doi: https://doi.org/10.1016/j.ijheatmasstransfer.2018.01.042.

[34] H. Guo, X. Ma, Y. Li, S. Liang, Z. Wang, H. Xu, and J. Wang. Effect of flash boiling on microscopic and macroscopic spray characteristics in optical gdi engine. *Fuel*, 190:79–89, 2017. doi: http://dx.doi.org/10.1016/j.fuel.2016.11.043.

[35] M. Mojtabi, G. Wigley, and J. Helie. The effect of flash boiling on the atomization performance of gasoline direct injection multistream injectors. *Atomization and Sprays*, 24(6):467–493, 2014. doi: 10.1615/AtomizSpr.2014008296.

[36] P. Aleiferis, J. Serras-Pereira, Z. van Romunde, J. Caine, and M. Wirth. Mechanisms of spray formation and combustion from a multi-hole injector with e85 and gasoline. *Combustion and Flame*, 157(4):735–756, 2010. ISSN 0010-2180. doi: https://doi.org/10.1016/j.combustflame.2009.12.019.

[37] P. Bokinge, S. Heyne, and S. Harvey. Renewable OME from biomass and electricity—Evaluating carbon footprint and energy performance. *Energy Science and Engineering*, 8(7):2587–2598, 2020. ISSN 20500505. doi: 10.1002/ese3.687.

[38] Goeb D, Davidovic M, Cai L, Pancharia P, Bode M, Jacobs S et al. Oxymethylene ether – n-dodecane blend spray combustion: Experimental study and large-eddy simulations. *Proceedings of the Combustion Institute*, 38(2):3417–3425, 2021. doi: https://doi.org/10.1016/j.proci.2020.08.017.

[39] Deutz S, Bongartz D, Heuser B, Kätelhön A, Langenhorst LS, Omari A et al. Cleaner production of cleaner fuels: wind-to-wheel-environmental assessment of CO_2-based oxymethylene ether as a drop-in fuel. *Energy and Environmental Science*, 11:331–343, 2018. doi: https://doi.org/10.1039/C7EE01657C.

[40] A. Omari, B. Heuser, and S. Pischinger. Potential of oxymethylenether-diesel blends for ultra-low emission engines. *Fuel*, 209:232–237, 2017. ISSN 00162361. doi: 10.1016/j.fuel.2017.07.107.

[41] Langhorst T, Toedter O, Koch T, Niethammer B et al. Investigations on spark and sorona Ignition of oxymethylene ether-1 and dimethyl carbonate blends with gasoline by high-speed evaluation of OH* chemiluminescence. *SAE Int. J. Fuels Lubr.*, 11(1):5–20, 2018. ISSN 19463960. doi: 10.4271/04-11-01-0001.

[42] S. Leblanc, X. Yu, N.S. Sandhu, M. Wang, M. Zheng, and J. Tjong. Combustion and Emission Characteristics of SI and HCCI Combustion Fueled with DME and OME. *SAE Technical Paper*, 2020. ISSN 0148-7191. doi: 10.4271/2020-01-1355.

[43] Z. Wang, H. Liu, X. Ma, J. Wang, S. Shuai, and R.D. Reitz. Homogeneous charge compression ignition (HCCI) combustion of polyoxymethylene dimethyl ethers (PODE). *Fuel*, 183:206–213, 2016. ISSN 00162361. doi: 10.1016/j.fuel.2016.06.033.

[44] E. Sher, T. Bar-Kohany, and A. Rashkovan. Flash-boiling atomization. *Progress in Energy and Combustion Science*, 34(4):417–439, 2008. ISSN 03601285. doi: 10.1016/j.pecs.2007.05.001.

[45] A.J. Robinson. *Bubble growth dynamics in boiling*. PhD thesis, 2002.

[46] Rayleigh. VIII. On the pressure developed in a liquid during the collapse of a spherical cavity. *The London, Edinburgh, and Dublin Philosophical Magazine and Journal of Science*, 34(200):94–98, 1917. doi: 10.1080/14786440808635681.

[47] H.S. Lee and H. Merte. Spherical vapor bubble growth in uniformly superheated liquids. *International Journal of Heat and Mass Transfer*, 39(12):2427–2447, 1996. doi: 10.1016/0017-9310(95)00342-8.

[48] M.S. Plesset and S.A. Zwick. The growth of vapor bubbles in superheated liquids. *Journal of Applied Physics*, 25(4):493–500, 1954. ISSN 00218979. doi: 10.1063/1.1721668.

[49] M.S. Plesset and S.A. Zwick. A nonsteady heat diffusion problem with spherical symmetry. *Journal of Applied Physics*, 23(1):95–98, 1952. ISSN 00218979. doi: 10.1063/1.1701985.

[50] L. Scriven. On the dynamics of phase growth. *Chemical Engineering Science*, 10(1):1–13, 1959. ISSN 0009-2509. doi: https://doi.org/10.1016/0009-2509(59)80019-1.

[51] J. Riznic, G. Kojasoy, and N. Zuber. On the spherically symmetric phase change problem. *International Journal of Fluid Mechanics Research*, 26 (2):110–145, 1999. doi: 10.1615/InterJFluidMechRes.v26.i2.10.

[52] B.B. Mikic, W.M. Rohsenow, and P. Griffith. On bubble growth rates. *International Journal of Heat and Mass Transfers*, 13(4):657–666, 1970.

[53] Y.C. Lien. *Bubble growth rates at reduced pressure*. PhD thesis, 1969.

[54] M.D. Donne and M.P. Ferranti. The growth of vapor bubbles in superheated sodium. *International Journal of Heat and Mass Transfer*, 18 (4):477–493, 1975. ISSN 00179310. doi: 10.1016/0017-9310(75)90289-6.

[55] P. Zhang and Y.S. Zhang. Numerical modeling of dimethyl ether (DME) bubble growth and breakup. *Chinese Science Bulletin*, 54(14):2457–2463, 2009. ISSN 10016538. doi: 10.1007/s11434-009-0173-8.

[56] X. Xi, H. Liu, C. Cai, M. Jia, and X. Ma. Analytical and experimental study on boiling vaporization and multi-mode breakup of binary fuel droplet. *International Journal of Heat and Mass Transfer*, 165:120620, 2021. doi: https://doi.org/10.1016/j.ijheatmasstransfer.2020.120620.

[57] S. Fostiropoulos, G. Strotos, N. Nikolopoulos, and M. Gavaises. A simple model for breakup time prediction of water-heavy fuel oil emulsion droplets. *International Journal of Heat and Mass Transfer*, 164:120581, 2021. doi: https://doi.org/10.1016/j.ijheatmasstransfer.2020.120581.

[58] D. Kawano, Y. Goto, M. Odaka, and J. Senda. Modeling atomization and vaporization processes of flash-boiling spray. In *SAE 2004 World Congress & Exhibition*. SAE International, March 2004. doi: https://doi.org/10.4271/2004-01-0534.

[59] S. Yang. Development and validation of a flash boiling model for single-component fuel droplets. *Atomization and Sprays*, 27(11):963–997, 2017. ISSN 10445110. doi: 10.1615/AtomizSpr.2017020237.

[60] D. Dietzel, T. Hitz, C.D. Munz, and A. Kronenburg. Numerical simulation of the growth and interaction of vapour bubbles in superheated liquid jets. *International Journal of Multiphase Flow*, 121:103112, 2019. doi: https://doi.org/10.1016/j.ijmultiphaseflow.2019.103112.

[61] R. Mettin, I. Akhatov, U. Parlitz, C.D. Ohl, and W. Lauterborn. Bjerknes forces between small cavitation bubbles in a strong acoustic field. *Physical Review Letters*, 56(3):2924–2931, 1997. doi: https://doi.org/10.1103/PhysRevE.56.2924.

[62] C.F. Delale, G.H. Schnerr, and J. Sauer. Quasi-one-dimensional steady-state cavitating nozzle flows. *Journal of Fluid Mechanics*, 427:167–204, 2001. doi: https://doi.org/10.1017/S0022112000002330.

[63] N. Bremond, M. Arora, C.D. Ohl, and D. Lohse. Controlled multibubble surface cavitation. *Physical Review Letters*, 96:224501, 2006. doi: 10.1103/PhysRevLett.96.224501.

[64] M. Ida, T. Naoe, and M. Futakawa. Birect observation and theoretical study of cavitation bubbles in liquid mercury. *Physical Review Letters*, 756:046304, 2007. doi: https://doi.org/10.1103/PhysRevE.75.046304.

[65] Y. Ye and G. Li. Modelling of hydrodynamics cavitating flows considering the bubble-bubble interaction. *International Journal of Multiphase Flow*, 84:155–164, 2016. doi: https://doi.org/10.1016/j.ijmultiphaseflow.2016.03.022.

[66] M.A. Maiga, O.C. Delgosha, and D. Buisine. A new cavitation model based on bubble-bubble interactions. *Physics of Fluids*, 30:123301, 2018. doi: https://doi.org/10.1063/1.5052257.

[67] Y. Shi, K. Luo, X. Chen, D. Li, and L. Jia. A new cavitation model considering inter-bubble action. *International Journal of Naval Architechture and Ocean Engineering*, 13:566–574, 2021. doi: https://doi.org/10.1016/j.ijnaoe.2021.05.005.

[68] B. Zuo, A.M. Gomes, and C.J. Rutland. Modelling superheated fuel sprays and vaproization. *International Journal of Engine Research*, 1 (4):321–336, 2000. doi: 10.1243/1468087001545218.

[69] S.H. Park, H.J. Kim, and C.S. Lee. Study on the dimethyl ether spray characteristics according to the diesel blending ratio and the variations in the ambient pressure, energizing duration, and fuel temperature. *Energy and Fuels*, 25(4):1772–1780, 2011. ISSN 08870624. doi: 10.1021/ef101562b.

[70] C. Ji, C. Liang, and S. Wang. Investigation on combustion and emissions of DME/gasoline mixtures in a spark-ignition engine. *Fuel*, 90(3):1133–1138, 2011. ISSN 00162361. doi: 10.1016/j.fuel.2010.11.033.

[71] J. Yu, Y. Zhang, G. Jiang, and Q. Kui. An experimental study on steady flash boiling spray characteristics of DME/diesel blended fuel. *SAE Technical Paper*, 2020. ISSN 0148-7191. doi: https://doi.org/10.4271/2010-01-0879.

[72] Y. Zeng and C.F.F. Lee. An Atomization Model For Flash Boiling Sprays. *Combustion Science and Technology*, 169:45–67, 2001. doi: http://dx.doi.org/10.1080/00102200108907839.

[73] C. Price, A. Hamzehloo, P. Aleiferis, and D. Richardson. An Approach to Modeling Flash-Boiling Fuel Sprays for Direct-injection Spark-ignition Engines. *Atomization and Sprays*, 26(2):1–43, 2016. doi: 10.1615/AtomizSpr.2016015807.

[74] H. Guo, Y. Li, B. Wang, H. Zhang, and H. Xu. Numerical investigation on flashing jet behaviors of single-hole gdi injector. *International Journal of Heat and Mass Transfer*, 130:50–59, 2019. ISSN 0017-9310. doi: https://doi.org/10.1016/j.ijheatmasstransfer.2018.10.088.

[75] F. Duronio, S. Ranieri, A. Montanaro, L. Allocca, and A. De Vita. Ecn spray g injector: Numerical modelling of flash-boiling breakup and spray collapse. *International Journal of Multiphase Flow*, 145:103817, 2021. ISSN 0301-9322. doi: https://doi.org/10.1016/j.ijmultiphaseflow.2021.103817.

[76] F. Duronio, A.D. Mascio, C. Villante, M. Anatone, and A.D. Vita. Ecn spray g: Coupled eulerian internal nozzle flow and lagrangian spray simulation in flash boiling conditions. *International Journal of Engine Research*, 0(0):14680874221090732, 2022. doi: 10.1177/14680874221090732.

[77] A.Y. Deshmukh, T. Grenga, M. Davidovic, L. Schumacher, J. Palmer, M.A. Reddemann, R. Kneer, and H. Pitsch. A reduced-order model for multiphase simulation of transient inert sprays. *Internation Journal of Multiphase Flows*, 147:103872, 2022. doi: https://doi.org/10.1016/j.ijmultiphaseflow.2021.103872.

[78] S. Sazhin, G. Feng, and M. Heikal. A model for fuel spray penetration. *Fuel*, 80(15):2171–2180, 2001. doi: 10.1016/S0016-2361(01)00098-9.

[79] J.M. Desantes, R. Payri, F.J. Salvador, and A. Gil. Development and validation of a theoretical model for diesel spray penetration. *Fuel*, 22: 87–110, 2006. doi: 10.1016/j.fuel.2005.10.023.

[80] J.V. Pastor, J. Javier Lopez, J. Garcia, and J.M. Pastor. A 1D model for the description of mixing-controlled inert diesel sprays. *Fuel*, 87 (13-14):2871–2885, 2008. doi: 10.1016/j.fuel.2008.04.017.

[81] J. Desantes, J. Pastor, J. García-Oliver, and J. Pastor. A 1D model for the description of mixing-controlled reacting diesel sprays. *Combustion and Flame*, 156(1):234–249, 2009. doi: 10.1016/j.combustflame.2008.10.008.

[82] D.D. Loureiro, A. Kronenburg, J. Reutzsch, B. Weigand, and K. Vogiatzaki. Droplet size distributions in cryogenic flash atomization. *International Journal of Multiphase Flow*, 142:103705, 2021. doi: https://doi.org/10.1016/j.ijmultiphaseflow.2021.103705.

[83] C. Price, A. Hamzehloo, P. Aleiferis, and D. Richardson. Aspects of numerical modelling of flash-boiling fuel sprays. In *12th International Conference on Engines & Vehicles*. SAE International, sep 2015. doi: https://doi.org/10.4271/2015-24-2463.

[84] C. Price, A. Hamzehloo, P. Aleiferis, and D. Richardson. Numerical modelling of droplet breakup for flash-boiling fuel spray predictions. *International Journal of Multiphase Flow*, 125:103183, April 2020. doi: https://doi.org/10.1016/j.ijmultiphaseflow.2019.103183.

[85] O. Desjardins, G. Blanquart, G. Balarac, and H. Pitsch. High order conservative finite difference scheme for variable density low Mach number turbulent flows. *Journal of Computational Physics*, 227(15): 7125–7159, 2008. ISSN 10902716. doi: 10.1016/j.jcp.2008.03.027.

[86] V. Mittal, S. Kang, E. Doran, D. Cook, and H. Pitsch. LES of Gas Exchange in IC Engines. *Oil & Gas Science and Technology – Revue d'IFP Energies nouvelles*, 69(1):29–40, 2014. doi: 10.2516/ogst/2013122.

[87] S. Suma and M. Koizumi. Internal boiling atomization by rapid pressure reduction of liquids. *Trans. JSME (B)*, 43(376):4608–4617, 1977.

[88] K. Nakamura and T. Someya. Investigation on the tensile strength of real liquids. *Trans. JSME (B)*, 46(405):910–917, 1987.

[89] C.E. Brennen. *Cavitation and bubble dynamics*. Cambridge University Press, 2013. doi: https://doi.org/10.1017/CBO9781107338760.

[90] S.J. Board and R.B. Duffey. Spherical vapour bubble growth in superheated liquids. *Chemical Engineering Science*, 26(3):263–274, 1971. ISSN 00092509. doi: 10.1016/0009-2509(71)83001-4.

[91] R.S. Miller and J. Bellan. Direct numerical simulation of a confined three-dimensional gas mixing layer with one evaporating hydrocarbon-droplet-laden stream. *Journal of Fluid Mechanics*, 384(3):293–338, 1999. doi: 10.1017/S0022112098004042.

[92] G. Hubbard, V. Denny, and A. Mills. Droplet evaporation: Effects of transients and variable properties. *International Journal of Heat and Mass Transfer*, 18:1003–1008, 1975. doi: 10.1016/0017-9310(75)90217-3.

[93] M. Davidovic, T. Falkenstein, M. Bode, L. Cai, S. Kang, J. Hinrichs, and H. Pitsch. LES of n-Dodecane Spray Combustion Using a Multiple Representative Interactive Flamelets Model. *Oil and Gas Science and Technology*, 72(5), 2017. doi: https://doi.org/10.2516/ogst/2017019.

[94] M. Bode, T. Falkenstein, V. Le Chenadec, S. Kang, H. Pitsch, T. Arima, and H. Taniguchi. A New Euler/Lagrange Approach for Multiphase Simulations of a Multi-Hole GDI Injector. *SAE Technical Paper 2015-01-0949*, 2015. ISSN 01487191. doi: 10.4271/2015-01-0949.

[95] T.E. Daubert and R.P. Danner. *Physical and Thermodynamic Properties of Pure Compounds: Data Compilation*. New York : Hemisphere Pub. Corp, 1989. ISBN 9780891169482.

[96] S. Jacobs, M. Döntgen, A. Alquaity, W. Kopp, L. Kröger, U. Burke, H. Pitsch, K. Leonhard, H. Curran, and K. Heufer. Detailed kinetic modeling of dimethoxymethane. Part II: Experimental and theoretical study of the kinetics and reaction mechanism. *Combustion and Flame*, 205:522–533, 2019. doi: 10.1016/j.combustflame.2018.12.026.

[97] J. Safarov, S. Crusius, M. Reißig, M. Müller, and E. Hassel. Thermophysical properties of tetraoxymethylene dimethyl ether in a wide range of temperatures and pressures. (unpublished results).

[98] A. Kubota, H. Kato, and H. Yamaguchi. A new modelling of cavitating flows: a numerical study of unsteady cavitation ono a hydrofoil section. *J. Fluid Mech.*, 240:59–96, 1992.

[99] A. Prosperetti and M.S. Plesset. Vapor-bubble growth in a superheated liquid. *J. Fluid Mech.*, 85:349–368, 1978.

[100] A. Saha, A.Y. Deshmukh, T. Grenga, M. Bode, M. Grunewald, Y. Kaya, V. Kirsch, M.A. Reddemann, R. Kneer, and H. Pitsch. Numerical Modeling of the Flash Boiling Characteristics of E-Fuels at Low Ambient Pressure. In *International Conference on Liquid Atomization and Spray Systems (ICLASS), 30th September - 2nd September*, Edinburgh, Scotland UK, 2021.

[101] M. Germano, U. Piomelli, P. Moin, and W.H. Cabot. A dynamic subgrid-scale eddy viscosity model. *Physics of Fluids A: Fluid Dynamics*, 3(7): 1760–1765, 1991. doi: 10.1063/1.857955.

[102] C.T. Crowe, J.D. Schwarzkopf, M. Sommerfeld, and Y. Tsuji. *Mulitphase Flows with Droplets and Particles*. Taylor & Francis Group, LLC, 2012.

[103] A. Saha, T. Grenga, A.Y. Deshmukh, J. Hinrichs, M. Bode, and H. Pitsch. Numerical modeling of single droplet flash boiling behavior of e-fuels considering internal and external vaporization. *Fuel*, 308:121934, 2022.

[104] NIST. NIST Property Database, 2023. URL `https://webbook.nist.gov/chemistry/fluid/`.

[105] W.E. Ranz and W.R. Marshall. Evaporation from drops. Parts I & II. *Chem. Eng. Progr*, 48(3):141–146; 173–180, 1952. ISSN 09247963. doi: 10.1016/S0924-7963(01)00032-X.

[106] D.R. Dietzel. *Modeling and simulation of flash-boiling of cryogenic liquids*. PhD thesis, 2020.

[107] M.A. Patterson and R.D. Reitz. Modeling the effects of fuel spray characteristics on diesel engine combustion and emission. In *International Congress & Exposition*. SAE International, February 1998. doi: https://doi.org/10.4271/980131.

[108] R.D. Reitz. Modeling Atomization Processes in High-Pressure Vaporizing Sprays. *Atomization and Sprays*, 3:309–337, 1987.

[109] R.D. Reitz and R. Diwakar. Structure of high-pressure fuel sprays. In *SAE International Congress and Exposition*. SAE International, feb 1987. doi: https://doi.org/10.4271/870598.

[110] T. Gemci, K. Yakut, N. Chigier, and T.C. Ho. Experimental study of flash atomization of binary hydrocarbon liquids. *Internation Journal of Multiphase Flows*, 30:395–417, 2004. doi: doi:10.1016/j.ijmultiphaseflow.2003.12.003.

[111] Virtual injection rate generator, CMT-Motores Tér micos, Universitat Politècnica de València, 2023.

[112] H. Kamoun, G. Lamanna, and B. Weigand. High-Speed Shadowgraphy Investigations of Superheated Liquid Jet Atomisation. *ILASS-Americas 22nd Annual Conference on Liquid Atomization and Spray Systems, Cincinnati, OH*, May 2010.

[113] H. Hiroyasu and M. Arai. Fuel spray penetration and spray angle of diesel engines. *Trans. JSAE*, 21:5–11, 1980.

[114] Y. Wan. *Numerical Study of Transient Fuel Sprays with Autoignition and Combustion Under Diesel-Engine Relevant Conditions*. PhD thesis, RWTH Aachen University, 1997.

[115] A.J. Ghandilou and H. Taghavifar. New insight into air/spray boundary interaction for diesel and biodiesel fuels under different fuel temperatures. *Biofuels*, 13(9):1087–1101, 2022. doi: https://doi.org/10.1080/17597269.2022.2105867.

[116] G.B. Wallis. *One-Dimensional Two-Phase Flow*. McGraw-Hill, New York, 1969.

[117] A. Saha, A.Y. Deshmukh, T. Grenga, and H. Pitsch. Dimensional analysis of vapor bubble growth considering bubble-bubble interactions in flash boiling microdroplets of highly volatile liquid electrofuels. *International Journal of Multiphase Flow*, 2023.

[118] C.R. Wilke. A viscosity equation for gas mixtures. *The Journal of Chemical Physics*, 18(4):517, 1950. doi: 10.1063/1.1747673.

[119] C. von Kuensberg Sarre, S.c. Kong, and R.D. Reitz. Modeling the Effects of Injector Nozzle Geometry on Diesel Sprays. *SAE Technical Paper 1999-01-0912*, (724):1–14, 1999. doi: 10.4271/1999-01-0912.

[120] V.V. Rusanov. Calculation of interaction of non–steady shock waves with obstacles. *J. Comput. Math. Phys. USSR*, 1961.

[121] ECN. Engine Combustion Network (ECN), 2020. URL `https://ecn.sandia.gov/`. Accessed on 12.10.2020.

[122] L.M. Pickett, J. Manin, C.L. Genzale, D.L. Siebers, M.P. Musculus, and C.A. Idicheria. Relationship Between Diesel Fuel Spray Vapor Penetration/Dispersion and Local Fuel Mixture Fraction. *SAE International Journal of Engines*, 2011. ISSN 19463936. doi: 10.4271/2011-01-0686.

[123] D.L. Siebers. Scaling liquid-phase fuel penetration in diesel sprays based on mixing-limited vaporization. *SAE Technical Paper 1999-01-0528*, 1999. ISSN 26883627. doi: 10.4271/1999-01-0528.

[124] K. Joback and R. Reid. Estimation of pure-component properties from group-contributions. *Chemical Engineering Communications*, 57(1–6): 233–243, 1987. doi: 10.1080/00986448708960487.

[125] O. Govender, J. Rarey, B. Moller, and D. Ramjugernath. A new group contribution method for the estimation of thermal conductivity for non-electrolyte organic compounds. 2009.

[126] R.B. Bird, W.E. Stewart, and E.N. Lightfoot. *Transport phenomena*. Wiley; 2. edition, 2007.

[127] J. Gross and J. Vrabec. An equation-of-state contribution for polar components: dipolar molecules. *AIChE Journal*, 52(3):1194–1204, 2006. doi: https://doi.org/10.1002/aic.10683.

[128] J. Gross. A density functional theory for vapor-liquid interfaces using the PCP-SAFT equation of state. *The Journal of Chemical Physics*, 131(20):204705, 2009. doi: 10.1063/1.3263124.

[129] N. Van Nhu, M. Singh, and K. Leonhard. Quantum mechanically based estimation of perturbed-chain polar statistical associating fluid theory parameters for analyzing their physical significance and predicting properties. *The Journal of Physical Chemistry B*, 112(18):5693–5701, 2008. doi: https://doi.org/10.1021/jp7105742.

[130] A. von Müller and K. Leonhard. Surface tension calculations by means of a PCP-SAFT-DFT formalism using equation of state parameters from quantum mechanics. *Fluid Phase Equilibria*, 356:96–101, 2013. ISSN 0378-3812. doi: https://doi.org/10.1016/j.fluid.2013.07.005.